Report No. TE 4092/3-123-68

FACILITY FORM 602

N68-25619	
(ACCESSION NUMBER)	(THRU)
113	1
(PAGES)	(CODE)
CR 94764	03
(NASA CR OR TMX OR AD NUMBER)	(CATEGORY)

FIRST QUARTERLY PROGRESS REPORT

APPLIED THERMIONIC RESEARCH

Contract 952184

4 December 1967 to 4 March 1968

F. Fraim, E. P. Gyftopoulos, G. N. Hatsopoulos,
F. Holly, D. Lieb, F. Rufeh,
L. van Someren and C. Wang

JUN 1968
RECEIVED
NASA STI FACILITY
INPUT BRANCH

Prepared for

Jet Propulsion Laboratory
Pasadena, California

This work was performed for the Jet Propulsion Laboratory, California Institute of Technology, sponsored by the National Aeronautics and Space Administration under Contract NAS7-100.

Thermo Electron Corporation, 85 First Avenue, Waltham, Massachusetts 02154

Report No. TE 4092/3-123-68

FIRST QUARTERLY PROGRESS REPORT

APPLIED THERMIONIC RESEARCH

Contract 952184

4 December 1967 to 4 March 1968

F. Fraim, E. P. Gyftopoulos, G. N. Hatsopoulos,
F. Holly, D. Lieb, F. Rufeh,
L. van Someren and C. Wang

Prepared for

Jet Propulsion Laboratory
Pasadena, California

Thermo Electron Corporation, 85 First Avenue, Waltham, Massachusetts 02154

This report contains information prepared by Thermo Electron Corporation under JPL subcontract. Its content is not necessarily endorsed by the Jet Propulsion Laboratory, California Institute of Technology, or the National Aeronautics and Space Administration.

TABLE OF CONTENTS

TABLE OF CONTENTS (continued)

CHAPTER I

INTRODUCTION AND SUMMARY

This report presents the work performed for NASA/JPL during the quarterly period ending March 4, 1968. This work is part of an applied research program which has been in progress for several years. The primary objective of the program is the improvement of converter performance by a continuous interplay between theoretical analysis and experimental results.

An experimental study of the cesium-oxygen system has been started in order to determine the behavior of cesium oxides as electronegative additives, and to achieve practical methods for controlling them. (Chapter II). Two areas of activity were involved: mass spectrometry and differential thermal analysis to identify chemical species and determine their properties, and diodes to evaluate surface effects and thermionic performance. A quadrupole mass-spectrometric system was constructed, and the basic operation of the system was examined. An apparatus was designed and constructed to form accurate mixtures of cesium and oxygen. A filamentary diode was designed and constructed to study emitter work functions in the presence of various mixtures of cesium and oxygen. A differential thermal analyzer was operated with cesium; several shortcomings were found, and the system is under modification. A thermionic converter was set up to study the effect of gaseous oxygen, using argon as a carrier gas.

The relation between surface orbital electronegativity and work function, from the standpoints of both thermodynamics and quantum mechanics, was analyzed (Chapter III). First it was shown that the electronic structure of crystals can be described by means of spin-orbitals which are localized around individual lattice sites. Second, electronegativity was related to the chemical potential of an electron in a spin-orbital. Third, it was shown that the work function of a uniform surface equals the neutral orbital electronegativity of a spin-orbital localized around a surface atom.

A variable-spacing converter with a specially treated single-crystal tungsten emitter and a polycrystalline molybdenum collector was constructed. Experimental data was obtained for three emitter temperatures and a wide range of interelectrode spacings (Chapter IV). The performance map of this converter is almost completed.

Two types of vapor-deposited material were procured and examined, in the form of deposits 0.2 inch thick. The microstructure and preferred orientation were studied in the as-received condition and after exposure to various heat treatments in a vacuum (Chapter V).

The computer program for plasma analysis was reviewed, and particular attention was devoted to the boundary conditions at the emitter and collector sheaths (Chapter VI). These boundary conditions were modified, and the effect of this modification was examined.

No items of new technology are included in this report.

CHAPTER II

ELECTRONEGATIVE ADDITIVES

F. Fraim, F. Holly, and M. Shaw

During the past quarter work was begun in several areas for the investigation of additives. A mass spectrometer system has been built to study the species which volatilize from heated additive samples. Differential thermal analysis is being used to study the gross properties of various additives such as melting points, transition points, decomposition points, and temperature ranges of chemical reactions. Filamentary diodes are being built to study the effect of additives on thermionic emission from hot filaments.

The first additive to be studied is cesium oxide. All of the above techniques are being used to analyze the cesium-oxygen system. In order to produce repeatable oxide mixtures, an apparatus has been built to make oxide samples under carefully controlled conditions. The samples are produced in capsules, which are then sealed and stored for later use.

A. MASS SPECTROMETER

The major components of the mass spectrometer/molecular beam system are the Knudsen cell or source, the vacuum system, the mass spectrometer, and the signal detection and amplification apparatus. A schematic diagram of the system is shown in Figure II-1 and a photograph in Figure II-2.

Construction of the system, except for the Knudsen cell, is essentially complete. Construction of the main vacuum system has involved the following operations:

(1) Modification of the " cross" by an apertured partition to separate the high-vacuum chamber housing the mass spectrometer from the intermediate-vacuum chamber housing the Knudsen cell. This modification was hampered by the tendency of the cross to spring out of shape, and it was decided not to put a window into the side wall of the cross, as originally had been planned. Each chamber is separately pumped by its own 50-liter/sec ion pump.

(2) Welding in the pumping lines and leak-checking at the various stages of vacuum system assembly. It was found that the copper gaskets (supplied by Ultek) needed an additional annealing before they would seal. There appears to be some difference of opinion on this subject among various researchers.

(3) Mounting a shutter, a chopper, and a window on one of the ports (see Figure II-1). The purpose of the shutter is to aid in distinguishing between particles of a given charge-to-mass ratio which originate in the Knudsen cell and those which arise from extraneous sources. The chopper in conjunction with an ac detection system will be useful in extracting weak signals from the background. In some cases it will be necessary to use a lock-in amplifier. The rotary feed-throughs which drive the chopper and shutter are magnetically coupled, bakable devices.

(4) Machining of accessories for the mass spectrometer and alignment. The electric quadrupole mass spectrometer (E. A. I. Model 250) is operated in the " cross beam" mode. A shield was constructed to surround the ionizer. This

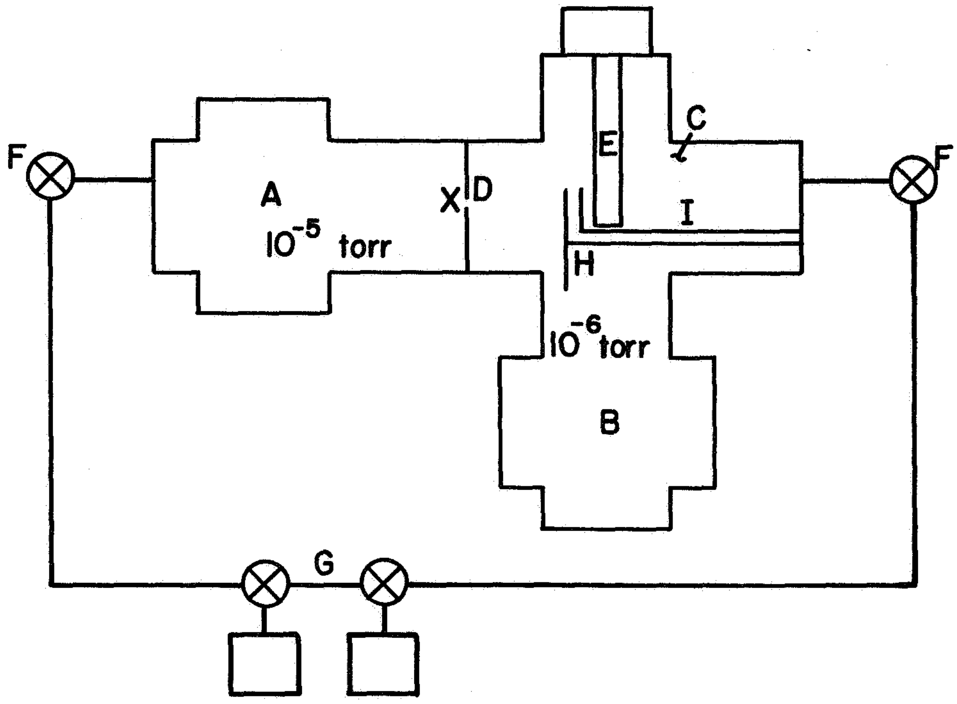

A) Double-flanged 50-liter/ sec ion pump which evacuates space where Knudsen cell resides

B) Single-flanged 50-liter/ sec ion pump which evacuates high-vacuum chamber

C) High-vacuum chamber or cross

D) Position of apertured partition between Knudsen cell chamber and high-vacuum chamber

E) Quadrupole

F) High-vacuum valves

G) Sorption pump manifold

H) Chopper

I) Shutter

X) Knudsen cell (5 x 10^{-3} torr)

Figure II-1 Schematic Diagram of Mass Spectrometer System.

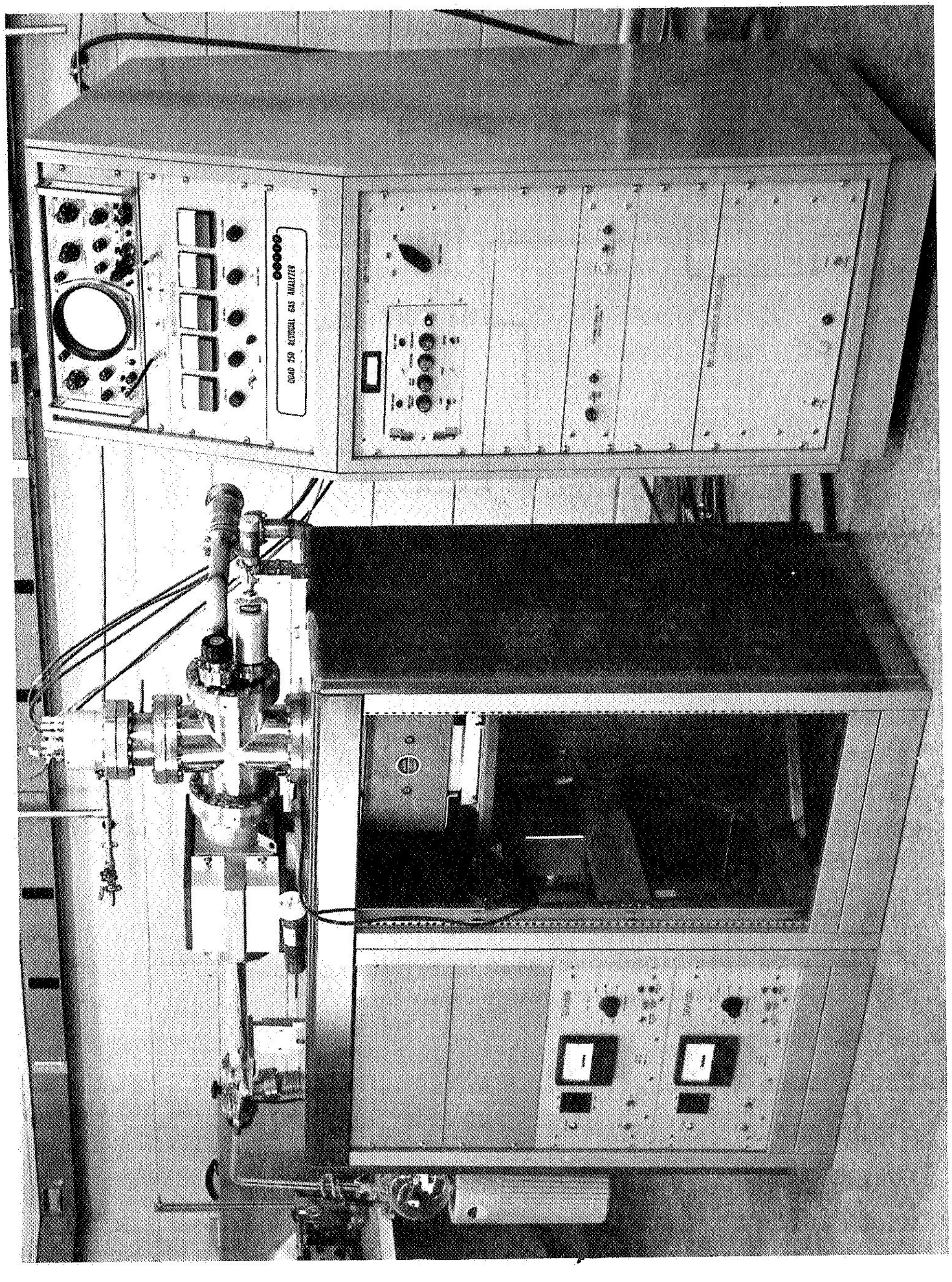

Figure II-2 Mass Spectrometer and Vacuum Apparatus.

shield can be coupled to a liquid-nitrogen transfer tube passing through the wall of the vacuum chamber for cooling when condensible vapors are being studied. Shielding the mass spectrometer from molecules not in the direct beam will be especially desirable when the lock-in amplifier is in operation, and will be generally useful in protecting the multiplier and eliminating " ghost" signals.

Alignment of the mass spectrometer with respect to the molecular beam was somewhat difficult due to the unavailability of scale drawings of the mass spectrometer and the necessity of keeping the mass spectrometer under vacuum as much as possible. Modifications of the adapter supplied with the instrument were necessary. The angular and vertical positions of the spectrometer and shield were indexed to simplify future assemblies.

(5) Construction of a simple gas flow system (see Figure II-3). The purpose of this apparatus is to produce a molecular beam of the same density and profile as will be produced under operating conditions with the Knudsen cell in place. It will be used in preliminary manipulations with the mass spectrometer and will provide a crude means of calibration when the test gas is of known composition.

The system has been put through a light bake-out, and the mass spectrometer has been operated on the background gases.

Detailed drawings for construction of the Knudsen cell are nearly completed.

According to preliminary calculations, pressures under typical experimental conditions will approximate 5×10^{-3} torr in the Knudsen cell, 10^{-5} torr in chamber A (see Figure II-1) housing the cell, and 10^{-8} torr as the background in the mass spectrometer chamber (B and C). The first project for the system will be to analyze the high-temperature chemistry of cesium oxides.

B. APPARATUS FOR CESIUM OXIDE PREPARATION

In order to have a reproducible mixture of cesium and oxygen for the various experiments, a special apparatus has been built. The purpose of this apparatus is to maintain rigid control on the conditions under which the oxides are formed: closely controlled amounts of cesium and oxygen are combined under controlled temperature conditions. The oxide is formed in a thin-walled molybdenum capsule which is sealed off and can later be cracked open when the oxide is wanted. These capsules will be used in all of the experiments, ensuring accurate control over the oxides used in each experiment.

Figure II-4 is a drawing of the apparatus which has been built to produce the oxide capsules. The system is made of copper tubing with two molybdenum sections. One molybdenum section is the capsule in which the oxide is formed. This capsule is connected to the rest of the system through a copper tube which is pinched off to seal the capsule. The second molybdenum section is a plug in the oxygen feed line which is used to isolate the oxygen line from the rest of the system during outgassing and cesiating of the capsule. When oxygen is desired, this plug is cracked open by pinching the copper tube. A precisely measured quantity of oxygen is then allowed to react with the cesium. After final evacuation of the system the capsule is pinched off and stored for later use.

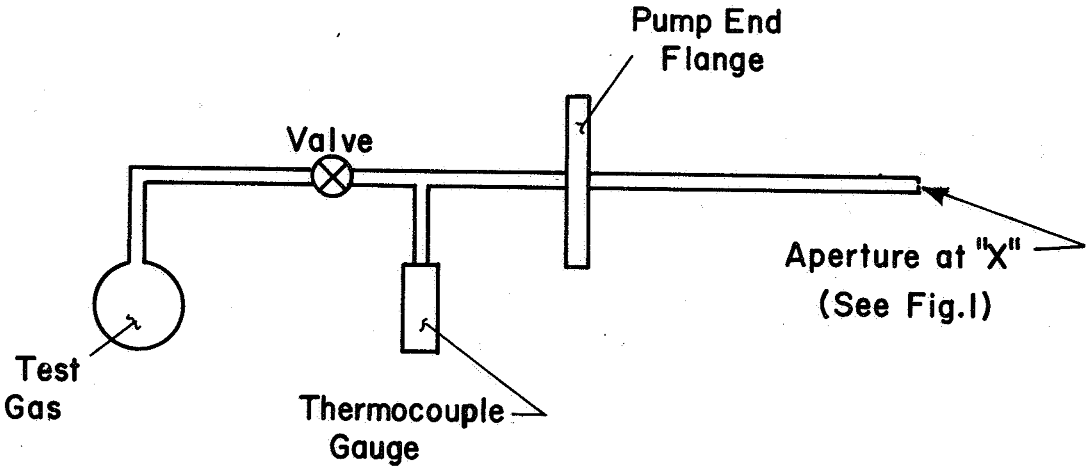

Figure II-3 Gas Manifold.

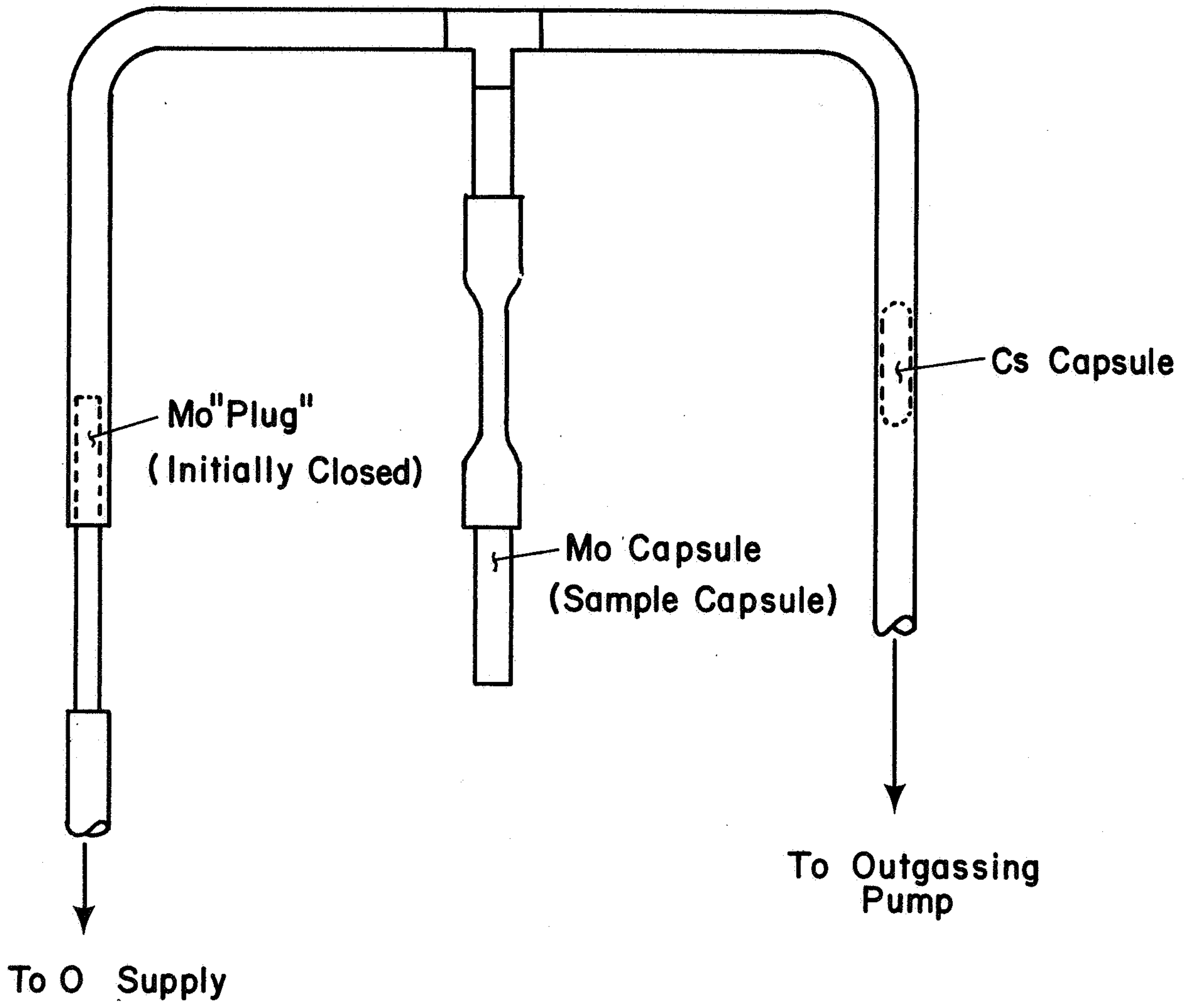

Figure II-4 Cesium Oxide Forming Apparatus.

C. FILAMENTARY DIODES

To observe the effects of the volatile species of cesium oxide on emitter work function, filamentary diodes will be used. These diodes are well suited for obtaining this type of data due to their simplicity, accuracy and low cost. The capsules discussed above will be used in these diodes.

Figure II-5 is a design drawing of the filamentary diode. The emitter is a tungsten filament, while the cylindrical collector and guards are nickel. The envelope is made of stainless steel tubing. The lead-through is a ceramic octal plug.

The data that will be obtained with these filamentary diodes includes changes in work function vs additive temperature and filament temperature, the additive temperatures at which these work function effects are obtained, and the approximate values of oxygen pressure estimated from the total pressure. All of this data is significant in predicting how an actual thermionic converter will perform when cesium oxide is introduced.

D. STUDY OF CESIUM-OXYGEN SYSTEMS BY DIFFERENTIAL THERMAL ANALYSIS

The differential thermal analysis of certain systems such as the ones containing cesium is a difficult problem, because not only does the sample have to be contained in a controlled atmosphere, but also special handling techniques are needed to introduce both cesium and oxygen into the analyzer. A Differential Thermalyzer made by Fisher Scientific Co. has been modified for the purpose. A new specimen holder has been designed and built, and it is illustrated schematically in Figure II-6. The Inconel block contains two wells. One is filled with molybdenum powder instead of the customary alumina, and the reference thermocouple is brazed fixed through a sealing plug. The other well is designed to collect condensing cesium, and it contains the other thermocouple of the differential pair. The block is supported by a thin-walled Inconel tube welded to it and to a closing cap at the upper end. The thermocouples pass through the closing cap and are connected externally (Figure II-7). A stainless steel tee is also welded to the closing cap and carries a metal-to-metal bellows valve connected to a vacuum system, an oxygen-administrating system, and a piece of copper tube from which cesium can be distilled into the sample well. After assembly, the system was baked at 200°C for two days at an internal pressure lower than 10^{-7} torr. After it was verified that the system was leak-tight, glass capsules containing 1 g of cesium were enclosed in the copper side tube, which was sealed again by the standard pinch-off technique. After evacuation the glass capsules were cracked, and the cesium was distilled into the sample well.

At present the system contains only cesium, and no oxygen has been added. The preliminary runs were only moderately successful, mainly because of the unknown thermal properties and the behavior of the system. It may have to be opened and calibration curves obtained with molybdenum vs molybdenum powder under vacuum, and some of the thermocouple connections must be better thermostated in order to obtain meaningful results with the pure cesium system. After this has been accomplished, a small controlled amount of oxygen will be introduced into the system, and thermograms will be obtained.

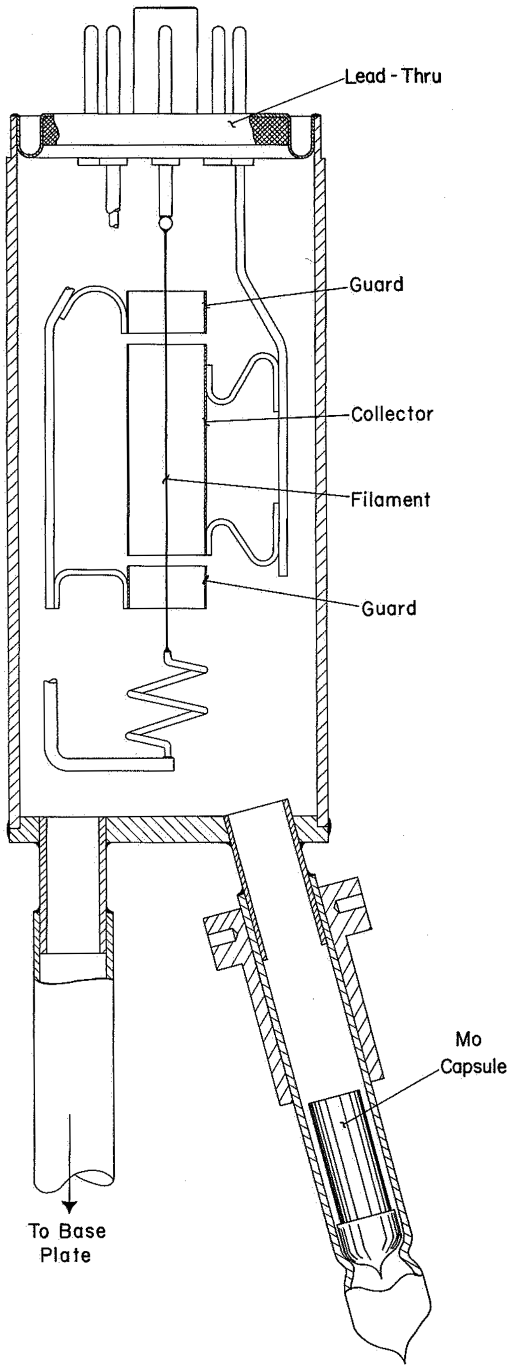

Figure II-5 Filamentary Diode.

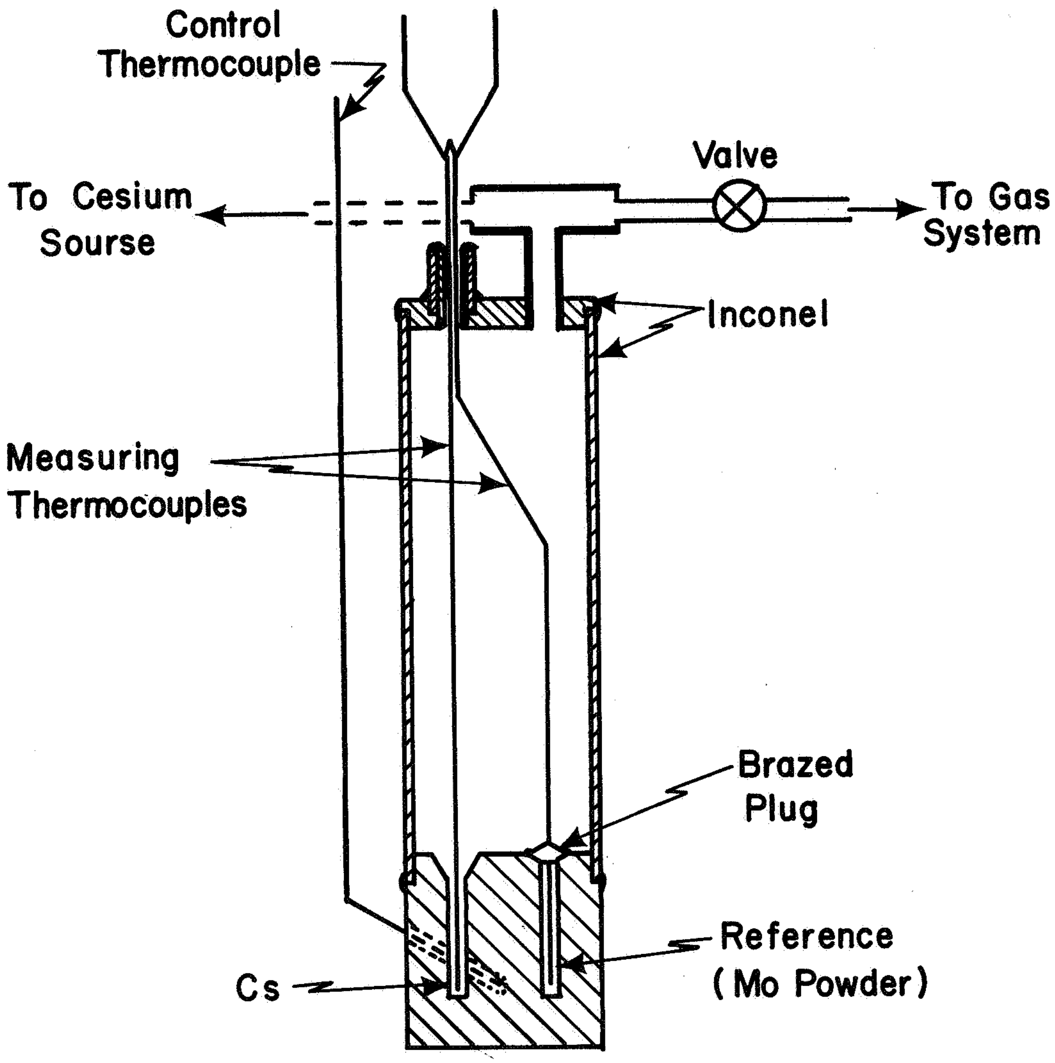

Figure II-6 Schematic View of DTA Sample Holder.

68-R-3-27

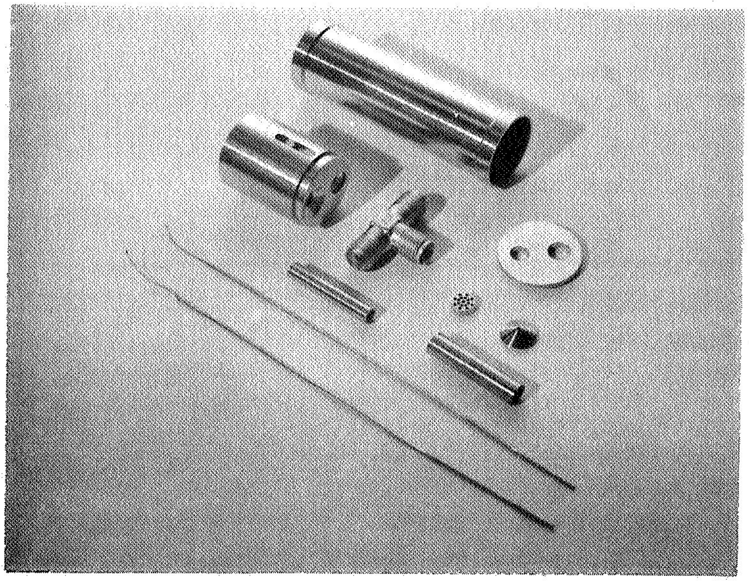

Figure II-7a. Components of Modified DTA Sample Holder

68-R-3-28

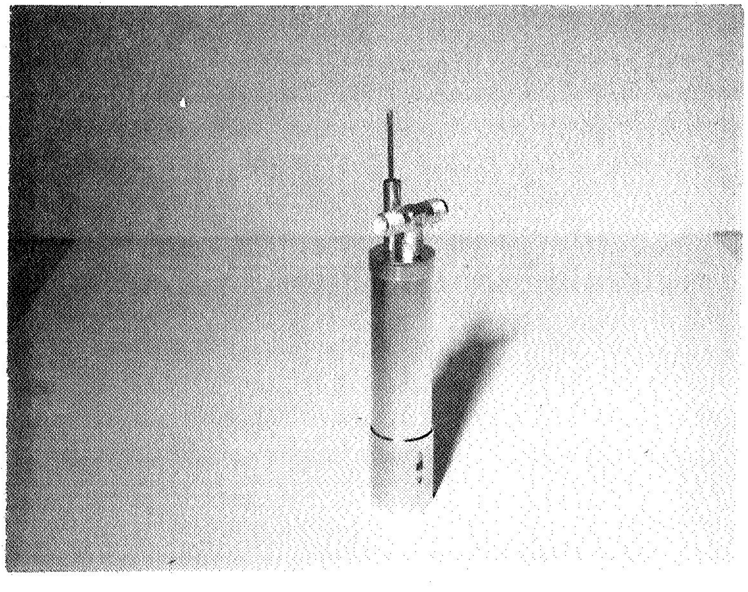

Figure II-7b. Assembled DTA Sample Holder.

CHAPTER III

QUANTUM-THERMODYNAMIC MEANING OF ELECTRONEGATIVITY AND WORK FUNCTION

Elias P. Gyftopoulos and George N. Hatsopoulos

A. INTRODUCTION

In previous publications by Steiner and Gyftopoulos,[1-3] emission phenomena occurring at metallic surfaces are analyzed in terms of surface atoms and their orbital electronegativity. For example, in Reference 1 the view is advanced that electrons emitted thermionically from a pure uniform surface of a crystal originate from a "valence orbital" of an "atom on the surface." It is assumed that the shape, the ionization energy, the electron affinity, and the excitation energies of this orbital are precisely defined, although not necessarily spectrocopically observable, and that they are determined by the many-body interactions of the crystal. On the basis of this picture, it is concluded that the work function of the surface must equal the neutral orbital electronegativity of the valence orbital of the surface atom.

This way of thinking about a crystal and its surface raises two questions. The first relates to the validity of viewing the electronic structure of a crystal in terms of orbitals which are associated with individual lattice sites, such as a valence orbital of a surface atom. It is customary to think of the electrons as belonging to the crystal as a whole, and therefore it is not obvious that electrons can be assigned to, localized around, individual lattice sites.

The second is a relatively old question. It refers to the meaning of electronegativity. This quantity has been found useful in many chemical studies, and yet it has not been given a rigorous definition.

The purpose of this chapter is to discuss the preceding two questions, in the context of the one-electron approximation for the electronic structure of many-electron systems. It is shown that the picture of localized orbitals is valid, and that electronegativity equals the negative of the chemical potential of an electron in an orbital.

The chapter is organized as follows: First the procedure for the derivation of the localized orbitals is discussed. These orbitals are shown to provide a description of the electronic structure of crystals which is entirely equivalent to the well known quantum-mechanical picture of electrons in metals. Second, the work of the authors on the identification of electronegativity[4] with the chemical potential is summarized. Third, it is shown that the work function of a pure uniform surface equals the orbital electronegativity of a surface atom.

B. LOCALIZED SPIN-ORBITALS FOR CRYSTAL LATTICES

The equivalence between the descriptions of the electronic structure of crystals by means of either non-localized, band structure theory, or localized spin-orbitals is best understood through a brief review of procedures employed for the analysis of any N-electron system.

Quantum-mechanically, the analysis of the energy eigenstates of the electronic structure of N-electron systems is very difficult. To avoid the difficulty, the electrons are treated as an ideal substance. In other words, the N-electron Hamiltonian operator is reduced to a sum of N separable one-electron Hamiltonian operators. Various methods are used for the reduction. Differences between methods arise from the degree to which exchange and correlation effects are included in the one-electron potential energy. In this regard, all methods are approximate and not all methods are equally accurate.

A given one-electron Hamiltonian operator defines an energy eigenvalue problem. The eigenfunctions and eigenvalues of this operator can be more readily found than those of the complete N-electron operator. Each eigenfunction, one-electron orbital, of a system with more than one nucleus, is delocalized throughout the system and is given the same interpretation as, say, the eigenfunctions of the hydrogen atom. For example, the orbital can accommodate at most two electrons with opposite spins. The negative of the eigenvalue equals approximately the energy required to extract an electron from the orbital, and it represents an ionization energy of the system. When the orbital is occupied by an electron with a given spin, it is called a spin-orbital. In many applications, a different orbital is used for each spin. In other words, each spin-orbital has its own spatial dependence.

By virtue of the ideal substance assumption, the eigenfunction ψ_N, for a given state of the system as a whole, should be given by the product of the occupied spin-orbitals. This, however, is not consistent with the symmetry rules of quantum mechanics.[5] For this reason ψ_N is represented by an antisymmetric, determinantal function of spin-orbitals, a Slater determinant.[6] The determinant is given by the relation

$$\psi_N = \frac{1}{(N!)^{1/2}} \begin{vmatrix} u_1(q_1) & u_2(q_1) & \cdot\cdot & u_N(q_1) \\ u_1(q_2) & u_2(q_2) & \cdot\cdot & u_N(q_2) \\ \cdot & \cdot & \cdot\cdot & \cdot \\ \cdot & \cdot & \cdot\cdot & \cdot \\ u_1(q_N) & u_2(q_N) & \cdot\cdot & u_N(q_N) \end{vmatrix} , \qquad (1)$$

where q_j represents the coordinates and spin of the j-th electron, u_i is the i-th orbital, and $u_i(q_j)$ is the i-th spin-orbital occupied by the j-th electron.

In general, it is found that one-electron energies E_i, eigenvalues E_i, are in good agreement with experimentally observed ionization energies of the system (atom, molecule, or crystal). However, the sum of the E_i, the eigenvalue of ψ_N with respect to the sum of the N one-electron operators, is not in good agreement with the total energy of the system, namely, the energy which would be derived from the exact ψ_N and the exact N-electron operator. Nevertheless, ψ_N in the form of Eq. 1 is often considered as an adequate approximation for the exact ψ_N.

For crystals, the one-electron results can also be described in terms of localized orbitals by means of the following procedure: Consider a crystal bounded by a uniform surface. Suppose that a relatively accurate one-electron equation has been established, say, by the method suggested by Slater.[7] The one-electron eigenvalue problem may be written in the form

$$(H_o + H_1)\, u = E u, \qquad (2)$$

where H_o is the one-electron, spatially periodic, Hamiltonian operator that would be derived if the solid were embedded in an infinite lattice, and H_1 is the one-electron operator which accounts for the perturbation introduced by the uniform surface. The spatial part of the eigenfunctions of Eq. 2 can be expanded into a series of Wannier functions[8] $a_n(\underline{r} - \underline{R}_s)$

associated with the operator H_o.* Thus the i-th eigenfunction is given by the relation[9]

$$u_i(\underline{r}) = \sum_s \sum_n U_{in}(\underline{R}_s)\, a_n(\underline{r} - \underline{R}_s)\,, \tag{3}$$

where $U_{in}(\underline{R}_s)$ is a constant, and the sums are over all lattice sites $\underline{R}_s$ and over all bands n. Mathematically, Eq. 3 is exact if an infinite number of bands is included in the expansion. As in all practical problems, however, through a judicious choice of localized, Wannier-like functions $W_n(\underline{r}, \underline{R}_s)$ (for example, a suitable linear combination of Wannier functions at the site $\underline{R}_s$), the summation over n may be reduced to a number equal to the number of valence electrons per atom, without great loss of accuracy. Thus, if different orbitals are used for different spins, a spin-orbital $u_i(q_j)$ may be adequately

---

*Recall that the Block functions $b_n(\underline{k}, \underline{r})$ of the n-th band of the infinite crystal are given by the relation[10]

$$H_o b_n(\underline{k}, \underline{r}) = E_n(\underline{k}) b_n(\underline{k}, \underline{r}),$$

and that the Wannier functions $a_n(\underline{r} - \underline{R}_s)$ of the n-th band are determined by the expression

$$a_n(\underline{r} - \underline{R}_s) = N_L^{-1/2} \sum_k b_n(\underline{k}, \underline{r}) \exp(-i\underline{k} \cdot \underline{R}_s),$$

where $\underline{R}_s$ is the s-th site of the lattice, and N_L is the number of lattice sites. The Wannier functions form a complete, orthonormal set over all bands and over all lattice sites, namely

$$\int a_m^*(\underline{r} - \underline{R}_j)\, a_n(\underline{r} - R_i)\, d\underline{r} = \delta_{mn} \delta_{ij}.$$

Moreover, each Wannier function $a_n(\underline{r} - \underline{R}_s)$ is localized around, associated with, the s-th site.

represented by the relation

$$u_i(q_j) = \sum_s \sum_n^v c_{in}(\underline{R}_s)\, w_n(q_j, \underline{R}_s), \tag{4}$$

where v is the number of valence electrons per atom, and $c_{in}(\underline{R}_s)$ is a constant.

Without loss of generality, suppose the crystal is that of a monovalent metal, v equals unity and the number N_L of lattice sites equals the number N of valence electrons. For this crystal, substitution of Eq. 4 into the determinantal relation, Eq. 1, for the overall eigenfunction ψ_N yields

$$\psi_N = \frac{1}{(N!)^{1/2}} \begin{vmatrix} \sum_s c_1(\underline{R}_s)\, w(q_1, \underline{R}_s) & \cdots & \sum_s c_N(\underline{R}_s)\, w(q_1, \underline{R}_s) \\ \sum_s c_1(\underline{R}_s)\, w(q_2, \underline{R}_s) & \cdots & \sum_s c_N(\underline{R}_s)\, w(q_2, \underline{R}_s) \\ \vdots & \cdots & \vdots \\ \vdots & \cdots & \vdots \\ \vdots & \cdots & \vdots \\ \sum_s c_1(\underline{R}_s)\, w(q_N, R_s) & \cdots & \sum_s c_N(\underline{R}_s)\, w(q_N, \underline{R}_s) \end{vmatrix} \tag{5}$$

where the subscript n equals unity has been omitted from the w's and the c's. Note that each column of the determinant in Eq. 5 is a linear combination of the N Wannier-like functions associated with the N sites of the crystal. It follows from the rules for the product of two determinants that Eq. 5 can be written in the form

$$\psi_N = \frac{1}{(N!)^{1/2}} \begin{vmatrix} w(q_1, \underline{R}_1) & \cdots & w(q_1, \underline{R}_N) \\ w(q_2, \underline{R}_1) & \cdots & w(q_2, \underline{R}_N) \\ \vdots & \cdots & \vdots \\ \vdots & \cdots & \vdots \\ \vdots & \cdots & \vdots \\ w(q_N, R_1) & \cdots & w(q_N, \underline{R}_N) \end{vmatrix} \begin{vmatrix} c_1(\underline{R}_1) & c_2(\underline{R}_2) & \cdots & c_N(\underline{R}_1) \\ c_1(\underline{R}_2) & c_2(\underline{R}_2) & \cdots & c_N(\underline{R}_2) \\ \vdots & \vdots & \cdots & \vdots \\ \vdots & \vdots & \cdots & \vdots \\ \vdots & \vdots & \cdots & \vdots \\ c_1(\underline{R}_N) & c_2(\underline{R}_N) & \cdots & c_N(\underline{R}_N) \end{vmatrix} \tag{6}$$

In the form of Eq. 6, the eigenfunction ψ_N for the whole crystal admits the localized spin-orbital interpretation which is sought. Indeed, note that each Wannier-like function $w(q, \underline{R}_s)$ is a spin-orbital associated with, localized around, lattice site $\underline{R}_s$ (the set of constants $C_i(\underline{R}_s)$, for $i = 1, 2, N$, is also associated with the same site $\underline{R}_s$). If the N electrons of the crystal are distributed among the N spin-orbitals $w(q, \underline{R}_s)$, an antisymmetric determinantal function, Eq. 6, can be formed. This function is completely equivalent to that obtained from the delocalized orbitals. In other words, the ψ_N's constructed from either the localized or the delocalized spin-orbitals are identical.

It should be noted that the localized spin-orbitals $w(q, \underline{R}_s)$ are not energy eigenfunctions of the one-electron equations. Only ψ_N, Eq. 6, is an approximate eigenfunction of the Hamiltonian operator for the whole crystal. Nevertheless, each localized spin-orbital can be assigned precise values for the ionization energy, electron affinity, and excitation energies of the electron in the spin-orbital, in a manner which is consistent with the usual definitions of these quantities. The values of the ionization energy, electron affinity, etc., of a localized spin-orbital are not equal to the corresponding values of the delocalized spin-orbitals. This point can be seen from the definition of the ionization energy given below.

Suppose that ψ_N, Eq. 6, represents the ground state of the crystal. The ionization energy of a spin-orbital localized around lattice site $\underline{R}_s$ is defined as the difference between the energy corresponding to an eigenfunction ψ_{N-1} and that of the ground state. The eigenfunction ψ_{N-1} is given by Eq. 6 except that the s-th column and the s-th row of the first and the second determinants are replaced by zeros, respectively, and

$(N!)^{1/2}$ is replaced by $[(N-1)!]^{1/2}$. The Hamiltonian operator for ψ_{N-1} is that corresponding to N lattice sites and N-1 valence electrons. This definition of the ionization energy assumes that removal of a localized spin-orbital from the system does not alter the functional dependence of the other N-1 localized spin-orbitals. Such an assumption is used in practically all approaches to the analysis of the electronic structure of solids (see, for example, Koopmans' theorem for the one-electron Hartree-Fock equations[11]).

The other energies of a localizes spin-orbital can be defined in a manner analogous to that used for the ionization energy.

C. ELECTRONEGATIVITY AND CHEMICAL POTENTIAL

In this section, the work of the authors[4] on the identification of electronegativity with the negative of the chemical potential of an electron in an atom is summarized.*

In Reference 4, an ensemble of identical, one-atom systems is considered. Each atom is thought of as consisting of two components, electrons and ions. The systems are in thermodynamic equilibrium with a reservoir of electrons and ions at a small temperature T (degrees Kelvin). The components can flow back and forth between the systems and the reservoir. The energy eigenstates of the atoms are assumed to be derivable from the one-electron Hartree-Fock equations.[12] In other words, the electrons are viewed in an ideal substance.

---

* Strictly speaking, the electronegativity has been identified with the electrochemical potential. For the reference level of energy selected in this chapter, however, the values of the chemical and the electrochemical potential are identical.

According to the theory of statistics of ensembles,[13] the physical situation described above obeys the rules of grand canonical ensembles. Use of these rules yields the following important conclusions:

(1) Statistically, the energy E of a one-atom system can be expressed as a continuous function E(q) of a continuous variable q which represents a statistical measure of the charge in a valence spin-orbital. The range of the value of the charge q is from minus one electronic charge (-e) (the orbital is doubly occupied) through zero (the orbital is occupied by one electron) to plus one electron charge (+e) (the orbital is ionized).

(2) The chemical potential μ_c of a valence electron is given by the relation

$$\mu_c = -(\partial E(q)/\partial q) \text{ at constant entropy.} \qquad (7)$$

In the limit of very small temperatures, this potential is found to have the following exact values:

$$\mu_c = -(I + A)/2e \quad \text{for } q = 0 \quad \text{(neutral atom)},$$

$$\mu_c = \infty \quad \text{for } q = e \quad \text{(positive ion)},$$

and

$$\mu_c = -\infty \quad \text{for } q = -e \quad \text{(negative ion)},$$

where I and A are the first ionization energy and the electron affinity of the atom, respectively. The quantities I and A can also be referred to the valence electron spin-orbital.

(3) For fractional values q and for small T, μ_c is a function of both q and T.

(4) By virtue of (2) above, it is found that for small temperatures (in the limit of zero temperature) an excellent approximation for E(q) is given by the relation.

$$E(q) = \frac{I + A}{2e} q + \frac{I - A}{2} [1 - (1 - \frac{q^2}{e^2})^{1/2}] \qquad (8)$$

when the zero energy level is taken to be at the energy of the neutral atom (q equals zero). Note that this approximation yields exact values for E(q) and μ_c for q = -e, 0, e.

(5) The orbital electronegativity x(q) of a valence electron is defined as

$$x(q) = (\partial\ E(q)/\partial q) \text{ at constant entropy}$$
$$= -\mu_c$$

This is the first time that a rigorous definition of x(q) is given.

(6) The value of the neutral orbital electronegativity x(0) obtained from Eq. 8 is identical to the value of electronegativity suggested by Mulliken.[14] It should be noted, however, that Mulliken's value is considered to be approximate. Here the thermodynamic analysis yields that, in the limit of small temperatures, x(0) has the exact value given by the relation

$$x(0) \equiv \frac{I + A}{2e} \qquad (9)$$

(7) The definition of the orbital electronegativity given above can be easily extended to orbitals in systems other than atoms. Such an extension is discussed in the next section.

D. WORK FUNCTION AND ELECTRONEGATIVITY

Without loss of generality, consider a crystal of a monovalent metal, bounded by a uniform surface. Suppose the analysis of the electronic structure of this metal has been carried out with respect to a zero energy level taken at the points just outside the surface. Moreover, suppose that both the delocalized and the localized spin-orbitals have been established, in accordance with the procedure discussed in Section B.

Thermodynamically, for a system of N electrons, any set of N spin-oribitals which describes the system may be thought of as representing N degrees of freedom. When these N degrees of freedom are treated statistically, the following results can be obtained:

(1) Given the N delocalized spin-orbitals, one-electron spin-orbitals, the negative of the chemical potential of the surface, with respect to the points just outside the surface, equals the work function. This is the well known thermodynamic definition of work function.[15, 16]

(2) Given the N localized spin-orbitals, Wannier-like functions, suppose that all degrees of freedom are frozen except that corresponding to the spin-orbital localized around the surface site $\underline{R}_s$. Under this condition, the surface spin-orbital can be treated statistically by the same procedure as that used for atoms in Section C. In other words, this orbital may be thought of as a surface atom. Thus a chemical potential for the electron in the orbital can be defined. For example, in the limit of small temperatures, the value of the chemical potential of the localized spin-orbital equals

$$-(I_s + A_s)/2e,$$

where I_s and A_s are the ionization energy and the electron affinity of the orbital as defined in Section B. This value equals the negative of the neutral orbital electronegativity of the spin-orbital, Eq. 9.

(3) From thermodynamic equilibrium considerations, it can be shown that the chemical potential of the localized spin-orbital as defined in (2) must be equal to the chemical potential of the surface, as defined in (1).*

(4) By virtue of (1), (2), and (3), it follows that the work function equals the neutral orbital electronegativity of a spin-orbital localized around a surface atom.

In conclusion: (1) the characterization of the electronic structure of metals by localized spin-orbitals is equivalent to the ordinary picture of electrons in metals; (2) electronegativity can be given a rigorous thermodynamic definition; and (3) the neutral orbital electronegativity of a surface spin-orbital, atom, equals the work function of the surface.

---

*The proof of this statement is analogous to that used in the study of chemical reactions with or without a catalyst.[17]

REFERENCES FOR CHAPTER III

1. Steiner, D.; Gyftopoulos, E. P., "An Equation for the Prediction of Bare Work Functions." Report 27th Annual Conf. Physical Electronics, MIT, Cambridge (1967), p. 160.

2. Gyftopoulos, E. P.; Steiner, D., "Orbital Electronegativity and Physical Properties of Bimetallic Adsorption Systems." Report 27th Annual Conf. Physical Electronics, MIT, Cambridge (1967) p. 169.

3. Steiner, D.; Gyftopoulos, E. P., "Orbital Electronegativity and Physical Properties of Metal-Gas Adsorption Systems." Report Thermionic Conversion Specialist Conf., San Francisco (1967) 145.

4. Gyftopoulos, E. P.; Hatsopoulos, G. N., "Quantum Thermodynamic Definition of Electronegativity." To be published.

5. Tolman, R. C., The Principles of Statistical Mechanics. University Press, New York (1938), pp. 312-324.

6. Slater, J. C., Quantum Theory of Molecules and Solids, Vol. 1. McGraw-Hill, New York (1963), p. 43.

7. Slater, J. C., Quantum Theory of Molecules and Solids, Vol. 3. McGraw-Hill, New York (1967, pp. 265-271.

8. Slater, J. C., Quantum Theory of Molecules and Solids, Vol. 2. McGraw-Hill, New York (1965), pp. 154-158.

9. Koster, G. F.; Slater, J. C., "Wave Functions for Impurity Levels." Phys. Rev. 95 (1954), p. 1167.

10. Reference 6, Chapter 9.

11. Ibid., p. 96.

12. Ibid., Appendix 4.

13. Hatsopoulos, G. N.; Keenan, J. H., Principles of General Thermodynamics. John Wiley, New York (1965), Chapter 48.

14. Mulliken, R. S., "A New Electroaffinity Scale." J. Chem. Phys. 2 (1934), p. 782.

15. Reference 13, pp. 557-558.

16. Herring, C.; Nichols, M. H., "Thermionic Emission." Rev. Modern Phys. 21 (1949), p. 190.

17. Reference 13, pp. 329-330.

CHAPTER IV

PARAMETRIC DATA

D. Lieb, F. Rufeh, L. van Someren, C. Wang

A. SINGLE-CRYSTAL TUNGSTEN CONVERTER

A guard-ring converter with Mo collectors and a nominally single-crystal (110) tungsten emitter was constructed and tested during the first quarter. Performance data was obtained over the emitter temperature range of 1700°K to 1900°K and the interelectrode spacing range of 0.5 mil to 40 mils. The data was obtained in the form of cesium families at optimized collector temperatures.

1. Emitter Preparation

The emitter (W25) was prepared from an ingot of nominal single-crystal tungsten made by the Linde Division of Union Carbide Corporation. X-ray studies using the Laue back-reflection technique indicated that the material contained considerable substructure which was stable to annealing, but that all areas had an orientation that was grossly (110) along the ingot axis, and that exact (110) directions always lay within 4° of the ingot axis.

After polishing and heat treatment, the emitter showed several distinct grains, which glinted in slightly different directions. The microscopic examination revealed that the surface was composed of flat areas of (110) plane bounded by curves and connected by an undulating background, while occasional well defined plateaus or mesas stood out against this background. The surface of the whole emitter (to within 0.4 inch of the edge) was qualitatively similar; a representative photomicrograph is shown in Figure IV-1.

2. Performance Data

The performance of this converter was recorded in terms of cesium temperature families for various values of emitter temperature and interelectrode spacing. To simplify cross-plotting and to increase the usefulness of the data for converter design, a constant set of cesium temperatures have been used in these families. In order to facilitate the use of this data for analysis and correlation of converter parameters, the interelectrode spacing values were chosen in a manner to yield a consistent set of Pd values. The pressures and interelectrode spacings used are presented in Table IV-1.

Families of volt-ampere characteristics were obtained by changing the cesium reservoir temperature while the other converter parameters were held constant. Figures IV-2 to IV-5 show these families at the emitter temperature of 1700°K, with a range of 5 to 40 mils in interelectrode spacing. The collector temperature in these runs was held constant in the vicinity of its optimum value. The emitter temperature indicated represents the temperature at the surface of the emitter; the output voltage is measured from a voltage tap at the cold end of the emitter sleeve. The correction factor for conversion to electrode voltage is approximately 3 mV per A/cm^2. A summary of the cesium optimized envelopes at an emitter temperature of 1700°K is shown in Figure IV-6.

Cesium-temperature families obtained at an emitter temperature of 1800°K are shown in Figures IV-7 through IV-13, and a summary of these envelopes is shown in Figure IV-14. Similar data recorded at the emitter temperature of 1900°K is shown in Figures IV-15 through IV-20. The fully optimized performance of this converter for the emitter temperatures of 1700, 1800, and 1900°K is presented in Figure IV-21. The

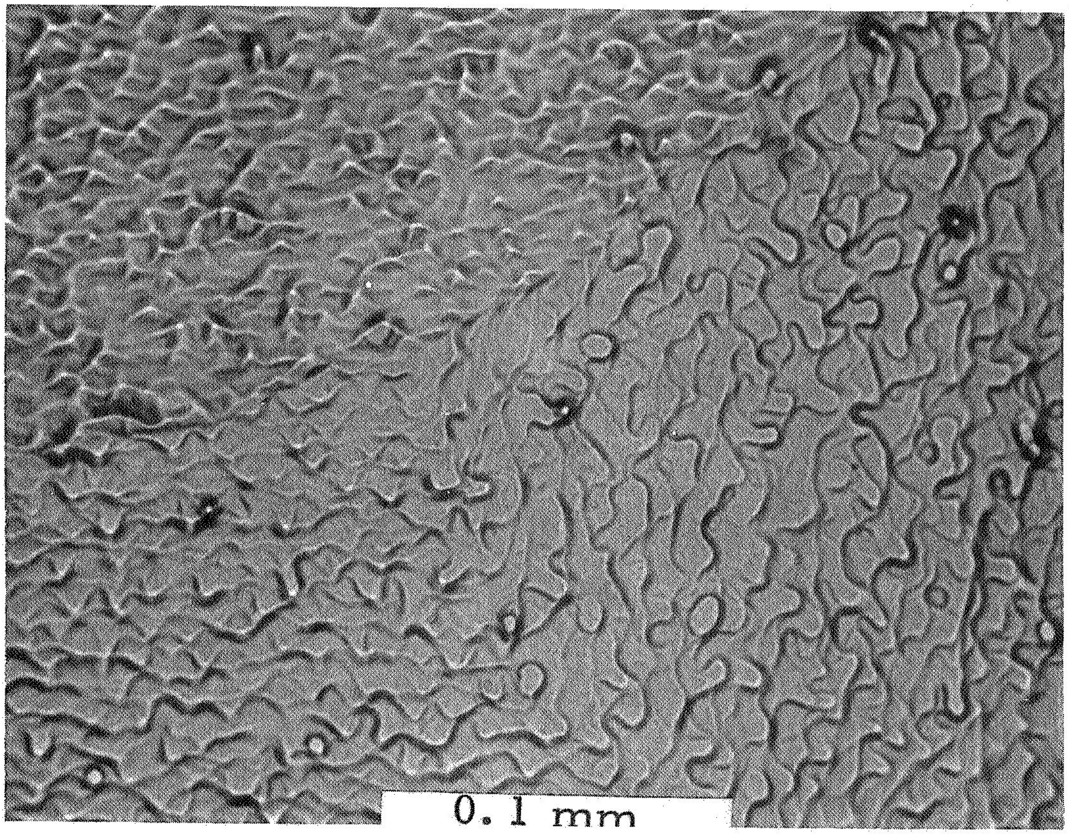

Figure IV-1

TABLE IV-1
CESIUM VAPOR PRESSURE TABLE

TEMPERATURE °K	PRESSURE, TORR
436	0.0156
444	0.0221
452	0.0312
460	0.0442
469	0.0625
477	0.0884
487	0.125
496	0.177
507	0.25
517	0.353
528	0.5
539	0.707
551	1.0
564	1.41
577	2.0
591	2.83
605	4.0
620	5.66
636	8.0
653	11.314
671	16.0
689	22.63

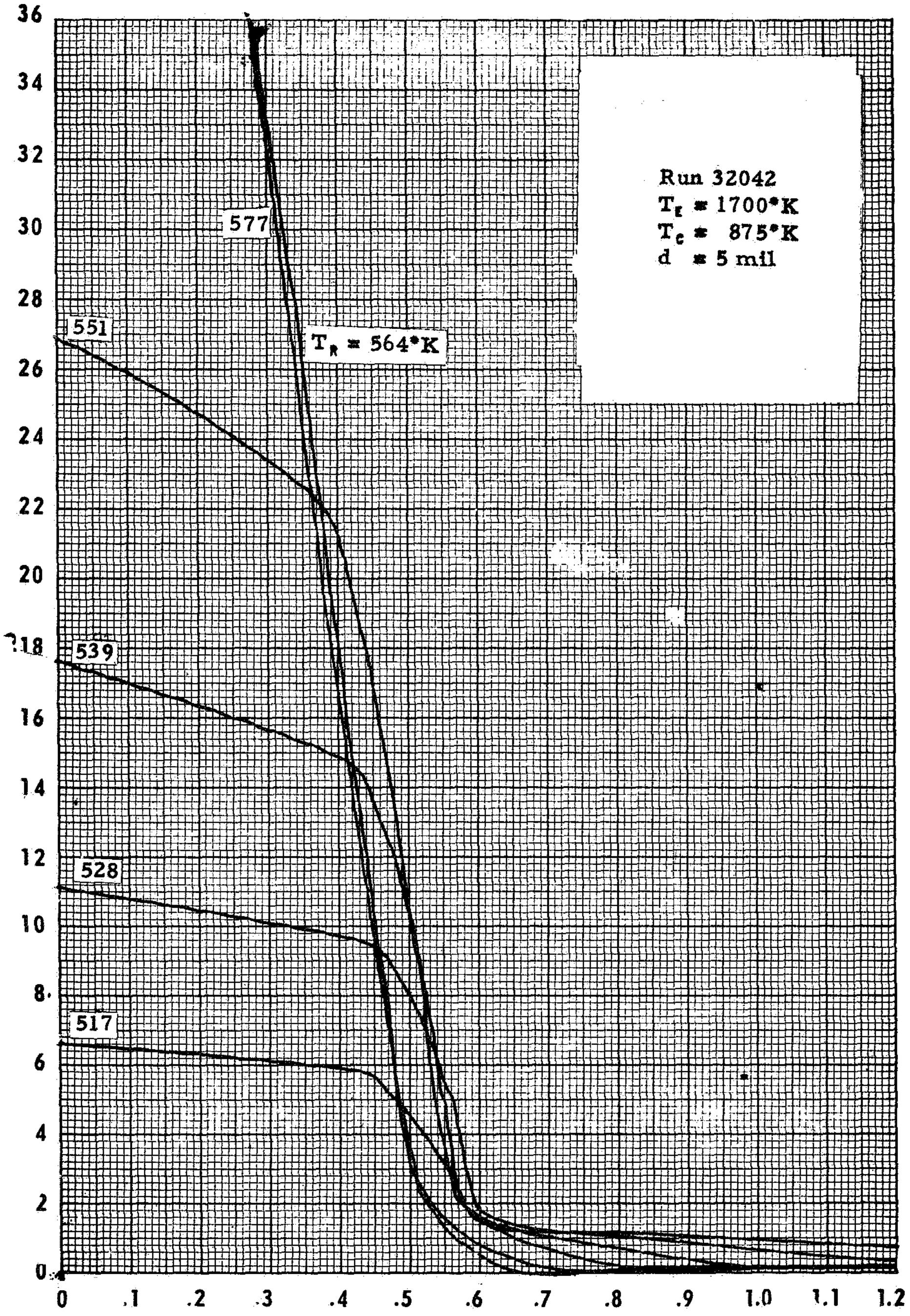
36
34
32
30
28
26
24
22
20
18
16
14
12
10
8
6
4
2
0
0
.1
.2
.3
.4
.5
.6
.7
.8
.9
1.0
1.1
1.2
577
551
539
528
517
T_R = 564°K
Run 32042
T_E = 1700°K
T_C = 875°K
d = 5 mil

Figure IV-2

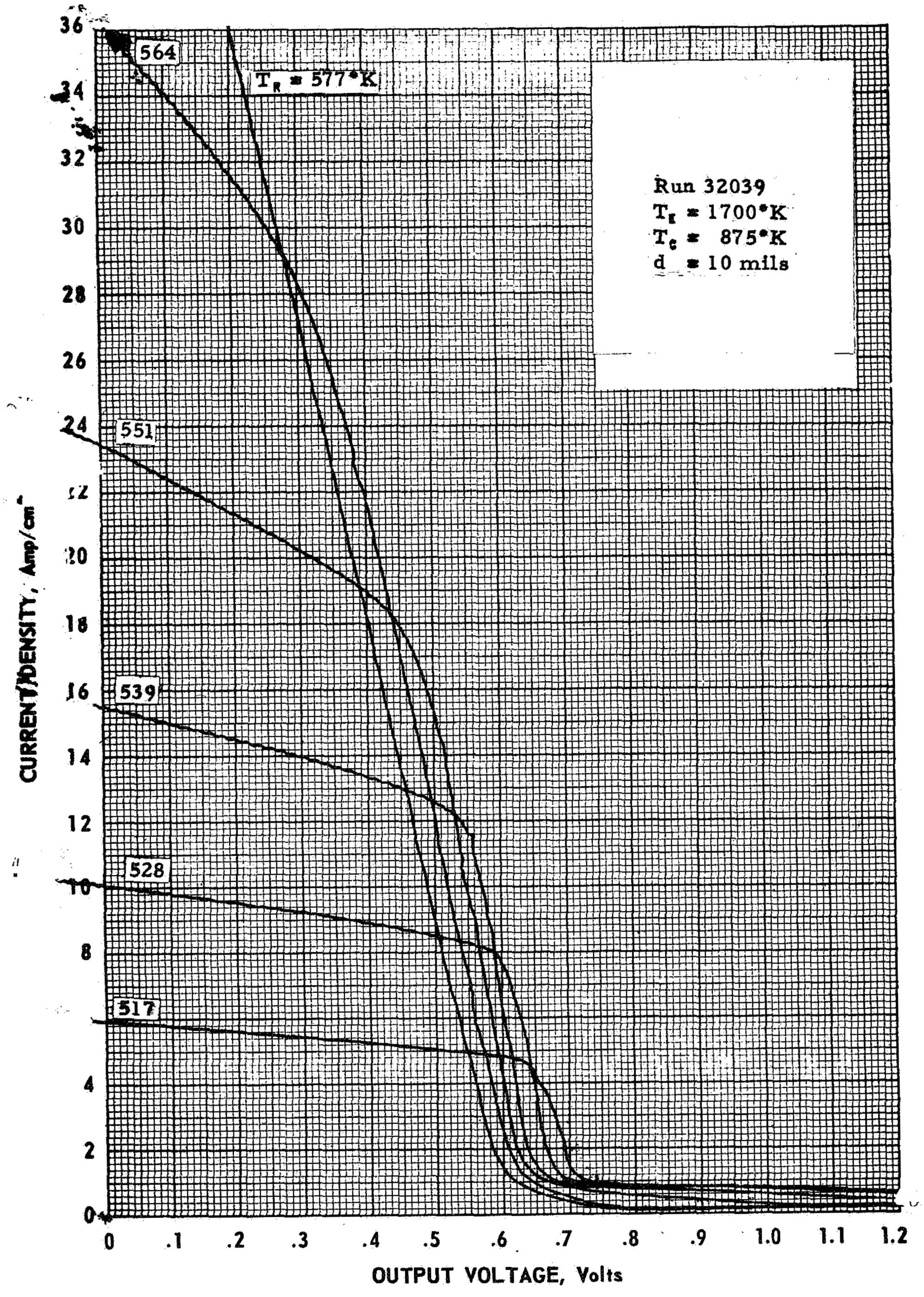
36
34
32
30
28
26
24
22
20
18
16
14
12
10
8
4
2
0
CURRENT DENSITY, Amp/cm²
564
551
539
528
517
T_R = 577°K
Run 32039
T_E = 1700°K
T_C = 875°K
d = 10 mils
0
.1
.2
.3
.4
.5
.6
.7
.8
.9
1.0
1.1
1.2
OUTPUT VOLTAGE, Volts

Figure IV-3

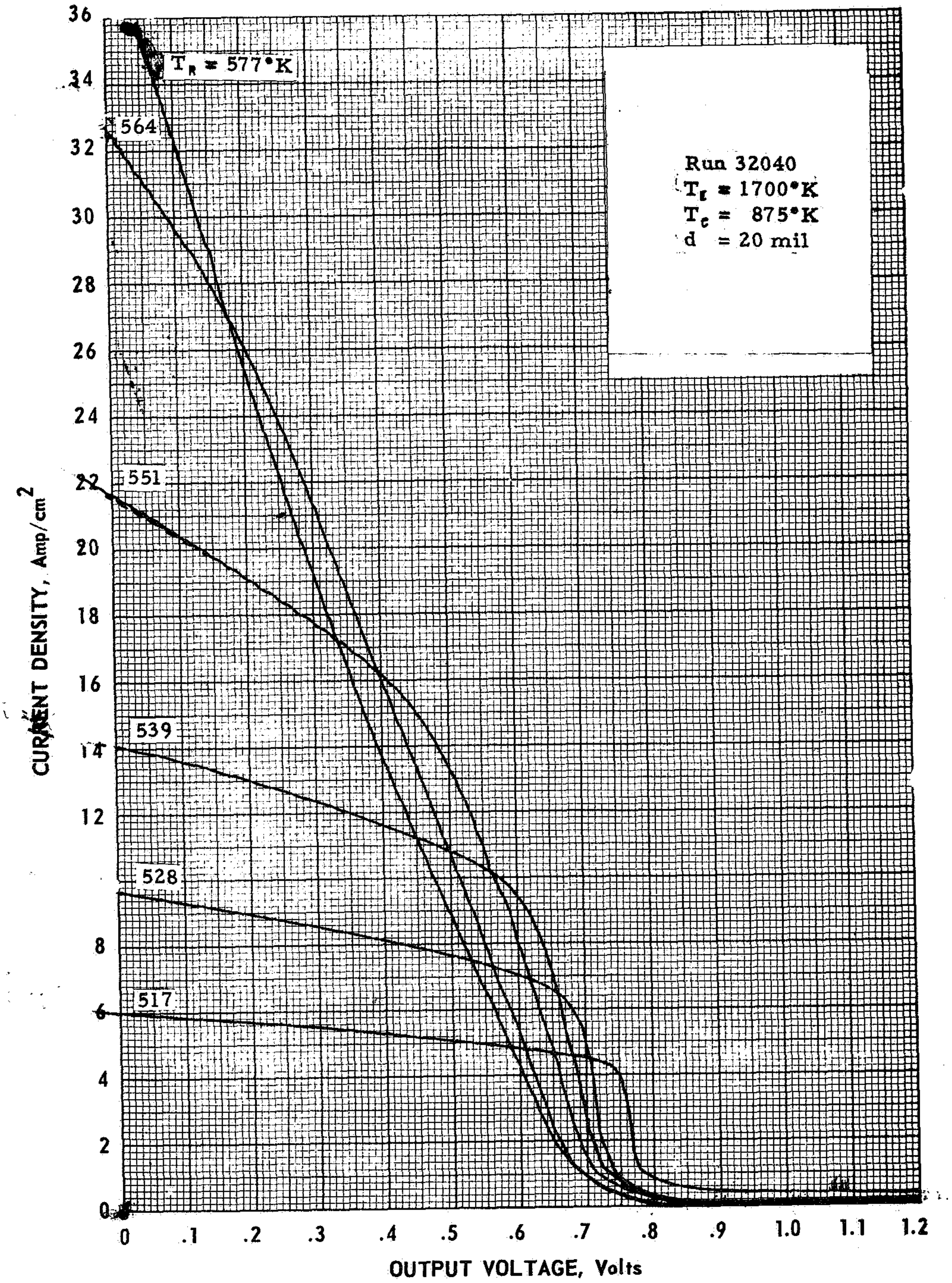
T_R = 577°K
564
551
539
528
517
Run 32040
T_E = 1700°K
T_C = 875°K
d = 20 mil
CURRENT DENSITY, Amp/cm^2
36
34
32
30
28
26
24
22
20
18
16
14
12
8
6
4
2
0
0
.1
.2
.3
.4
.5
.6
.7
.8
.9
1.0
1.1
1.2
OUTPUT VOLTAGE, Volts

Figure IV-4

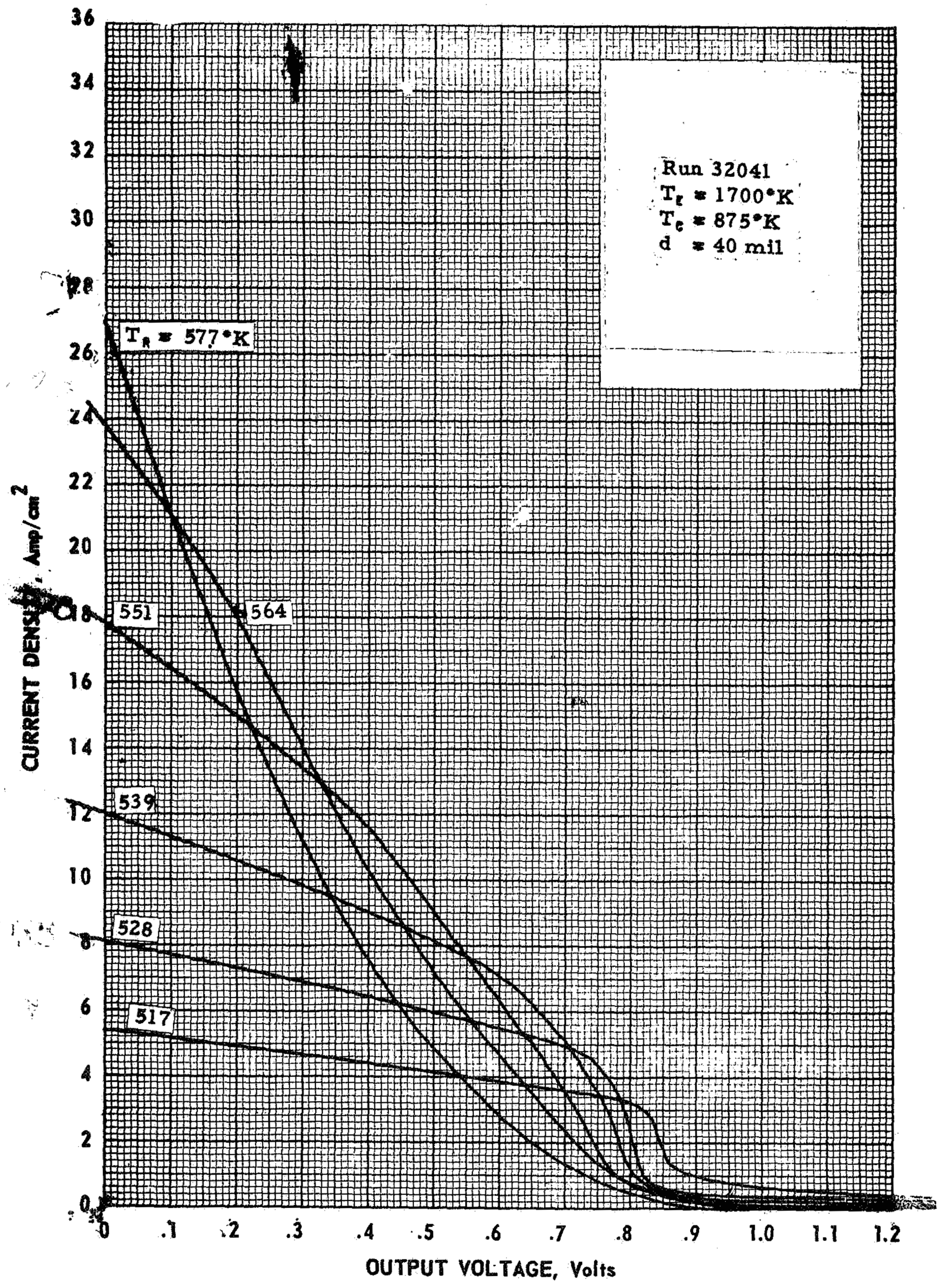
Run 32041
T_E = 1700°K
T_C = 875°K
d = 40 mil
T_R = 577°K
564
551
539
528
517
CURRENT DENSITY, Amp/cm^2
0
2
4
6
8
10
12
14
16
18
20
22
24
26
28
30
32
34
36
OUTPUT VOLTAGE, Volts
0
.1
.2
.3
.4
.5
.6
.7
.8
.9
1.0
1.1
1.2

Figure IV-5

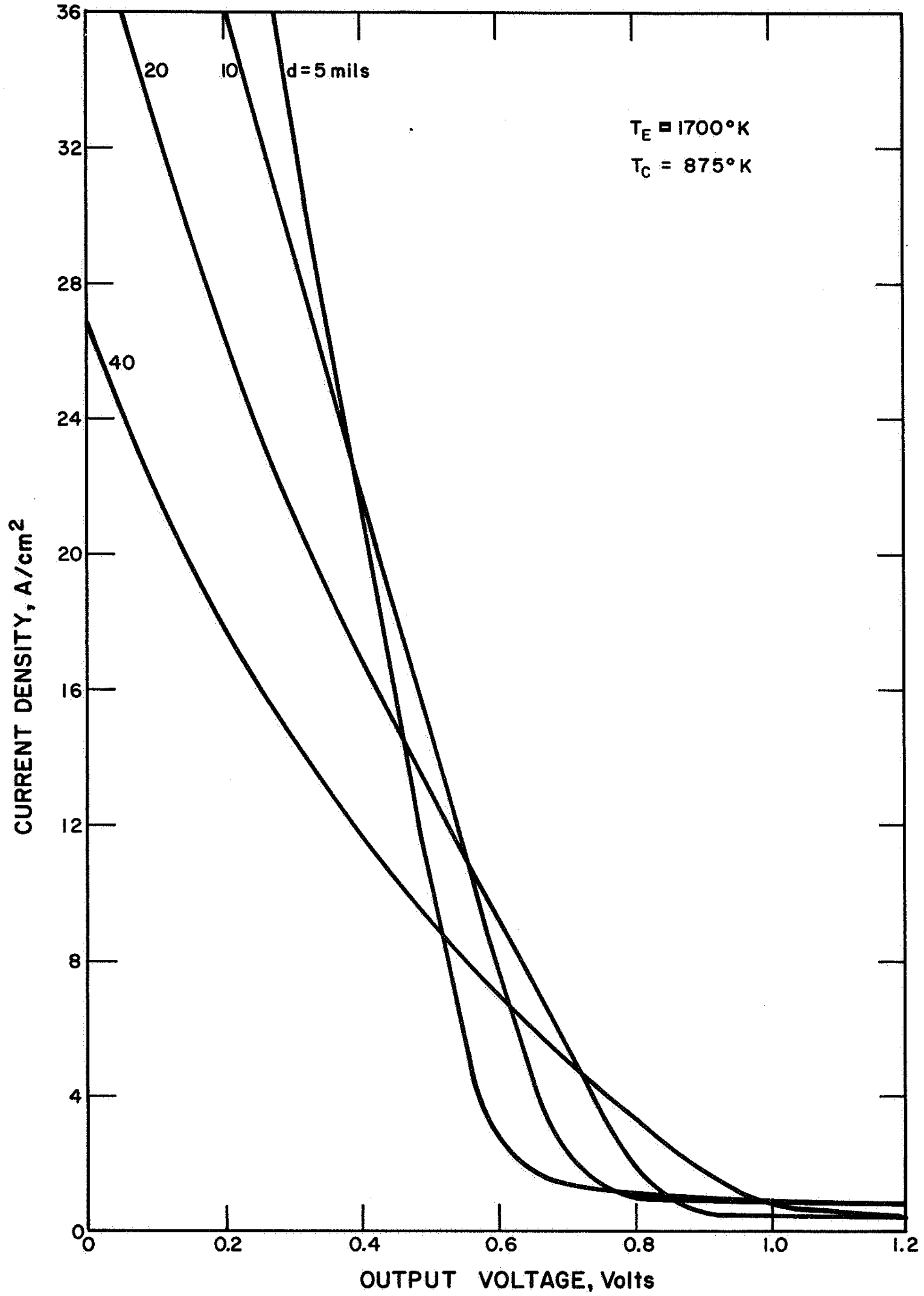
36
32
28
24
20
16
12
8
4
0
0
0.2
0.4
0.6
0.8
1.0
1.2
CURRENT DENSITY, A/cm^2
OUTPUT VOLTAGE, Volts
20
10
d=5 mils
40
T_E = 1700°K
T_C = 875°K

Figure IV-6

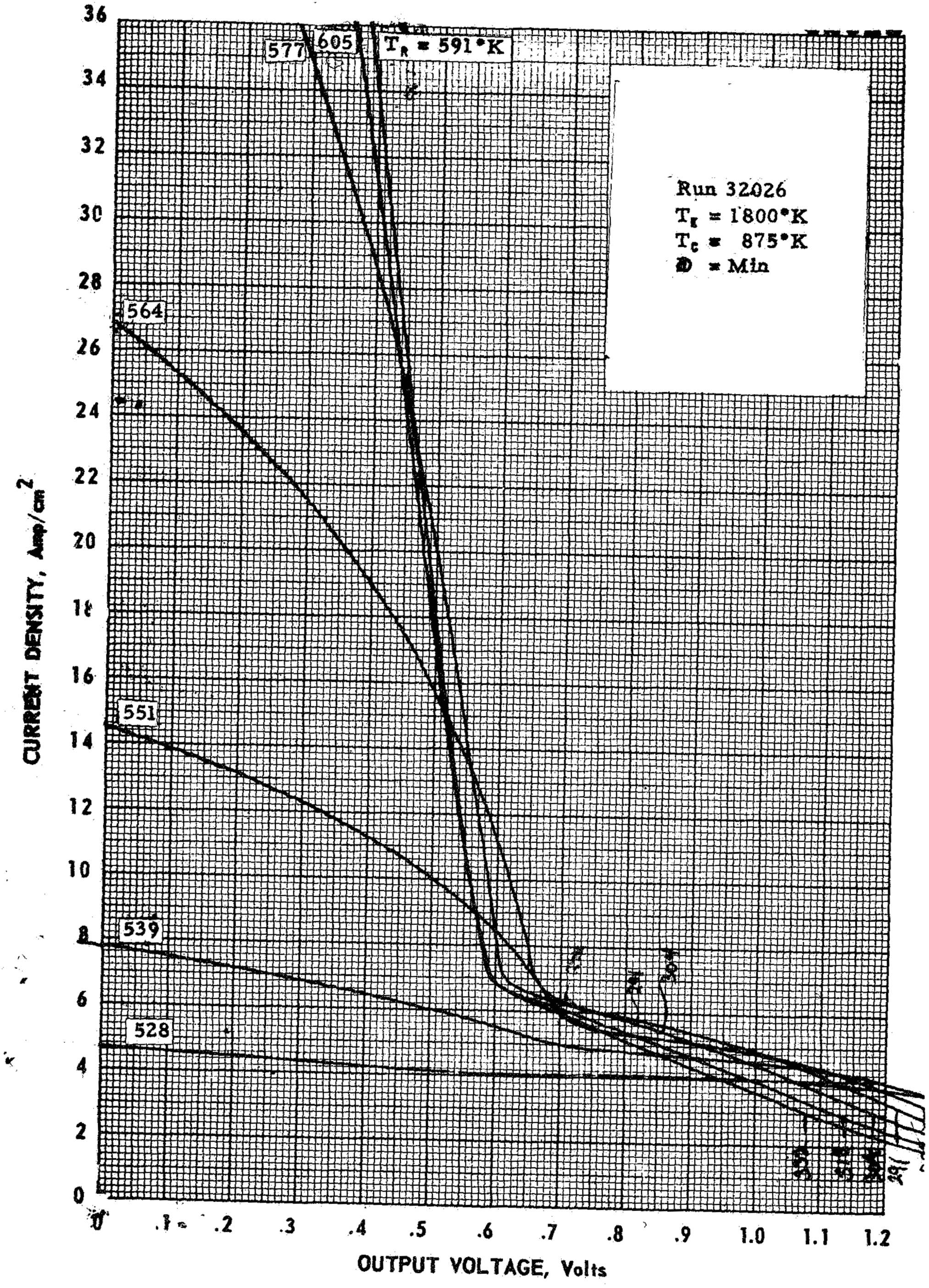
36
34
32
30
28
26
24
22
20
18
16
14
12
10
8
6
4
2
0
CURRENT DENSITY, Amp/cm²
0
.1
.2
.3
.4
.5
.6
.7
.8
.9
1.0
1.1
1.2
OUTPUT VOLTAGE, Volts
577
605
T_R = 591°K
564
551
539
528
Run 32026
T_E = 1800°K
T_C = 875°K
Φ = Min

Figure IV-7

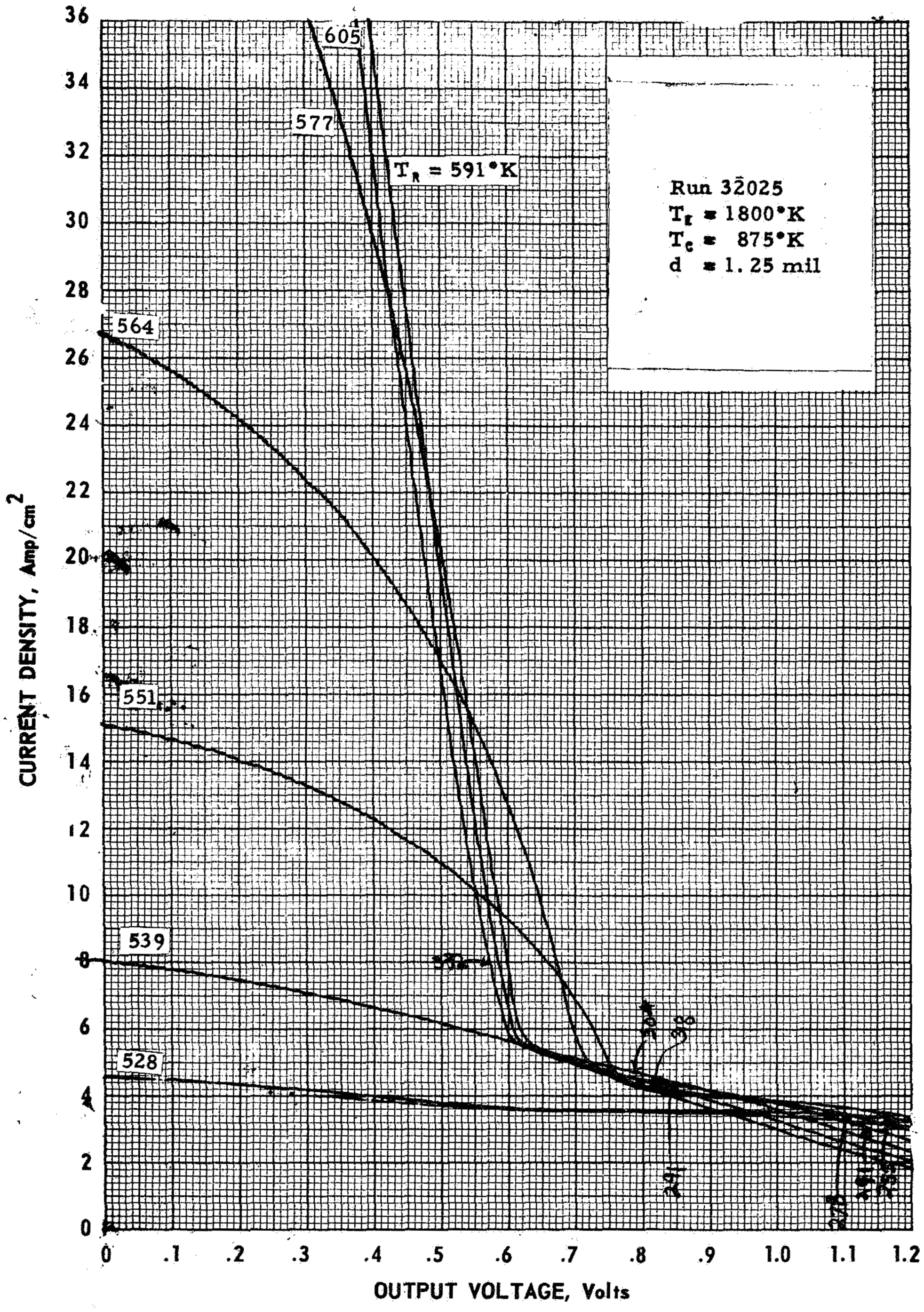
Run 32025
T_E = 1800°K
T_C = 875°K
d = 1.25 mil
T_R = 591°K
605
577
564
551
539
528
532
304
318
291
278
CURRENT DENSITY, Amp/cm^2
0
2
4
6
8
10
12
14
16
18
20
22
24
26
28
30
32
34
36
OUTPUT VOLTAGE, Volts
0
.1
.2
.3
.4
.5
.6
.7
.8
.9
1.0
1.1
1.2

Figure IV-8

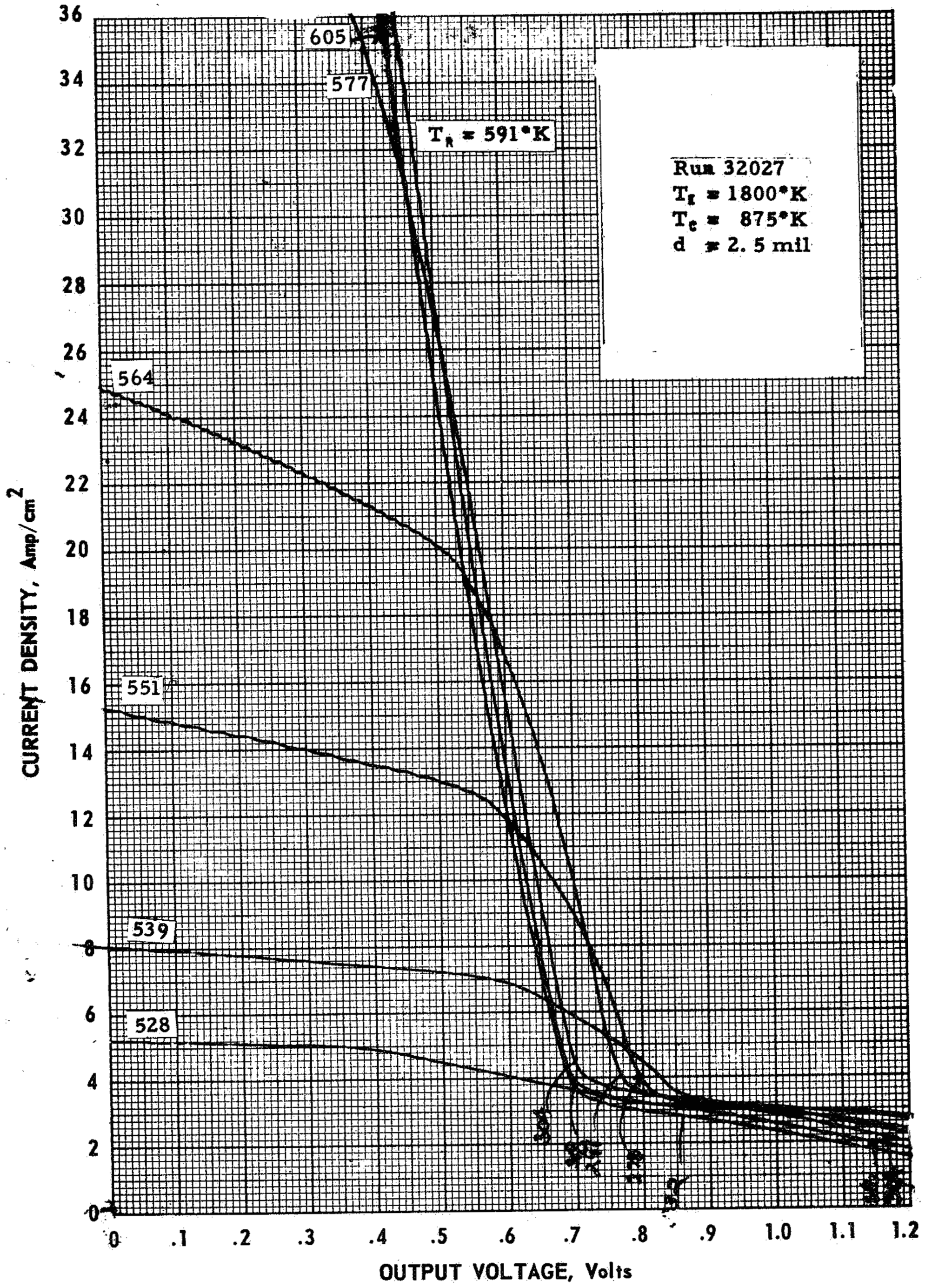
605
577
T_R = 591°K
Run 32027
T_E = 1800°K
T_C = 875°K
d = 2.5 mil
564
551
539
528
CURRENT DENSITY, Amp/cm^2
36
34
32
30
28
26
24
22
20
18
16
14
12
10
8
6
4
2
0
0
.1
.2
.3
.4
.5
.6
.7
.8
.9
1.0
1.1
1.2
OUTPUT VOLTAGE, Volts

Figure IV-9

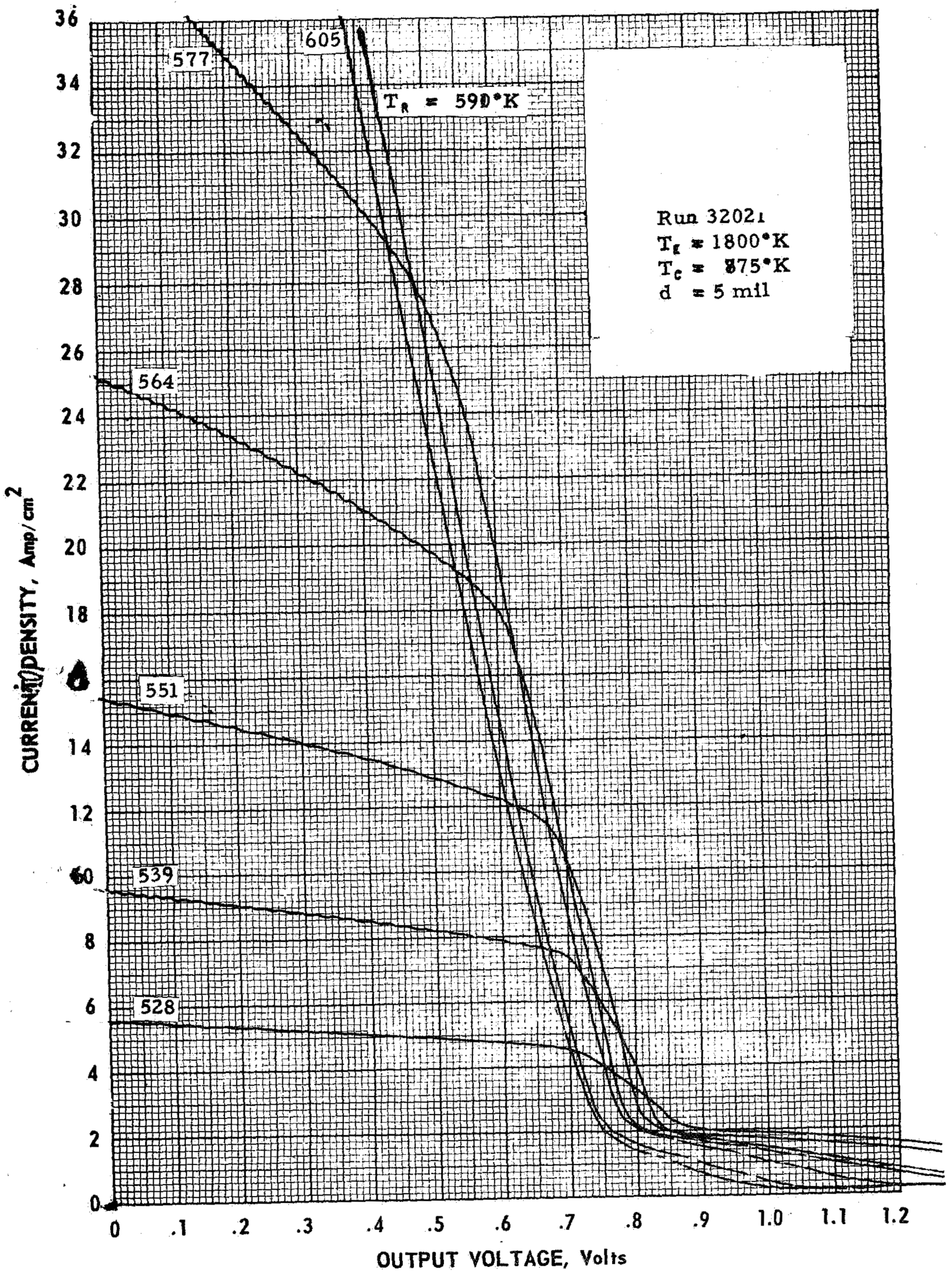
CURRENT DENSITY, Amp/cm^2
0
2
4
6
8
10
12
14
16
18
20
22
24
26
28
30
32
34
36
0
.1
.2
.3
.4
.5
.6
.7
.8
.9
1.0
1.1
1.2
OUTPUT VOLTAGE, Volts
577
605
T_R = 590°K
564
551
539
528
Run 32021
T_E = 1800°K
T_C = 875°K
d = 5 mil

Figure IV-10

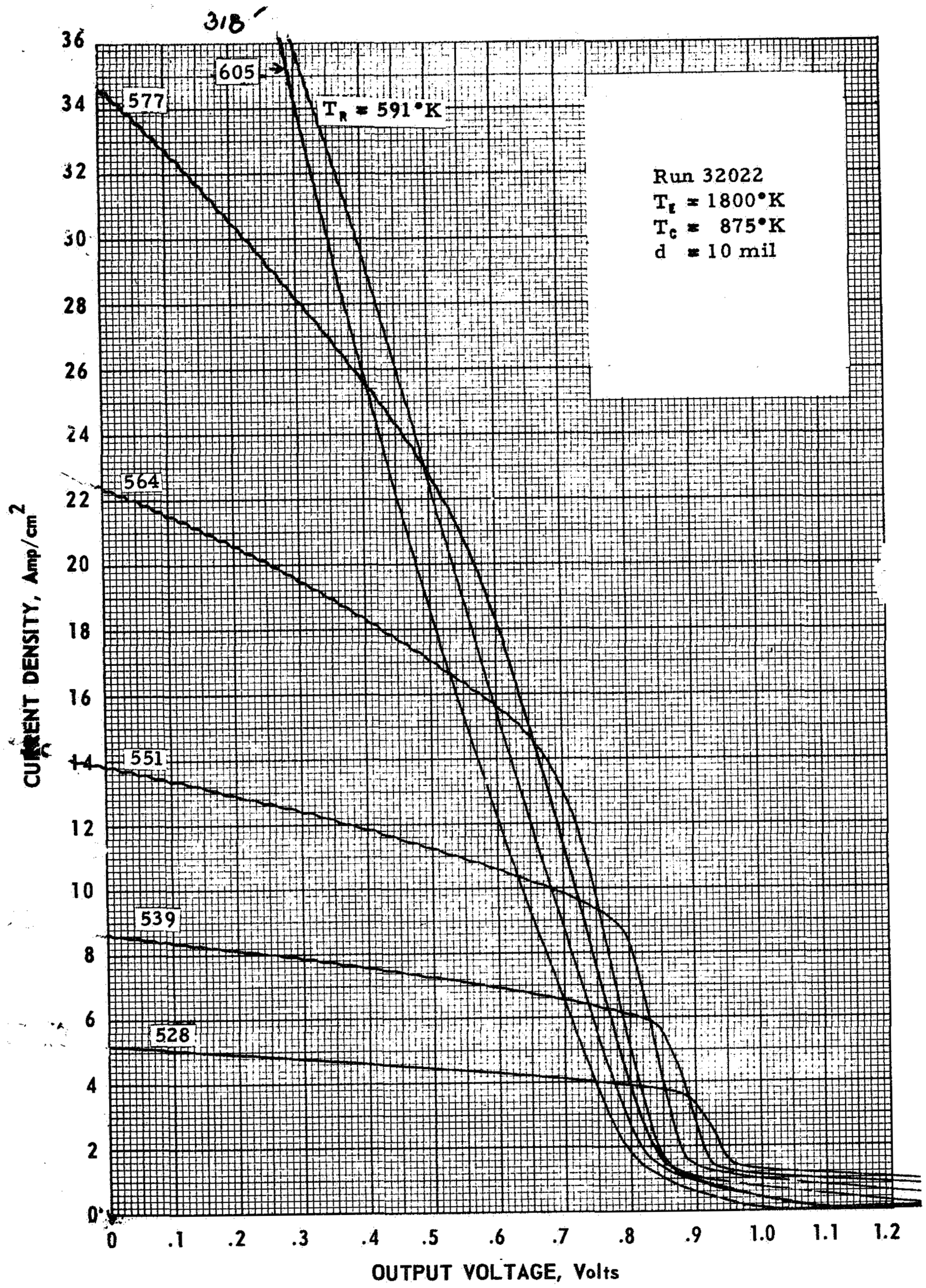
318
605
577
T_R = 591°K
564
551
539
528
Run 32022
T_E = 1800°K
T_C = 875°K
d = 10 mil
CURRENT DENSITY, Amp/cm^2
36
34
32
30
28
26
24
22
20
18
16
14
12
10
8
6
4
2
0
0
.1
.2
.3
.4
.5
.6
.7
.8
.9
1.0
1.1
1.2
OUTPUT VOLTAGE, Volts

Figure IV-11

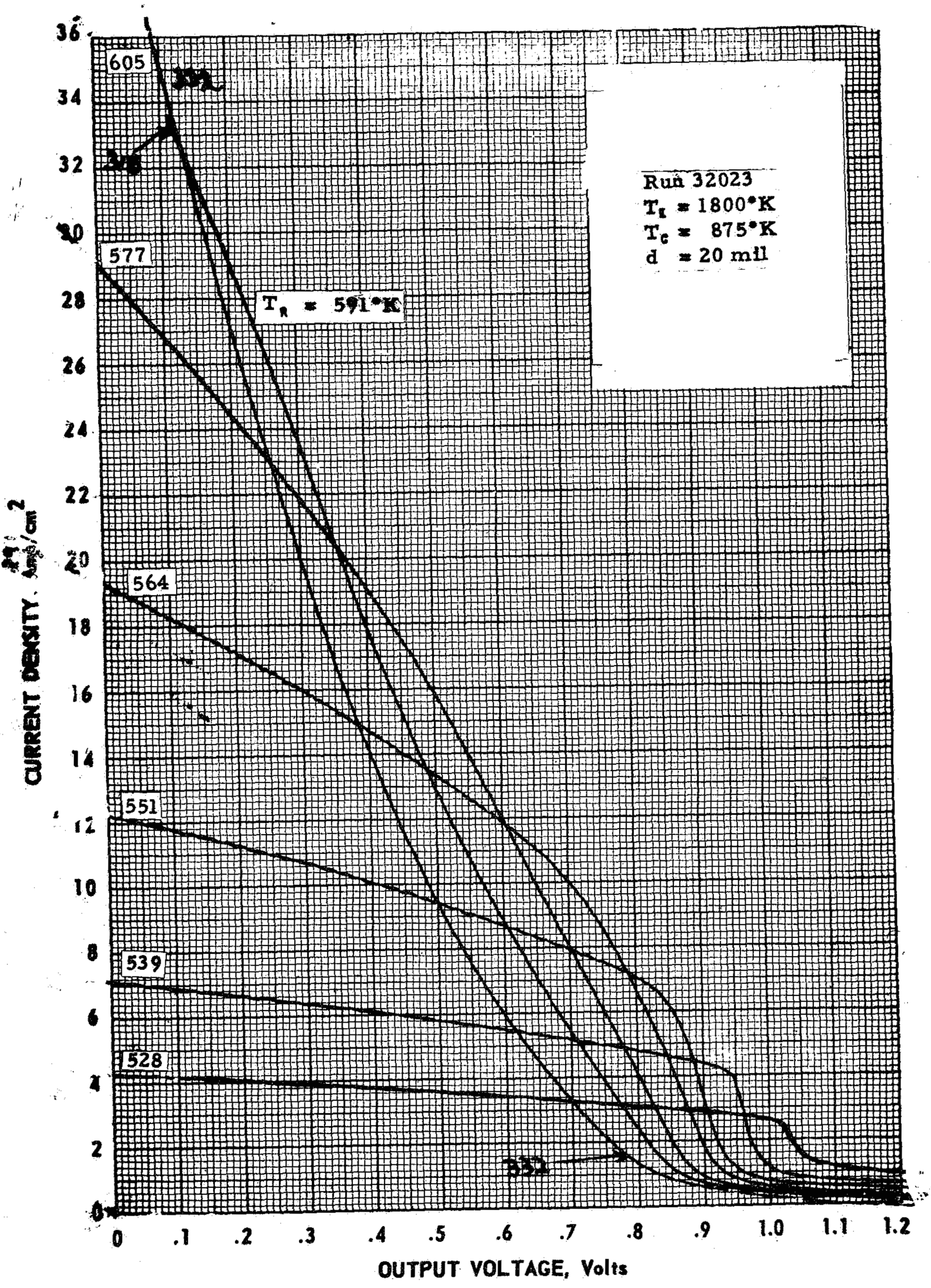
36
34
32
30
28
26
24
22
20
18
16
14
12
10
8
6
4
2
0
CURRENT DENSITY, Amps/cm²
0
.1
.2
.3
.4
.5
.6
.7
.8
.9
1.0
1.1
1.2
OUTPUT VOLTAGE, Volts
605
577
564
551
539
528
532
T_R = 591°K
Run 32023
T_E = 1800°K
T_C = 875°K
d = 20 mil

Figure IV-12

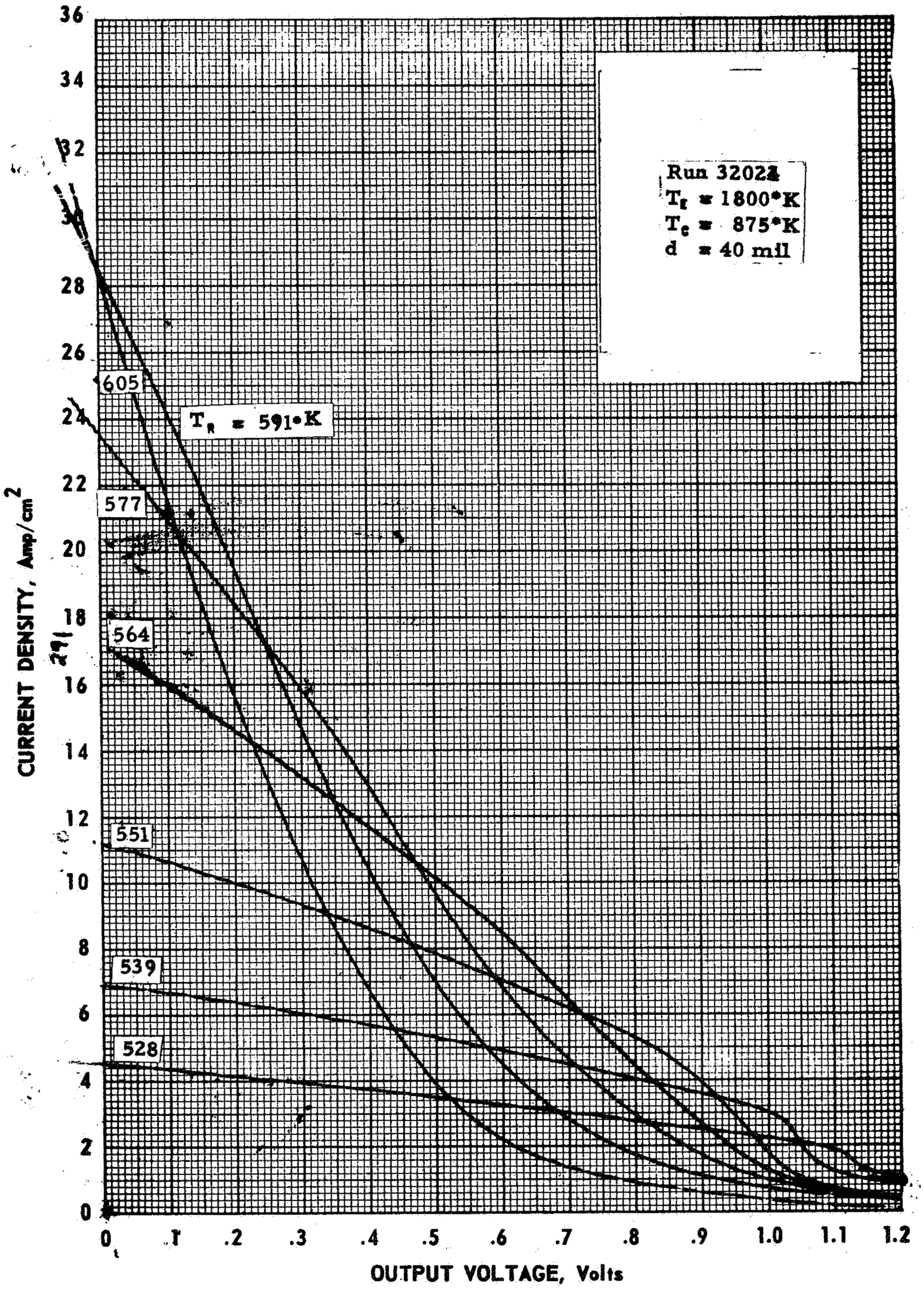
Run 32022
T_E = 1800°K
T_C = 875°K
d = 40 mil
T_R = 591°K
605
577
564
551
539
528
CURRENT DENSITY, Amp/cm^2
OUTPUT VOLTAGE, Volts
0
2
4
6
8
10
12
14
16
18
20
22
24
26
28
30
32
34
36
0
.1
.2
.3
.4
.5
.6
.7
.8
.9
1.0
1.1
1.2

Figure IV-13

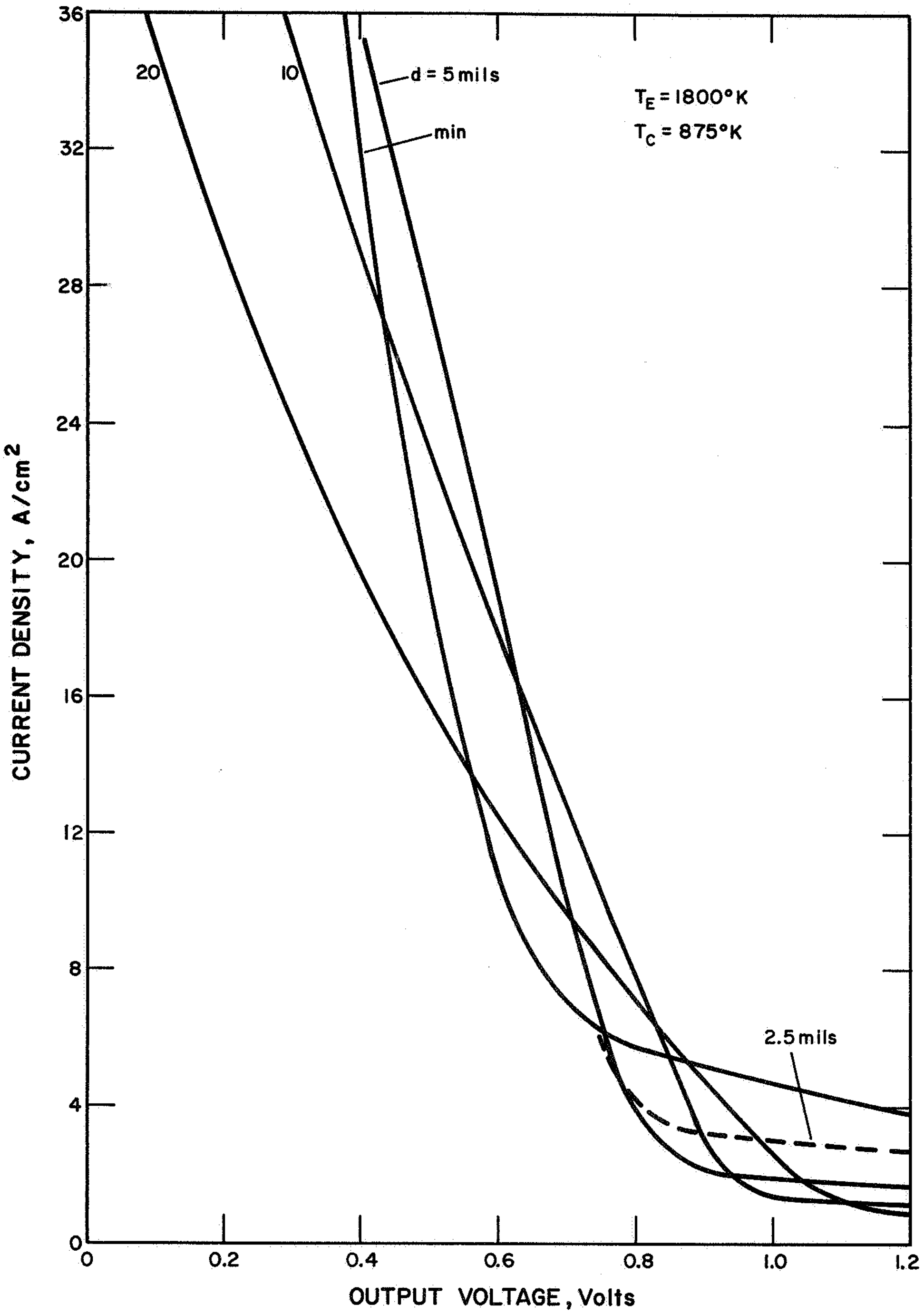
36
32
28
24
20
16
12
8
4
0
CURRENT DENSITY, A/cm²
0
0.2
0.4
0.6
0.8
1.0
1.2
OUTPUT VOLTAGE, Volts
20
10
d = 5 mils
min
2.5 mils
T_E = 1800°K
T_C = 875°K

Figure IV-14

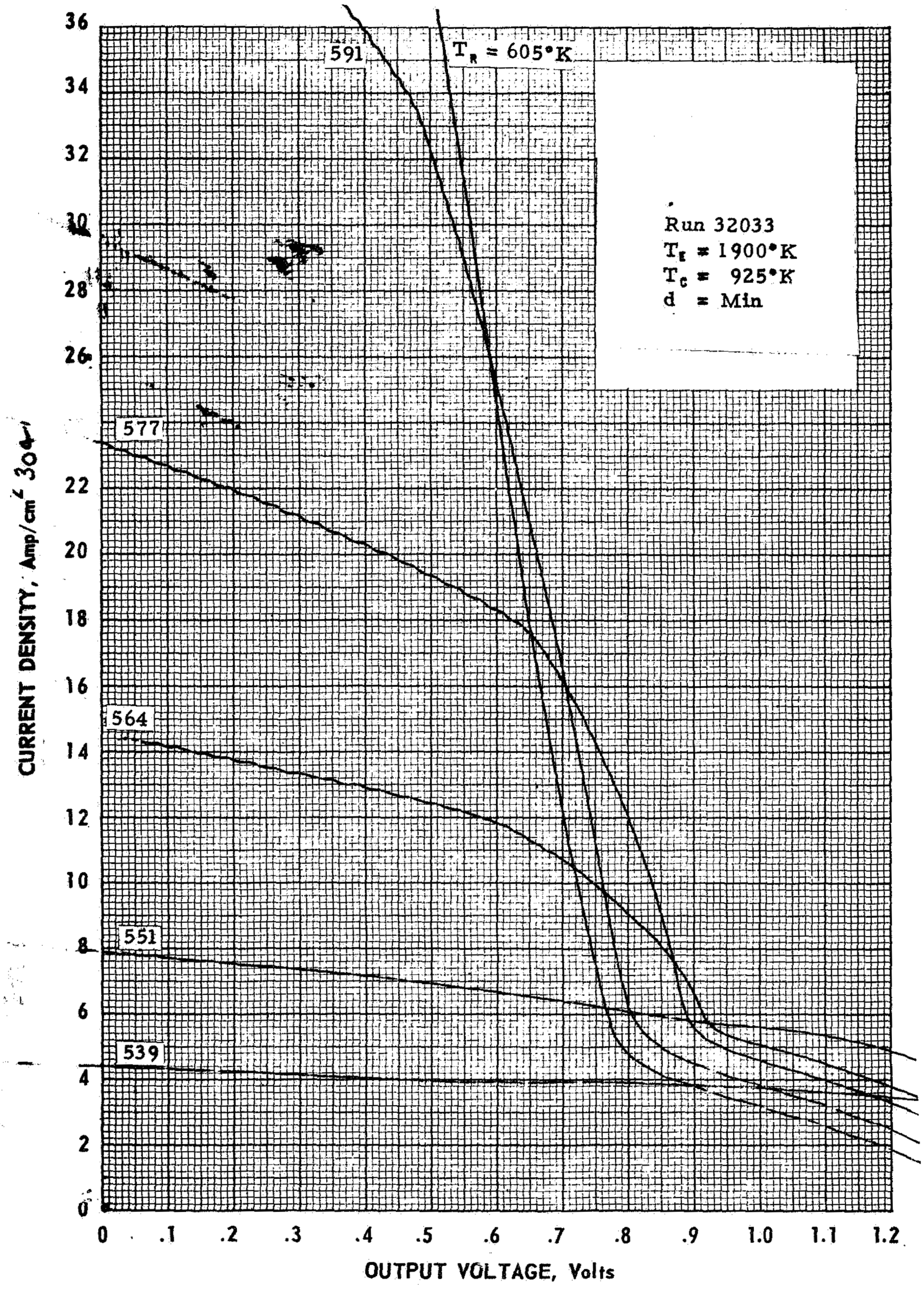
591
$T_R = 605°K$
Run 32033
T_E = 1900°K
T_C = 925°K
d = Min
577
564
551
539
CURRENT DENSITY, Amp/cm^2
36
34
32
30
28
26
22
20
18
16
14
12
10
8
6
4
2
0
0
.1
.2
.3
.4
.5
.6
.7
.8
.9
1.0
1.1
1.2
OUTPUT VOLTAGE, Volts

Figure IV-15

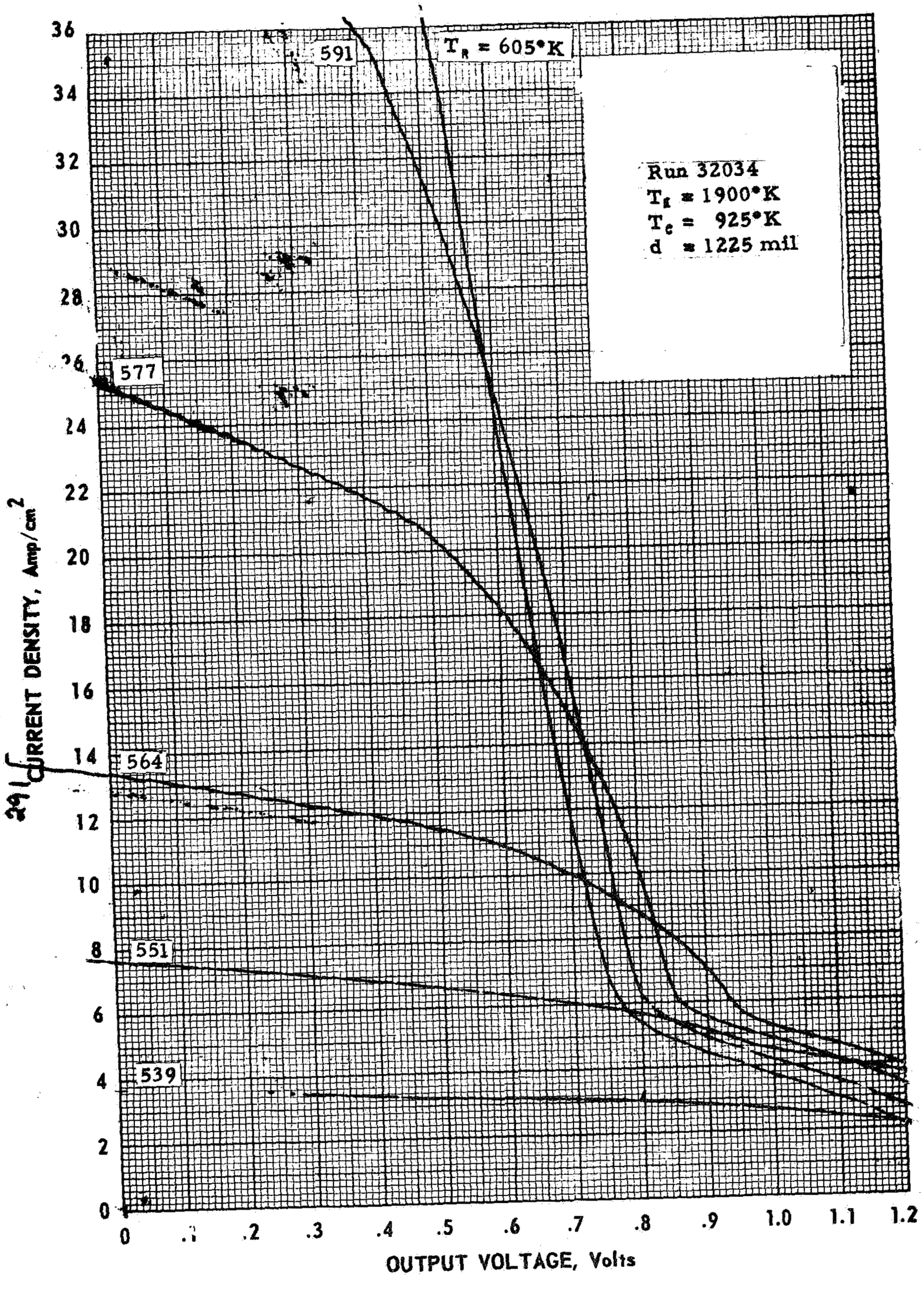
591
T_R = 605°K
Run 32034
T_E = 1900°K
T_c = 925°K
d = 1225 mil
577
564
551
539
CURRENT DENSITY, Amp/cm²
36
34
32
30
28
26
24
22
20
18
16
14
12
10
8
6
4
2
0
0
.1
.2
.3
.4
.5
.6
.7
.8
.9
1.0
1.1
1.2
OUTPUT VOLTAGE, Volts

Figure IV-16

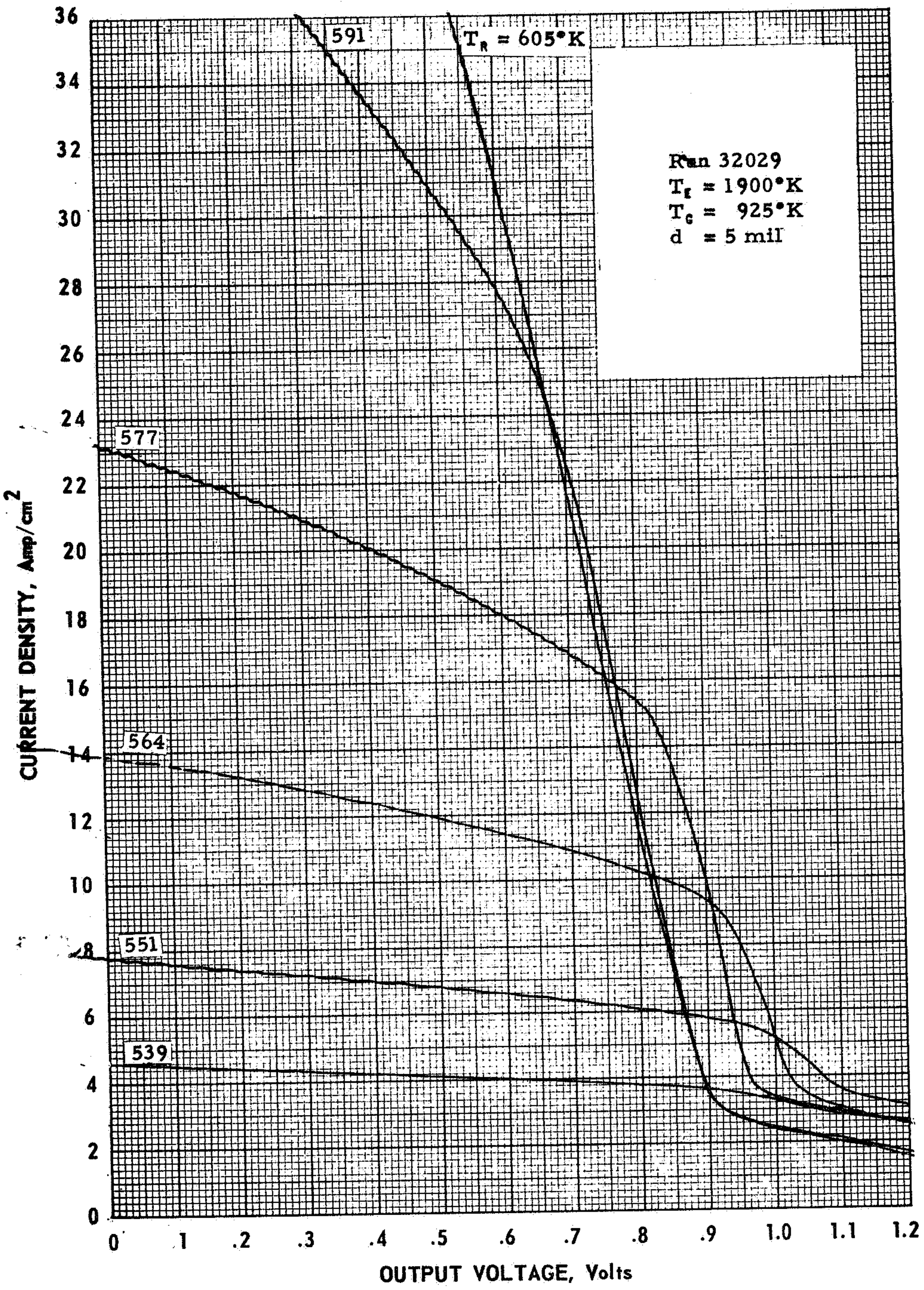
591
T_R = 605°K
Run 32029
T_E = 1900°K
T_C = 925°K
d = 5 mil
577
564
551
539
CURRENT DENSITY, Amp/cm^2
0
2
4
6
8
10
12
14
16
18
20
22
24
26
28
30
32
34
36
OUTPUT VOLTAGE, Volts
0
.1
.2
.3
.4
.5
.6
.7
.8
.9
1.0
1.1
1.2

Figure IV-17

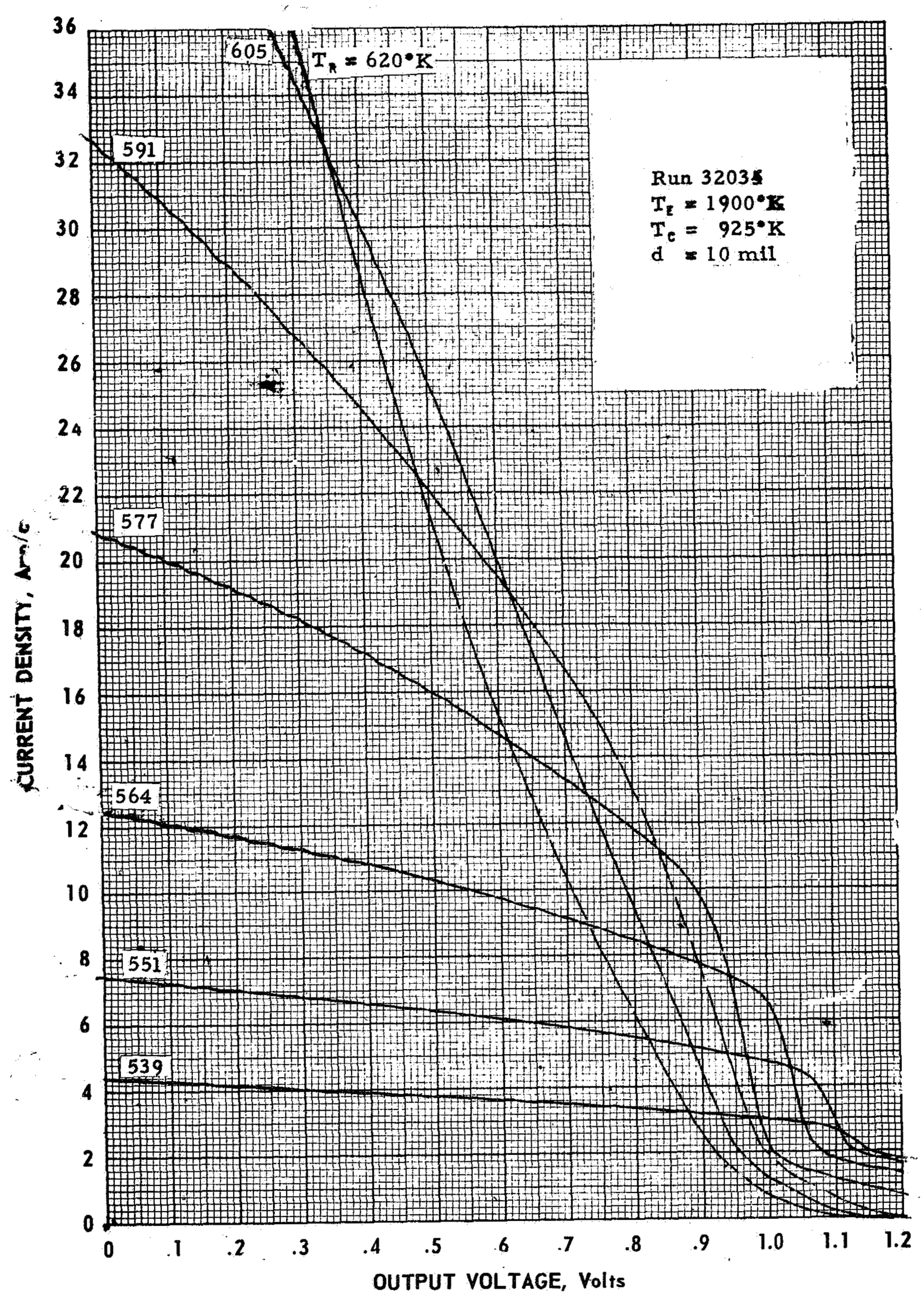
605
T_R = 620°K
591
577
564
551
539
Run 32035
T_E = 1900°K
T_c = 925°K
d = 10 mil
CURRENT DENSITY, Amp/c
36
34
32
30
28
26
24
22
20
18
16
14
12
10
8
6
4
2
0
0
.1
.2
.3
.4
.5
.6
.7
.8
.9
1.0
1.1
1.2
OUTPUT VOLTAGE, Volts

Figure IV-18

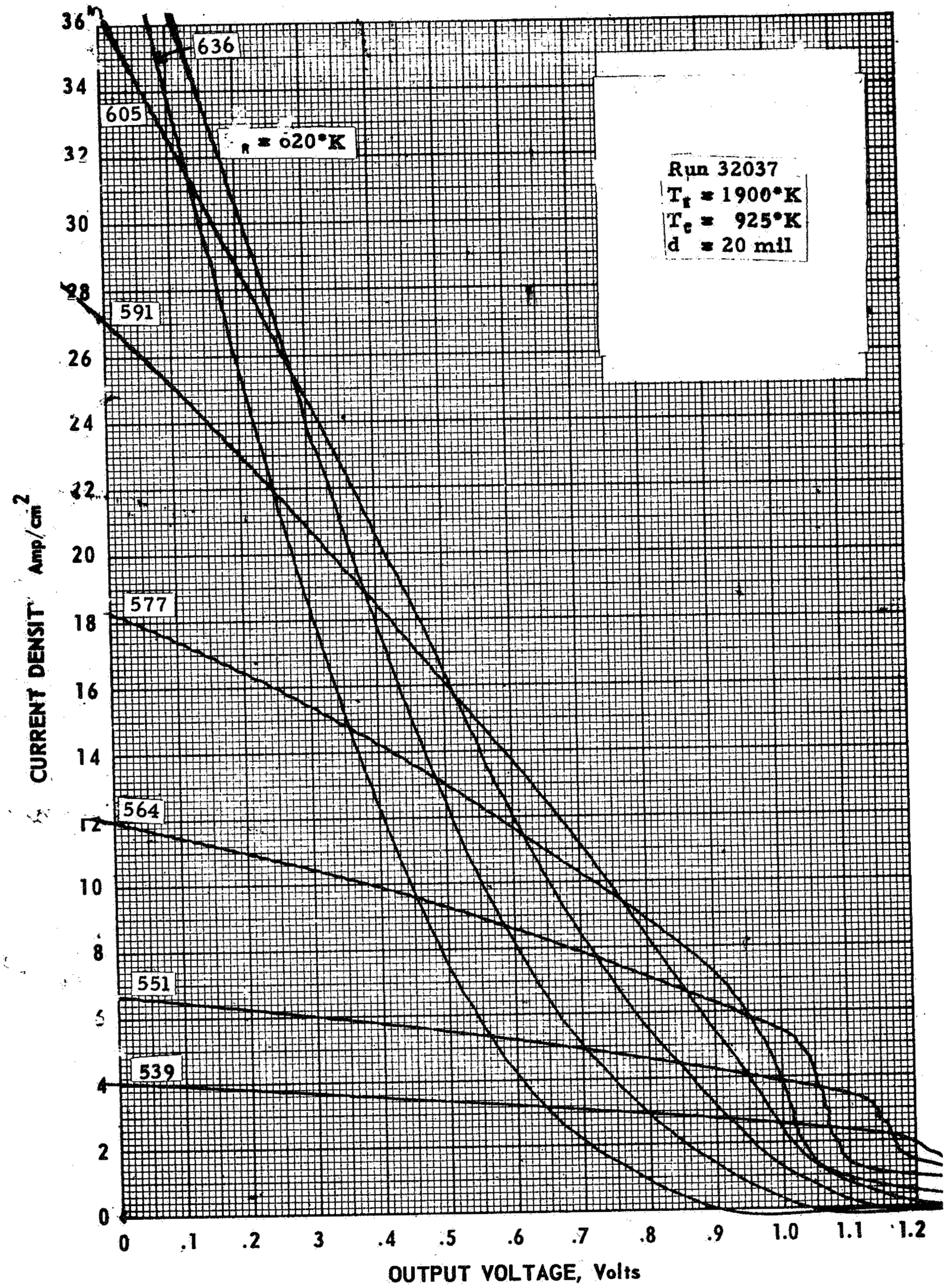
636
605
591
577
564
551
539
T_R = 620°K
Run 32037
T_E = 1900°K
T_C = 925°K
d = 20 mil
CURRENT DENSITY Amp/cm^2
36
34
32
30
28
26
24
22
20
18
16
14
12
10
8
6
4
2
0
0
.1
.2
3
.4
.5
.6
.7
.8
.9
1.0
1.1
1.2
OUTPUT VOLTAGE, Volts

Figure IV-19

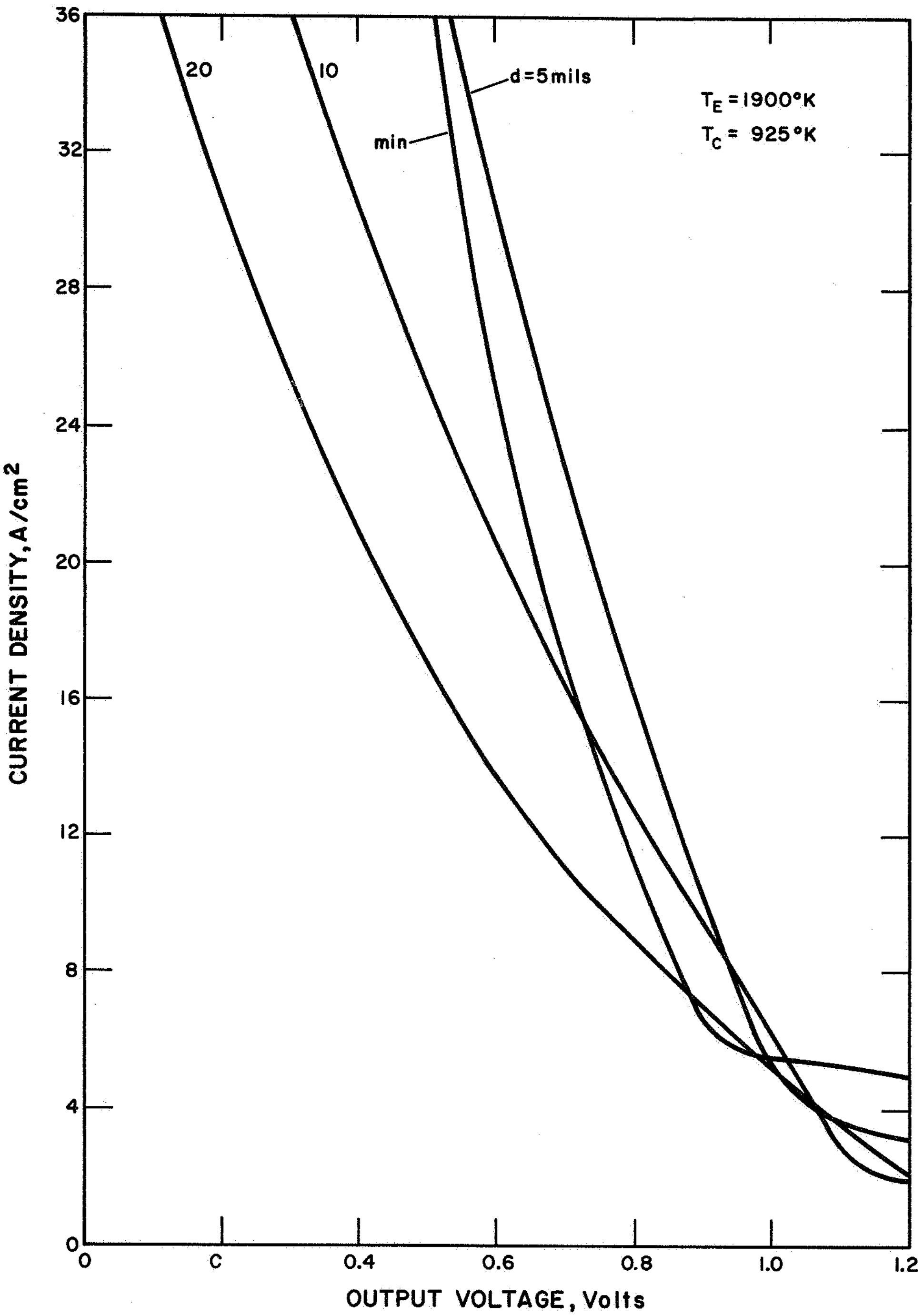
36
32
28
24
20
16
12
8
4
0
CURRENT DENSITY, A/cm2
0
C
0.4
0.6
0.8
1.0
1.2
OUTPUT VOLTAGE, Volts
20
10
min
d=5mils
T_E = 1900°K
T_C = 925°K

Figure IV-20

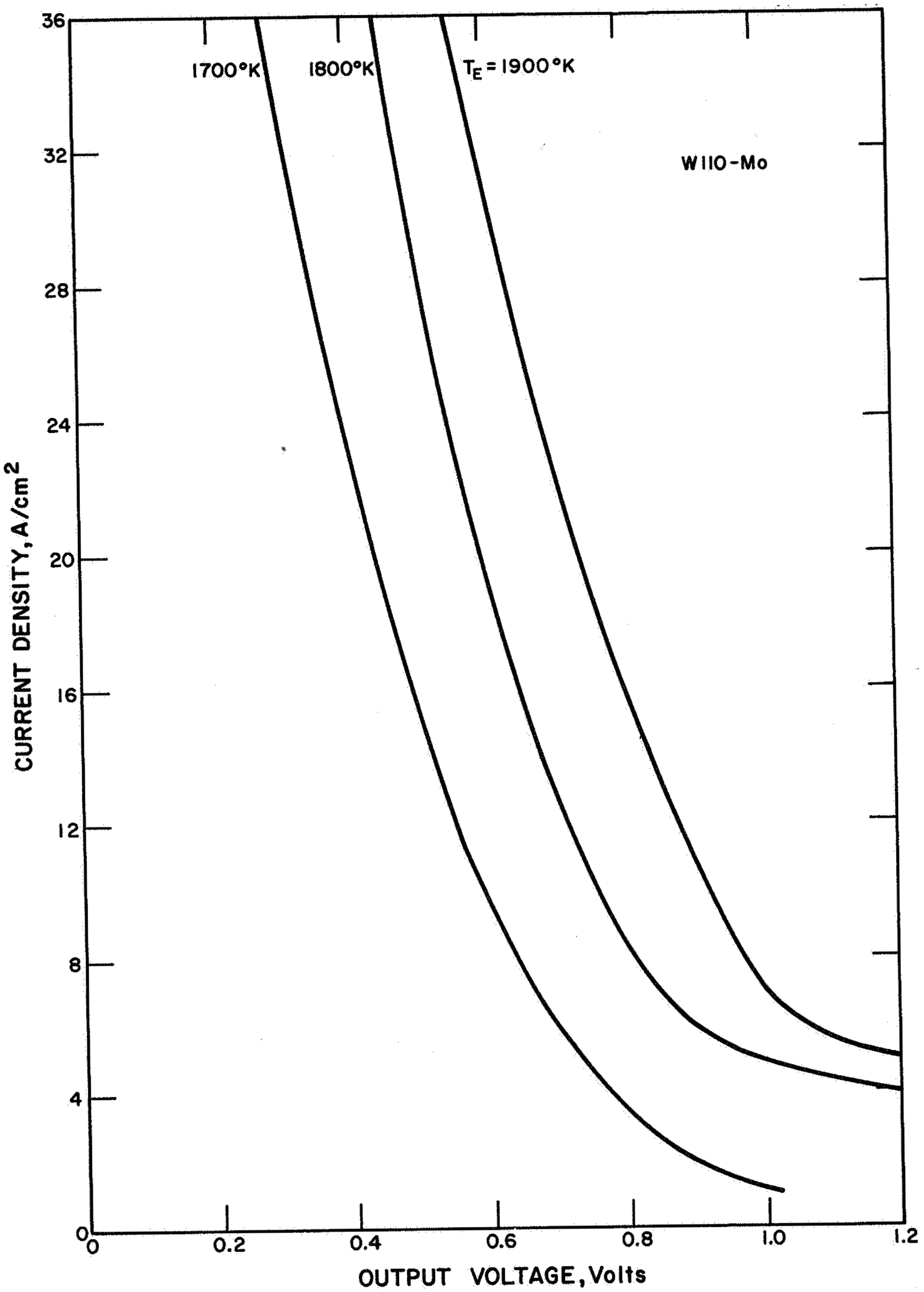
CURRENT DENSITY, A/cm²
OUTPUT VOLTAGE, Volts
1700°K
1800°K
T_E = 1900°K
W110-Mo
0
4
8
12
16
20
24
28
32
36
0
0.2
0.4
0.6
0.8
1.0
1.2

Figure IV-21

fully optimized envelopes of this converter are compared with those of an etched Re:Mo converter (Figure IV-22). The W110-Mo converter is better than the etched Re-Mo converter by about 60 to 120 millivolts. A comparison at an interelectrode spacing of 10 mils is shown in Figure IV-23. The increase in output power by about a factor of two is probably due to the better uniformity in the emitter surface.

B. SPACING MECHANISM

A new spacing mechanism, shown in Figure IV-24, was designed for the variable-spacing converter in order to simplify the assembly and increase the rigidity of the system.

The converter is located by the " guard support plate," which contacts the guard and establishes the spacing reference. Three threaded rods support the various elements of the converter and provide mounting adjustments. The ceramic rods extend between the emitter support plate and the micrometers to form the spacing regulator, and the three springs provide the required tension to move the emitter and to maintain the proper contact between the ceramic rods and the micrometers. The guard support plate is split and is assembled around the converter; clamp screws ensure the rigidity of this assembly. Ceramic inserts between the plate and the guard reduce the heat conducted to the plate.

Spacing control is obtained by varying the distance from the emitter support plate to the guard support plate by means of the micrometers. A ball between the ceramic rod and the micrometer shaft allows the shaft to rotate freely without erratically affecting the spacing. The low heat conductivity and low thermal expansion of the rods and the water cooling for the micrometers help to ensure stability with varying converter temperatures. Tension in the springs forces the emitter support plate to follow the micrometers as they are adjusted to control the spacing. With this arrangement variations in collector and guard temperatures have little effect on the interelectrode spacing. Electrical leakage paths from emitter to collector are minimized by arranging the system so that all of the collector insulators are at guard potential rather than at emitter potential.

C. WORK FUNCTION CORRELATION

To examine the validity of theoretical expressions describing the plasma phenomena in thermionic converters, it is necessary to compare these expressions with experimental data for a wide range of converter operating conditions. Emitter work function is one of the most important parameters in the theoretical expressions, since it influences both electron emission and ion generation at the emitter surface. An accurate experimental measurement of emitter work function, however, can only be made under a narrow range of converter operating conditions, and the measured values must be extrapolated to cover the other regions of operation. In this section a new correlation technique is presented and compared with the T_E/T_R correlation.

The new correlation is based on the thermodynamic equation:

$$T \ln P = AT + B \tag{1}$$

where T is surface temperature, P is cesium pressure, and A and B are functions of the surface work function ϕ. The functions A and B are assumed to be of the form:

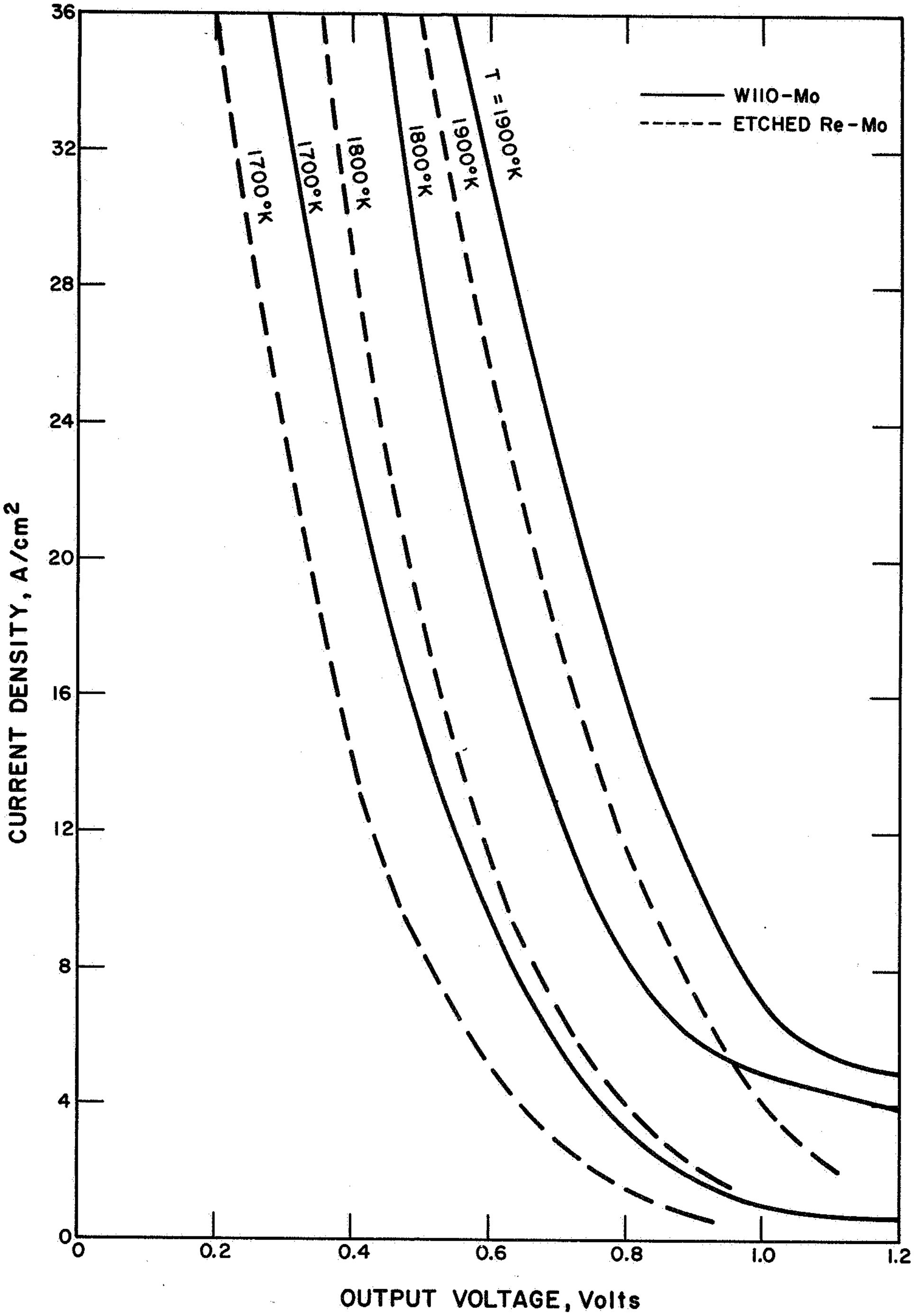
36
32
28
24
20
16
12
8
4
0
0
0.2
0.4
0.6
0.8
1.0
1.2
CURRENT DENSITY, A/cm²
OUTPUT VOLTAGE, Volts
W110-Mo
ETCHED Re-Mo
1700°K
1700°K
1800°K
1800°K
1900°K
T = 1900°K

Figure IV-22

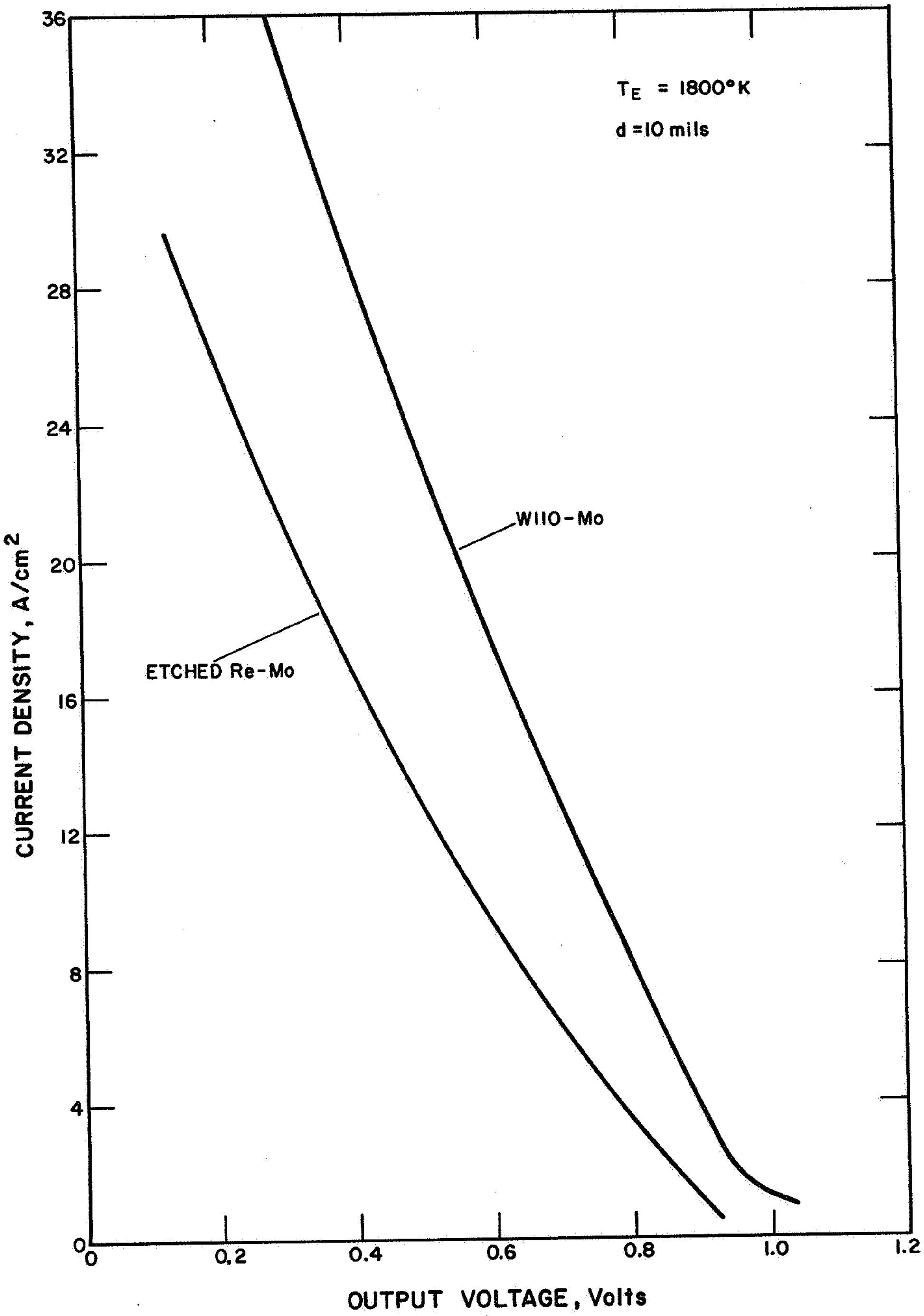
T_E = 1800°K
d = 10 mils
W110-Mo
ETCHED Re-Mo
CURRENT DENSITY, A/cm^2
0
4
8
12
16
20
24
28
32
36
0
0.2
0.4
0.6
0.8
1.0
1.2
OUTPUT VOLTAGE, Volts

Figure IV-23

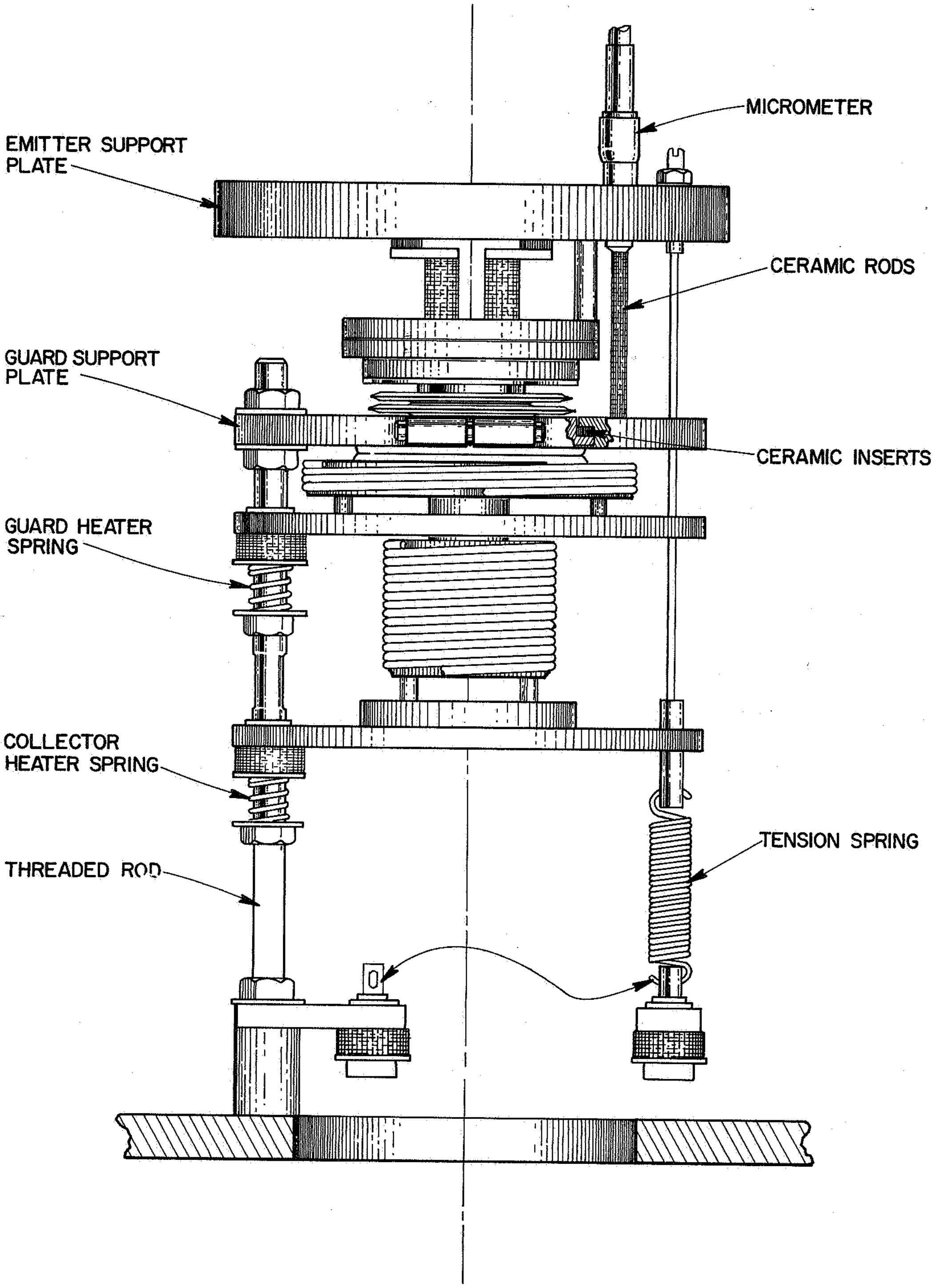
MICROMETER
EMITTER SUPPORT PLATE
CERAMIC RODS
GUARD SUPPORT PLATE
CERAMIC INSERTS
GUARD HEATER SPRING
COLLECTOR HEATER SPRING
TENSION SPRING
THREADED ROD

Figure IV-24

$$A = \alpha_1 \phi + \beta_1 \tag{2}$$

$$B = \alpha_2 \phi + \beta_2 \tag{3}$$

where α_1, α_2, β_1, and β_2 are constants. Equations 1 through 3 can be combined to give:

$$\ln P = (\alpha_2 \phi + \beta_2) \frac{1}{T} + \alpha_1 \phi + \beta_1 \tag{4}$$

This equation can be compared with experimental data in order to determine the constants α_1, α_2, β_1 and β_2.

The data used for this correlation is plotted as a function of kT ln P in Figure IV-25. A cross plot of the data in terms of ln P versus $\frac{1}{T}$ is shown in Figure IV-26. Each constant work function line has an intercept I and a slope S. According to Equation 4, the intercept and the slope are given by:

$$\begin{aligned} I &= \alpha_1 \phi + \beta_1 \\ S &= \alpha_2 \phi + \beta_2 \end{aligned} \tag{5}$$

The intercept I is determined from the constant-work-function lines and is plotted as a function of ϕ in Figure IV-27. The constants α_1 and β_1 are determined from a least-squares fit to the data.

$$\begin{aligned} \alpha_1 &= -1.04 \text{ torr/eV} \\ \beta_1 &= 19.3 \text{ torr} \end{aligned} \tag{6}$$

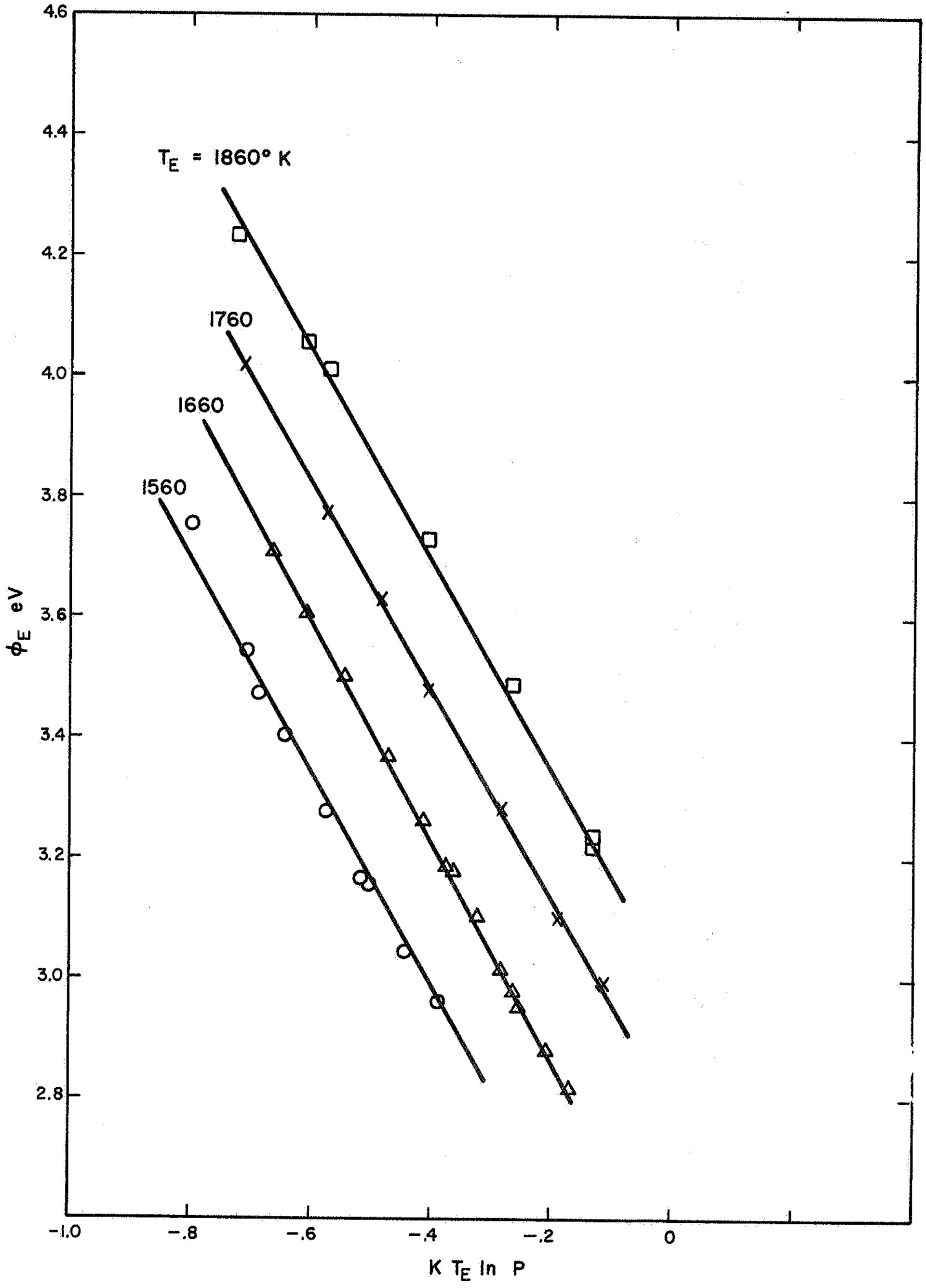
4.6
4.4
4.2
4.0
3.8
3.6
3.4
3.2
3.0
2.8
ϕ_E eV
T_E = 1860° K
1760
1660
1560
-1.0
-.8
-.6
-.4
-.2
0
K T_E ln P

Figure IV-25

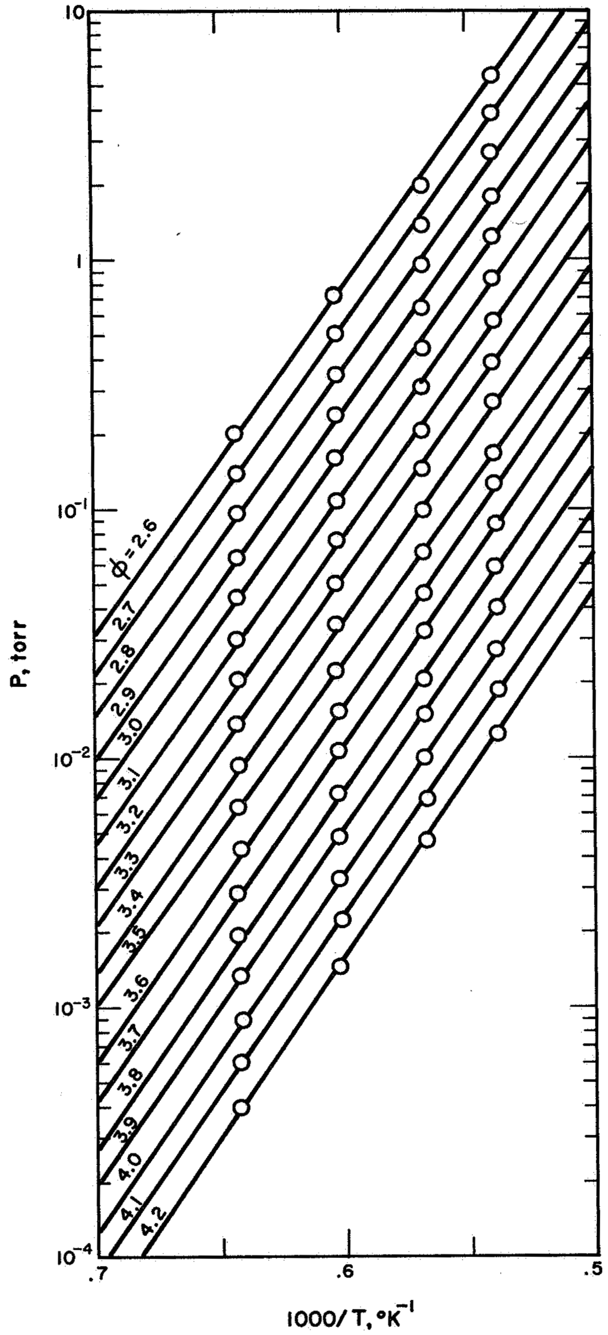
10
1
10^{-1}
10^{-2}
10^{-3}
10^{-4}
P, torr
ϕ=2.6
2.7
2.8
2.9
3.0
3.1
3.2
3.3
3.4
3.5
3.6
3.7
3.8
3.9
4.0
4.1
4.2
.7
.6
.5
1000/T, °K^{-1}

Figure IV-26

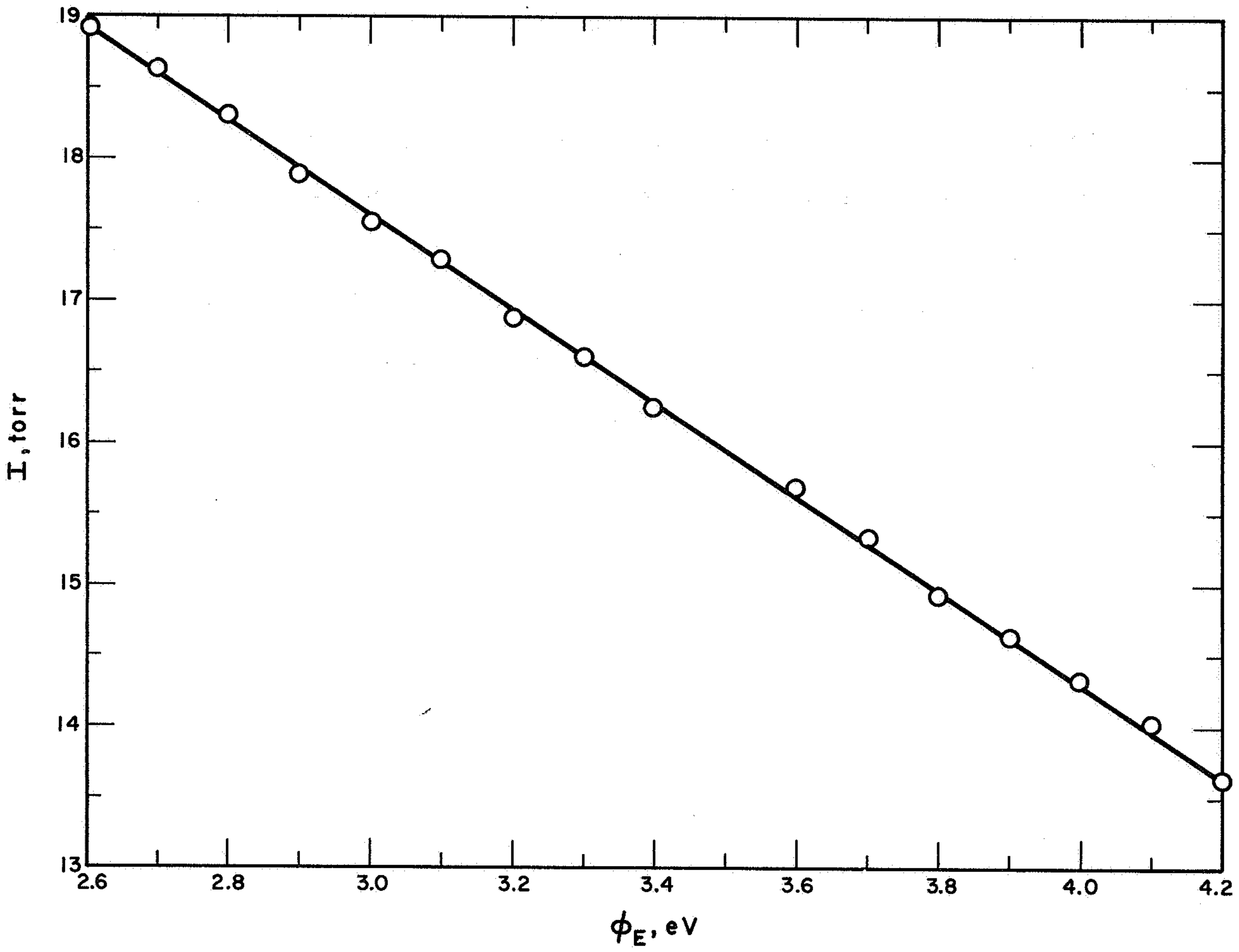

Figure IV-27

The slope S is determined from the constant-work-function lines in Figure IV-26 and is plotted as a function of ϕ in Figure IV-28. The constants α_2 and β_2 are determined from a least-squares fit to the data.

$$\begin{aligned} \alpha_2 &= 4.82 \times 10^3 \text{ torr, °K/eV} \\ \beta_2 &= 1.55 \times 10^4 \text{ torr, °K} \end{aligned} \qquad (7)$$

In order to evaluate this correlation, the experimental data was compared with the calculated values, using Equations 4, 6, and 7. Figure IV-29 shows that the experimental and calculated values are in agreement within 30 millivolts. The same data correlated by the T_E / T_R plots show a scatter of about 100 millivolts (Figure IV-30).

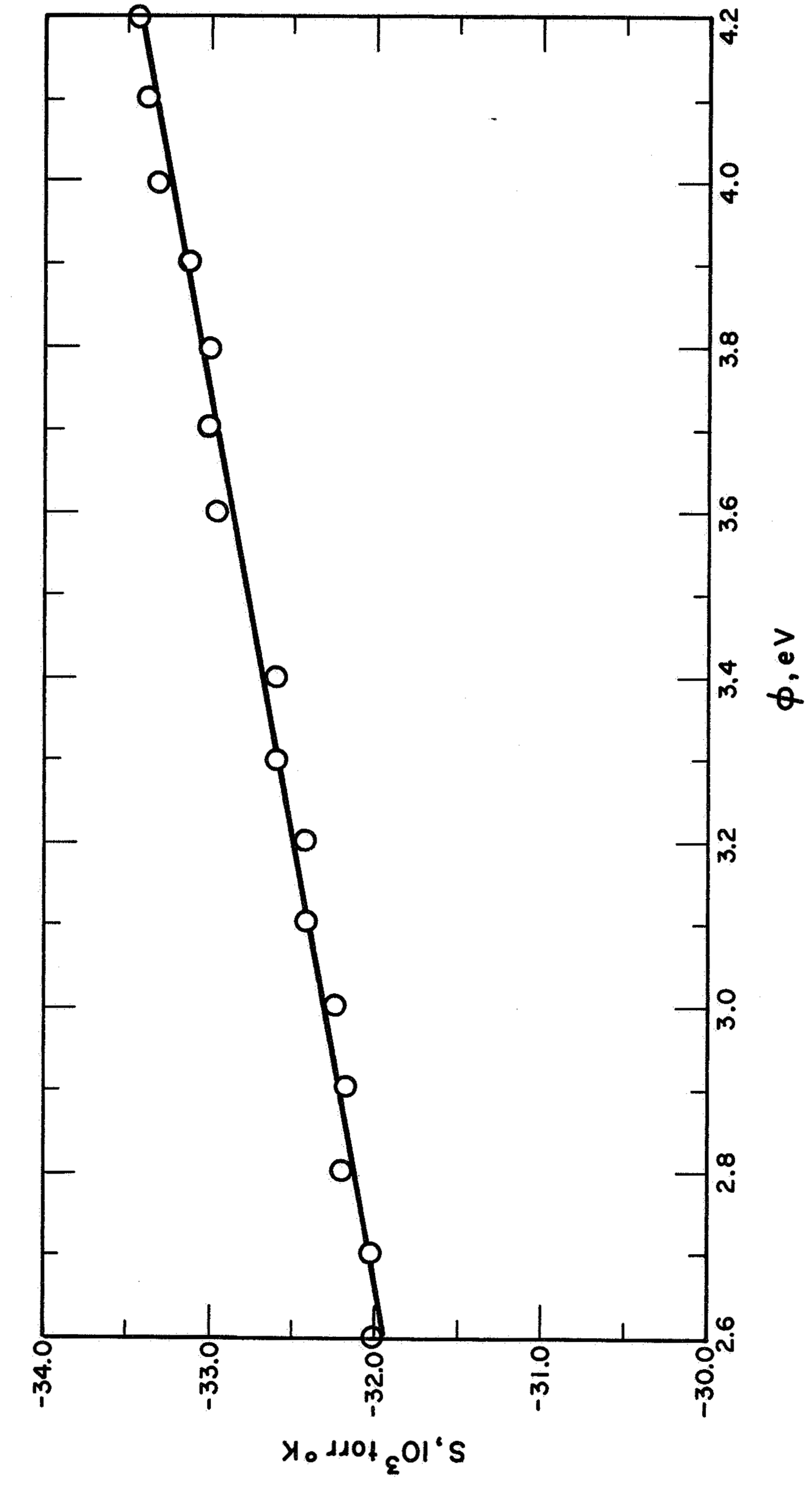

Figure IV-28

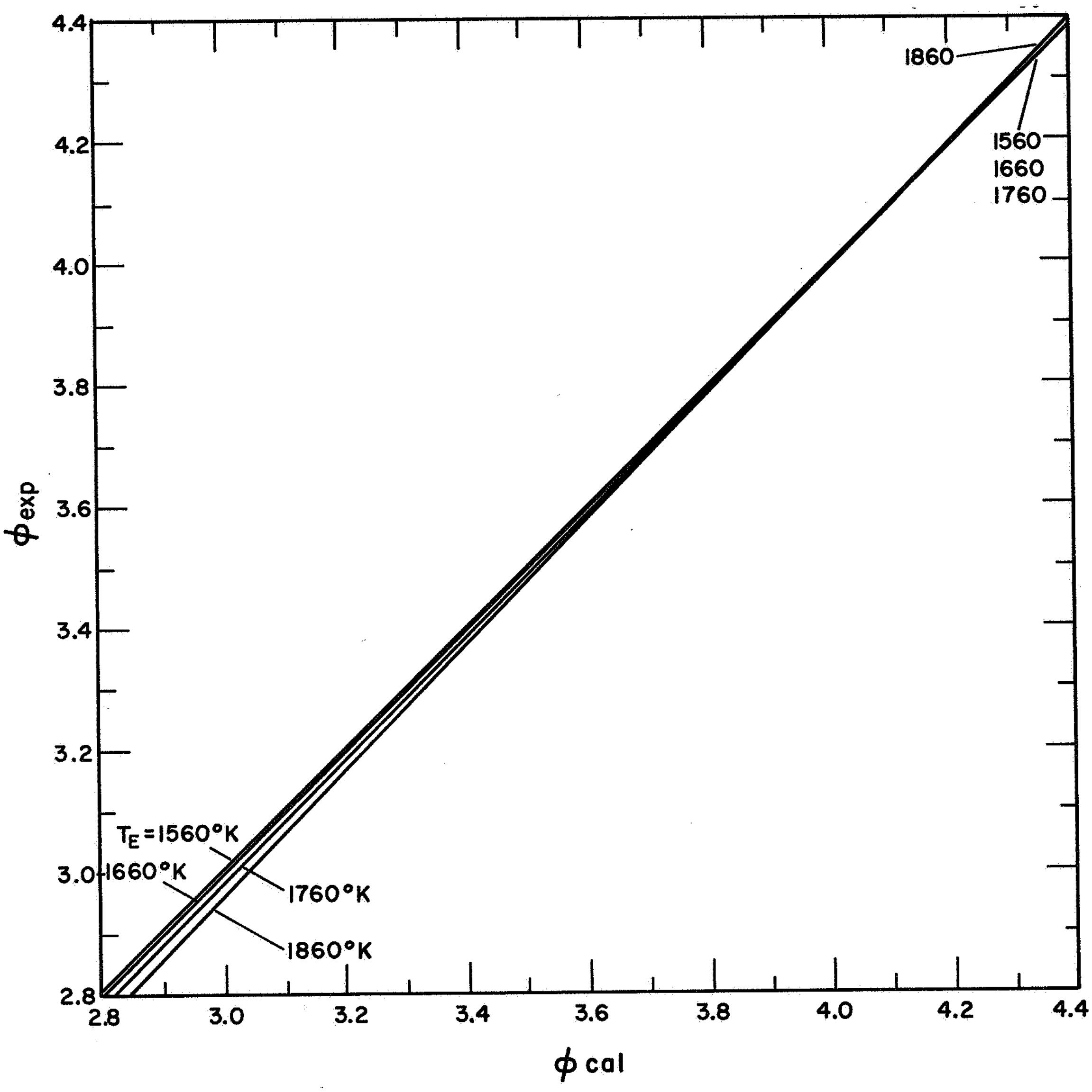
φexp
φ cal
4.4
4.2
4.0
3.8
3.6
3.4
3.2
3.0
2.8
2.8
3.0
3.2
3.4
3.6
3.8
4.0
4.2
4.4
1860
1560
1660
1760
T_E = 1560°K
1660°K
1760°K
1860°K

Figure IV-29

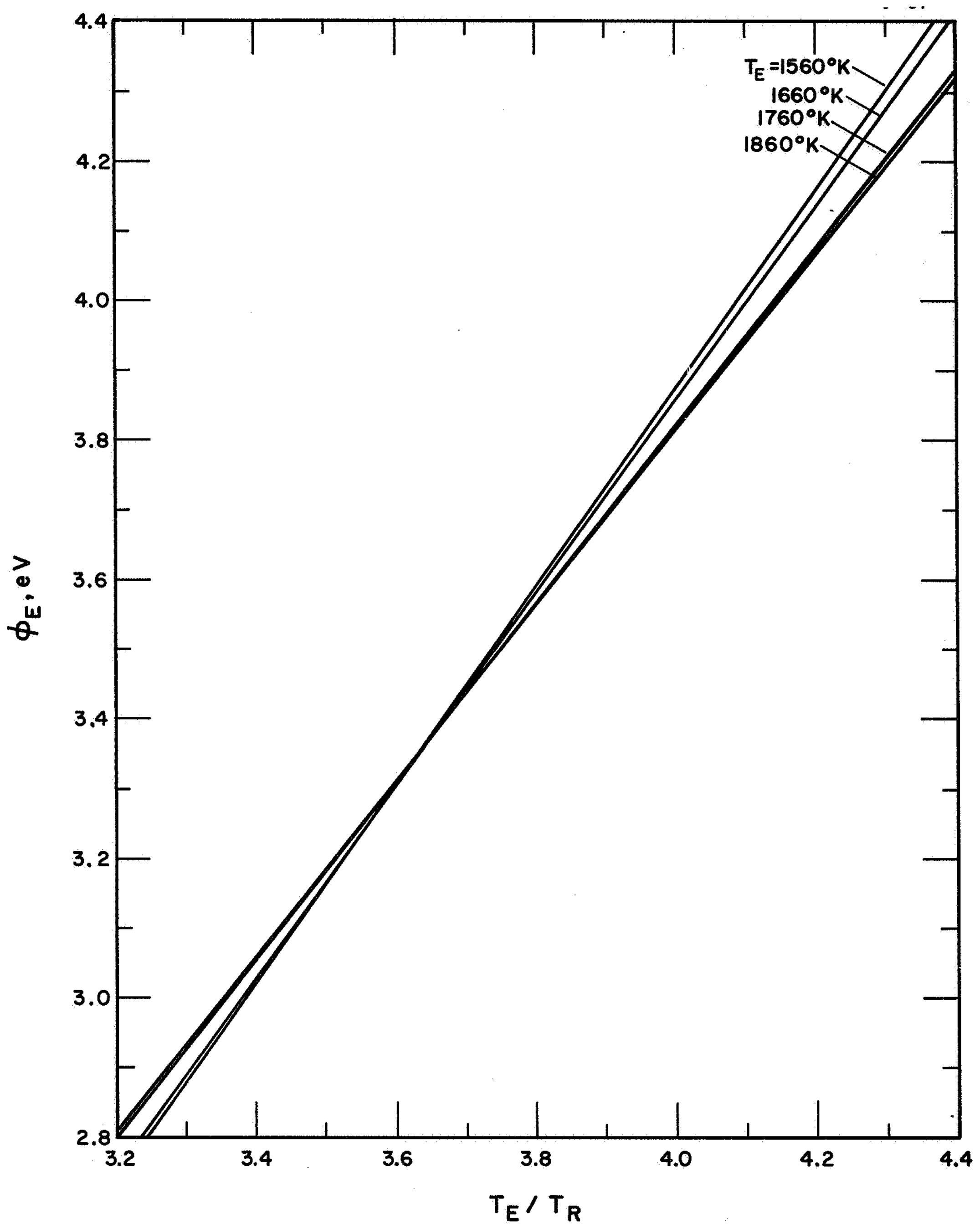
T_E =1560°K
1660°K
1760°K
1860°K
4.4
4.2
4.0
3.8
3.6
3.4
3.2
3.0
2.8
ϕ_E, eV
3.2
3.4
3.6
3.8
4.0
4.2
4.4
T_E / T_R

Figure IV-30

CHAPTER V

STUDIES ON VAPOR-DEPOSITED TUNGSTEN EMITTER MATERIALS

L. van Someren

During this quarter work has been carried out on the physical metallurgy of tungsten vapor-deposited from the fluoride and chloride compounds. This work is aimed at understanding the behavior of the bulk material under various mechanical and thermal treatments, as a necessary preliminary to attempting to modify the surface of the material to enhance its usefulness for thermionic emitters.

Material was supplied by San Fernando Laboratories, Inc., California, in the form of square tubes made by deposition onto one-inch-square molybdenum mandrels. A deposit about 0.2 inch thick was made, and then the mandrel was dissolved in an acid etch solution. After receipt at Thermo Electron, each tube was slit longitudinally at the corners to produce four strips of flat material about an inch wide. Discs were then cut from these strips by spark-machining. In some cases a flat was ground at the edge of the disc, and the flat, together with areas of the plane surfaces of the disc, was prepared for metallography by electropolishing in dilute sodium hydroxide solution and etching with alkaline ferricyanide solution. The uppermost surface of the deposit was ground flat in some but not all cases.

Chemical analyses of the material were not supplied by the manufacturer, but are under way at present.

A. FLUORIDE MATERIAL

1. As Received

The surface of the material next to the mandrel is a close replica of the mandrel surface. It bears visible traces of the grinding marks on the mandrel, but is quite smooth. The grain size is about 5 μ (40,000/mm^2). A longitudinal cross section of the deposit (Figure V-1) reveals well defined columnar grains several millimeters long growing from a thin layer of small equi-axed (randomly oriented) grains at the mandrel surface. The grain diameter increases with deposit thickness, as some grains grow in diameter at the expense of their neighbors. However, small new grains sometimes occur. The upper surface of the deposits (0.2 inch thick) is confused and rough on a scale large compared with the depth of focus of an optical microscope, so that it is not possible to photograph it. However, the grain size can be determined, if the material is lightly ground and then electropolished and etched. Figure V-2 shows a transverse section of the top surface prepared in this way, and reveals the wide range of grain sizes present. Excluding the smallest grains, the average size is about 70 μ (200/mm^2), implying a change in linear grain dimensions by a factor of 15 or so between the two surfaces of the deposit. It seems that the change occurs most rapidly at the start of the deposit. At the mid-plane the grain size is closer to that at the top than to that at the bottom.

The grains are unusually irregular, in comparison with material formed by more conventional methods. Grain boundaries are highly angular, when examined in both longitudinal and transverse sections. They do not show the tendency to form smooth curves meeting at triple points found in annealed material.

Figure V-3 shows a discontinuity in the grain structure near the mid-plane (just visible in Figure V-1). Total interruption of deposition usually results in the nucleation of a complete new set of grains when deposition is restarted: in the present case the grains

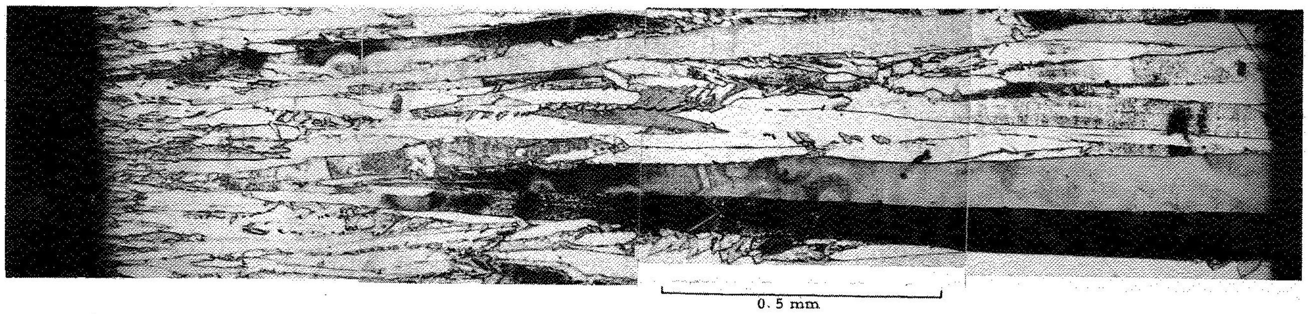

Figure V-1. Cross Section of Deposit from Tungsten Hexafluoride, as Received. WF.

(The scale for this figure applies to all other cross sections of this type.)

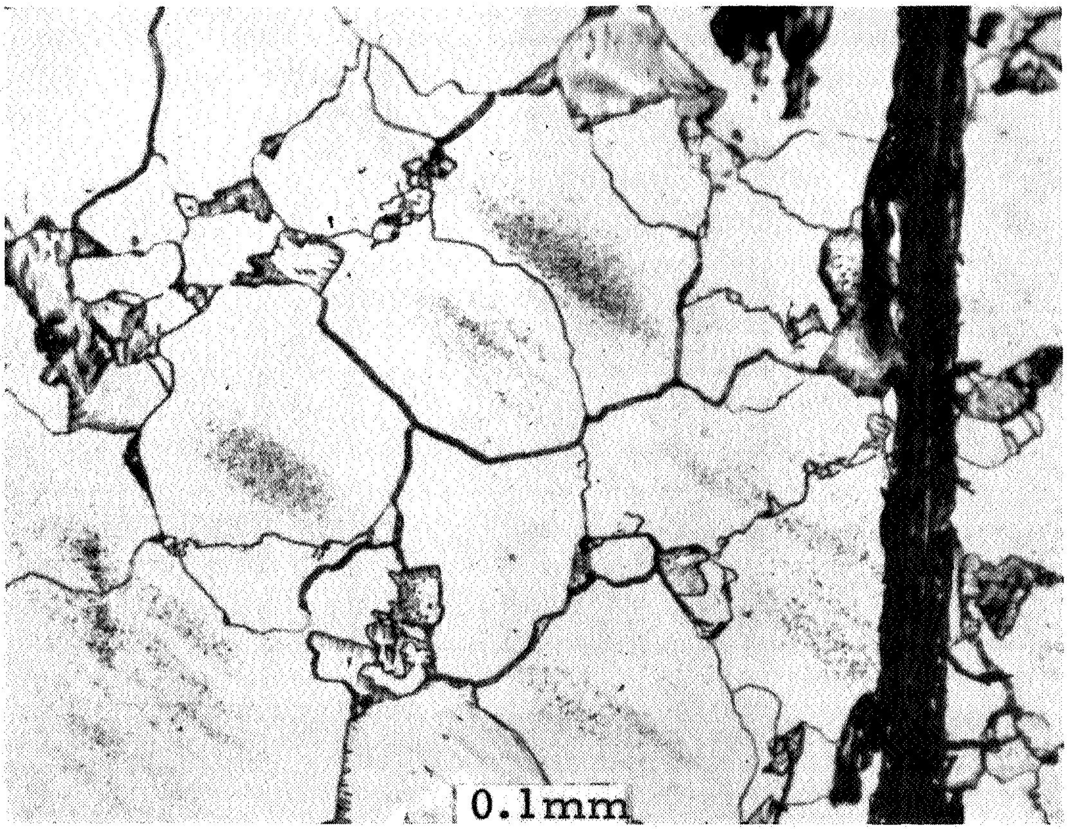

Figure V-2. Top Surface of Deposit Prepared to Show Grain Size. WF2A.

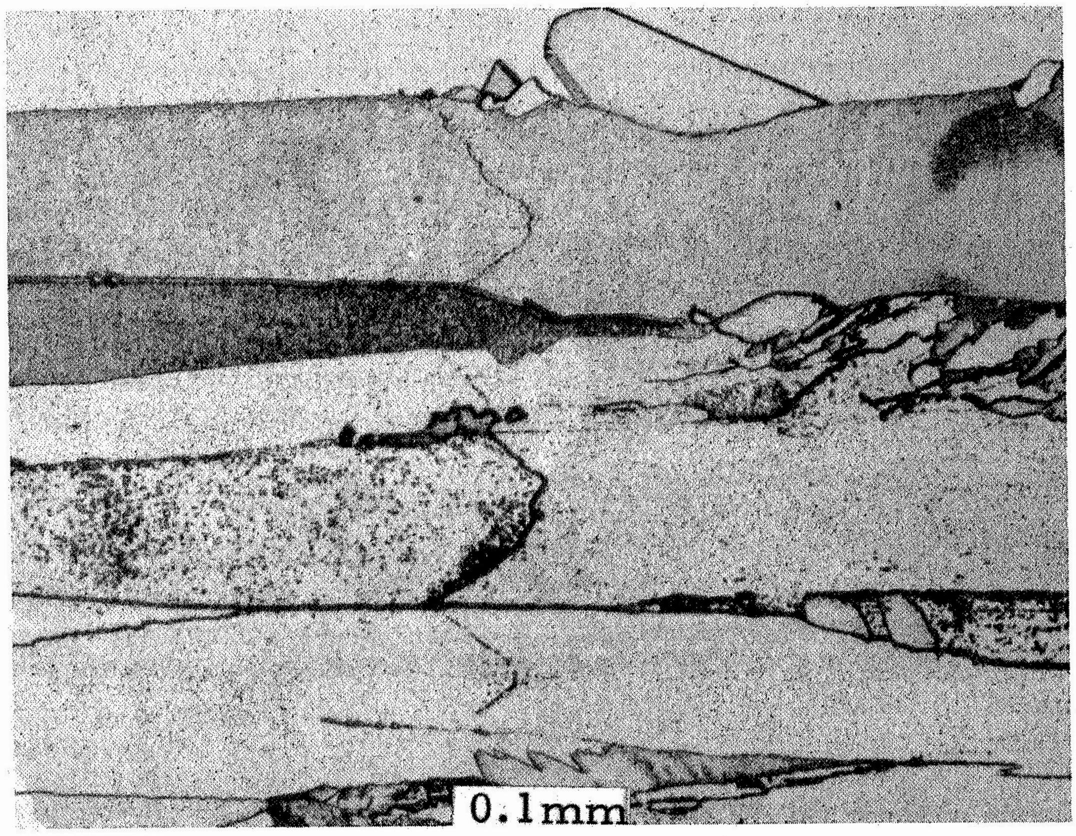

Figure V-3. Detail of Discontinuity in Middle of Deposit Thickness. WF.

continue across the interruption, so this discontinuity may have been caused by a minor perturbation in the environment during growth.

The material was quite brittle in tension (for example, under a hammer blow), but no samples have been broken by a drop from the bench to the floor. Preferred-orientation studies are described below.

2. Heat Treatment

Various specimens were heated by electron bombardment in a cold-walled furnace evacuated by a Vac-Ion pump to a pressure in the range of 10^{-5} to 10^{-7} torr. This technique is well established, and it has been shown that no contamination of the specimen occurs. Specimen temperatures were measured with an optical pyrometer sighted on the surface; a correction was applied to the observed reading, assuming the specimen emissivity was 0.4.

Composite photographs of the cross section of specimen WF2 before and after heat treatment are shown in Figures V-4 to V-7. These photographs show (4) the initial appearance, and the appearance of the same surface after exposure to (5) 6 hours at 2000°C and (6) 1 hour at 2400°C, and (7) the appearance after repolishing and etching the latter surface. Figure V-4 is very similar to Figure V-1, and together they indicate the variation in initial microstructure between samples. Figure V-5 shows the coalescence of some groups of small irregular grains, and the lessening of contrast between grains as the etched surfaces became smoothed by heat treatment. Signs of new grain boundaries are visible to the bottom of the deposit (near the reference

68-R-4-10

Figure V-4. Cross Section, as Received. WF2A.

68-R-4-11

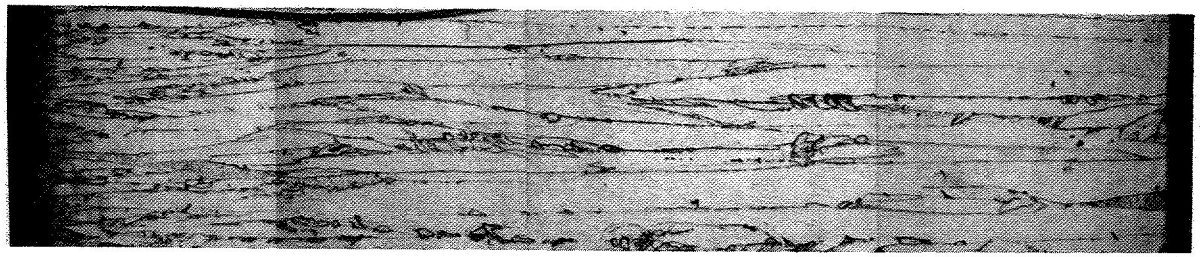

Figure V-5. Cross Section After 6 Hours at 2000°C. WF2B.

scratch). The more intensive heat treatment, 1 hour at 2400°C, prior to Figure V-6 produces further coalescence of grains, rounding of individual grains, and development of new boundaries near the bottom of the deposit. These are more clearly revealed in Figure V-7, which shows that the large number of columnar grains present within 0.2 mm of the bottom of the deposit has been replaced by a smaller number of non-columnar grains there. However, in the rest of the thickness of the material the grossly columnar structure is retained; while the irregular groups of grains have been lost, some angularities at boundaries have become smoothed, and some columnar grains have coalesced without loss of orientation. Figures V-8 and V-9 are of specimen WF2, and show the top of the deposit in the as-received condition and after the two heat treatments. The former, Figure V-8, shows the irregularity of grain outlines and the wide range of grain sizes, and the latter, Figure V-9, confirms the conclusions from sections of the material such as Figure V-7. The small grains have been absorbed by the larger ones, with only slight changes in the mean grain size, and some smoothing of the irregular boundaries of the large grains has occurred. The effect of a more intensive heat treatment, 6.5 hours at 2600°C, is shown in Figure V-10, a cross section after repolishing. Here one grain runs through almost the whole thickness of the specimen, except for a narrow (less than 0.5 mm) layer of grains at the top surface of the deposit. This sample had the top surface ground before this heat treatment.

The effect of milder heat treatments, such as might be used in preparing an emitter for operation, is shown in Figures V-11 and V-12 for specimens heated 20 minutes at 1900°C and 6 hours at 1800°C. The structure is changed relatively little from that found in the as-received material.

68-R-4-12

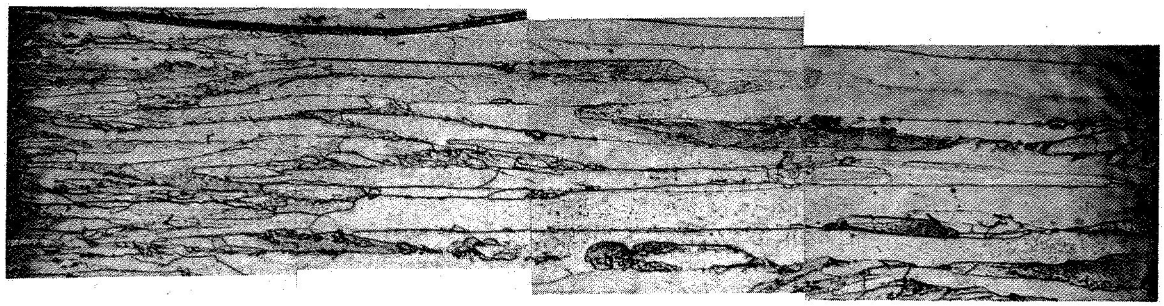

Figure V-6. Cross Section After 6 Hours at 2000°C and 1 Hour at 2400°C. WF2C.

68-R-4-13

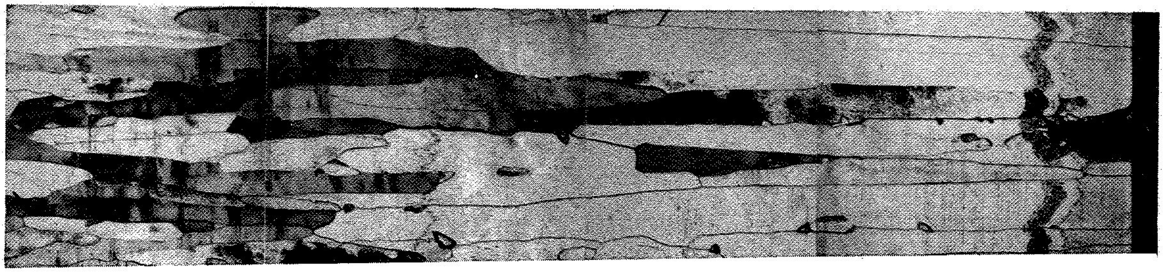

Figure V-7. Cross Section After 6 Hours at 2000°C and 1 Hour at 2400°C, Repolished and Etched. WF2C.

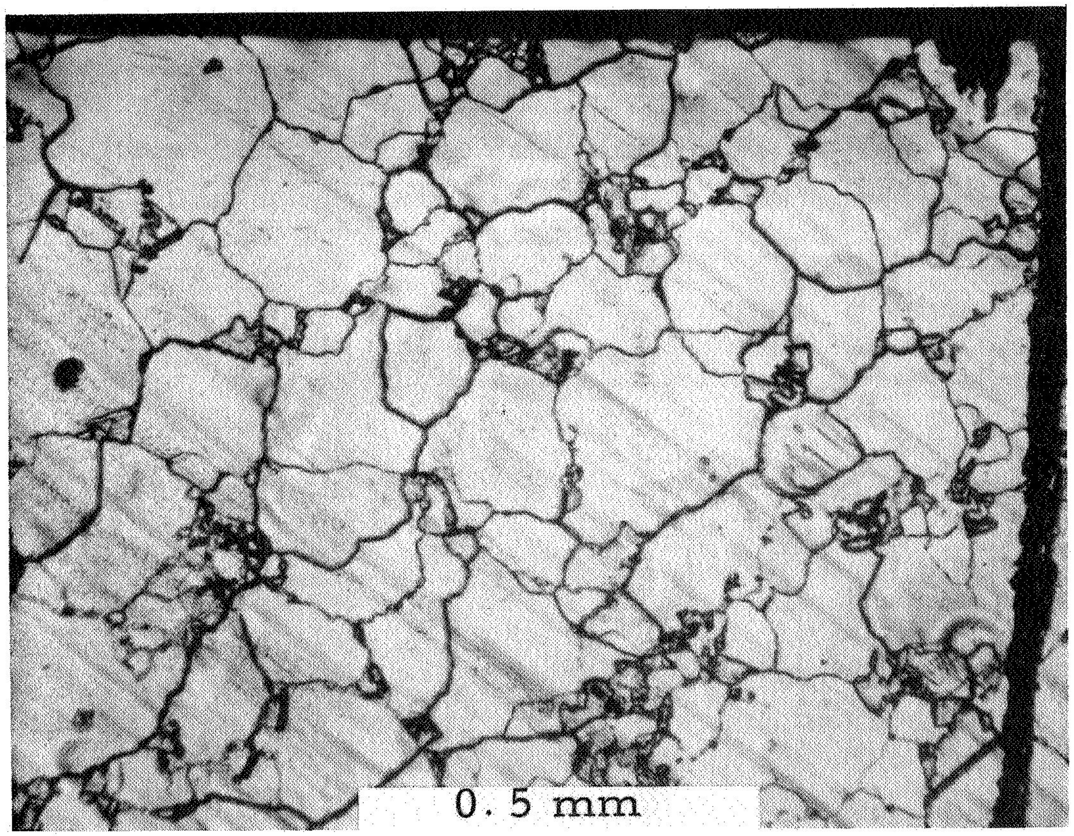

Figure V-8. Top of Deposit as Received, Ground, Polished, and Etched. WF2.

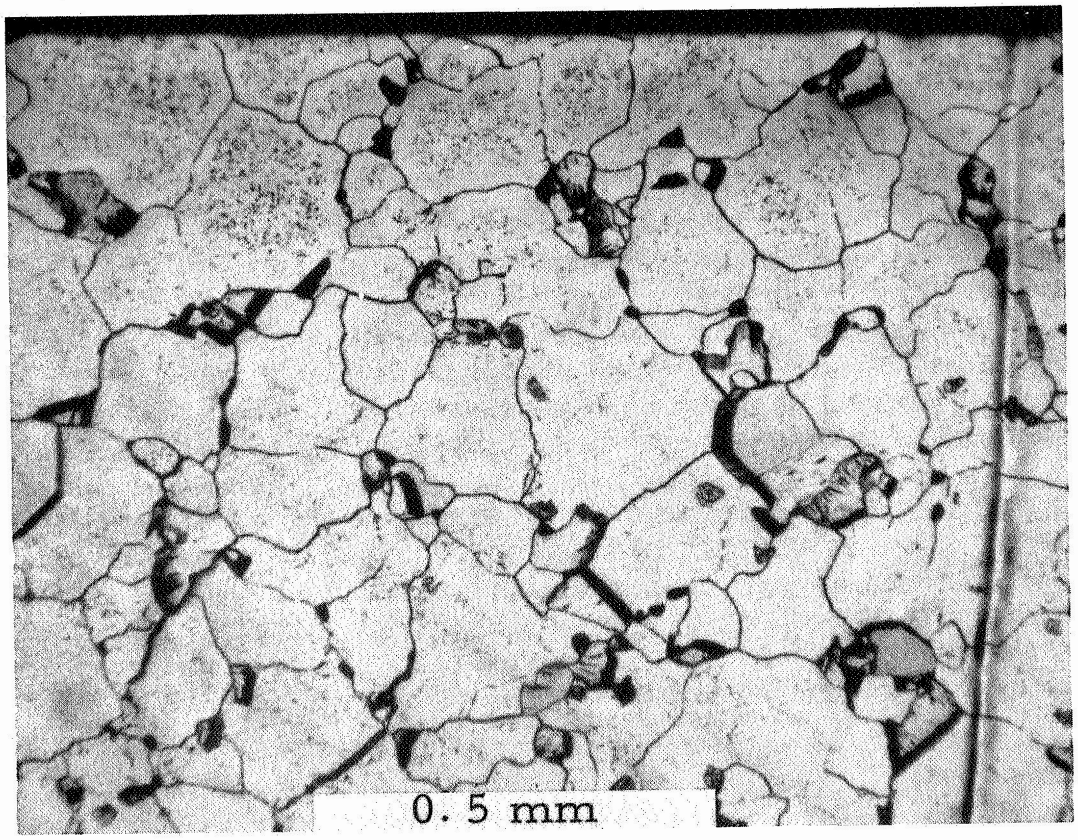

Figure V-9. Top of Deposit, After 6 Hours at 2000°C and 1 Hour at 2400°C, Repolished and Etched. WF2C.

68-R-4-16

Figure V-10. Cross Section After 6.5 Hours at 2600°C, Repolished and Etched. WF7C'.

68-R-4-17

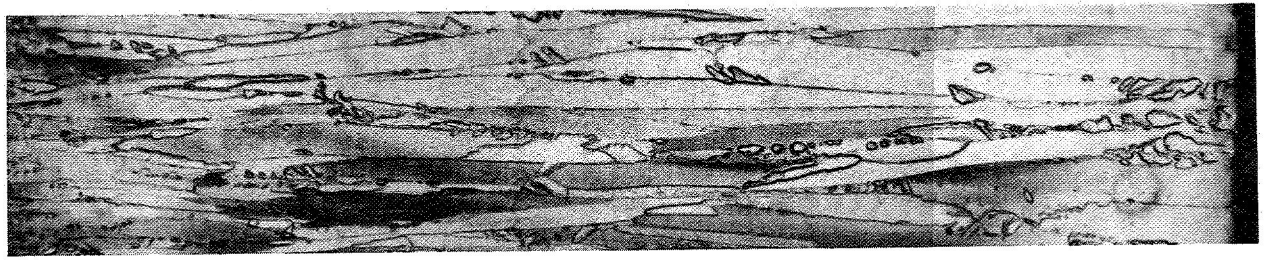

Figure V-11. Cross Section After 20 Minutes at 1900°C, Repolished and Etched. WF5.

Figure V-12. Cross Section After 6 Hours at 1800°C, Polished and Etched. WF4.

3. Conclusions

The fluoride material has a grain structure which is stable under relatively severe heat treatment. The first changes which occur are in the grains near the bottom of the deposit, which lose their columnar structure and form larger equi-axed grains. The columnar structure is retained even after 1 hour at 2400°C, though some coarsening of the columnar grain size is observed then. This columnar structure is completely lost after 6.5 hours at 2600°C.

B. CHLORIDE MATERIAL

1. As Received

This material is deposited at a higher temperature than the fluoride material, and because of technical problems associated with this temperature, two shorter square tubes were supplied in place of the single long tube of fluoride material. The deposit surface appears slightly smoother to the eye and to the touch than does that of fluoride material.

Cross sections revealed gross differences between the two techniques. While the fluoride deposits contained some grains running through the whole thickness of the deposit, the chloride material was composed of layers varying in thickness and grain size. In each deposit, nominally 0.2 inch thick, there were 11 distinguishable discontinuities, varying from gross porosity (#9) or layers of foreign material (#2) to simple renucleations of the deposit (#10 and #11) or mere lines (#7). Cross sections of each of the two ingots are shown in Figures V-13 and V-14 with the discontinuities numbered. Though the ingots were made and shipped at different times, there are similar types of discontinuities at similar positions in the deposits.

In the course of preparing samples for metallography the following curious observation was made: a specimen was electropolished (5% NaOH, 10 volts), and when the cross section was rinsed and pressed on a paper towel to dry it, a liquid with a distinct blue color oozed from #9 in the middle of the deposit and left marks on the towel. Under the microscope more liquid could be seen oozing from the pores near the middle of the deposit, and in fact it proved difficult to eliminate this effect.

About two-thirds of the way up through the deposit No. 2 (Figure V-14) is a region between #8 and #9 showing a continuous grain structure with layers of varying etch response. Detailed examination revealed several of these striated regions, in some cases associated with porosity (Figure V-15) and in some cases not (Figure V-16). This appearance resembles that reported for Federite, a non-equilibrium structure found in W-Re alloys made by vapor deposition.

The first layer of conspicuous material in the deposit, #2, is found about 0.7 mm from the bottom of the deposit, and is clear in Figures V-13 and V-14. A detail of this zone in ingot 2 after electropolishing (without etching) is shown in Figure V-17. Reference to Figure V-14 shows that the grain structure is continuous across this layer. The sharp contrast in electropolishing behavior strongly suggests that it is not pure tungsten. However, continued polishing removes the material (Figure V-17a).

2. Heat Treatment

Specimens from ingot 1WC of chloride material were heat-treated in exactly the same way as the fluoride specimens discussed above. Two differences were noticed. During the first stages of heating the specimen from room temperature to red heat considerable outgassing occurred,

68-R-4-18

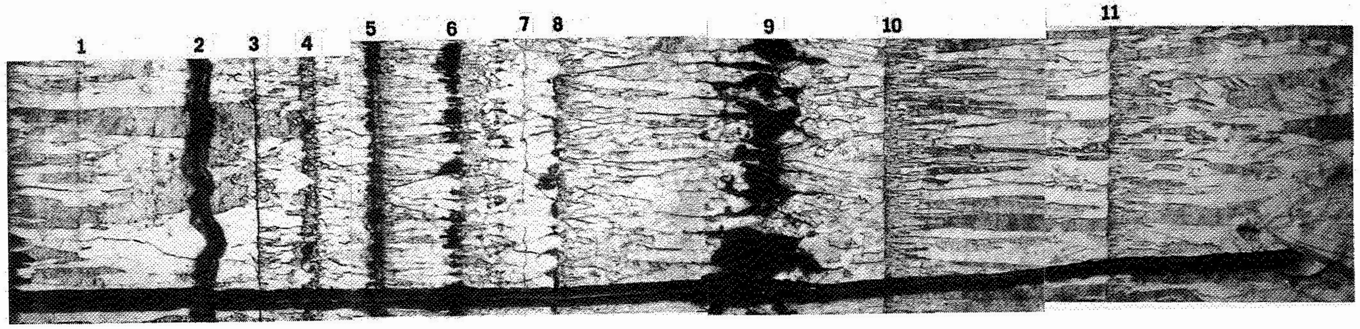

Figure V-13. Cross Section of Deposit from Tungsten Chloride, as Received. 1WC.

68-R-4-19

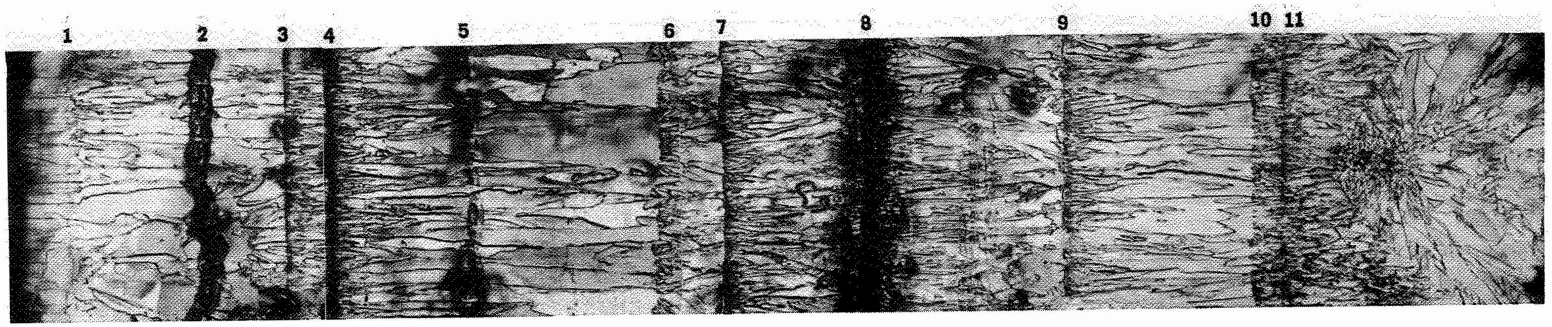

Figure V-14. Cross Section of Deposit from Tungsten Chloride, as Received. 2WC.

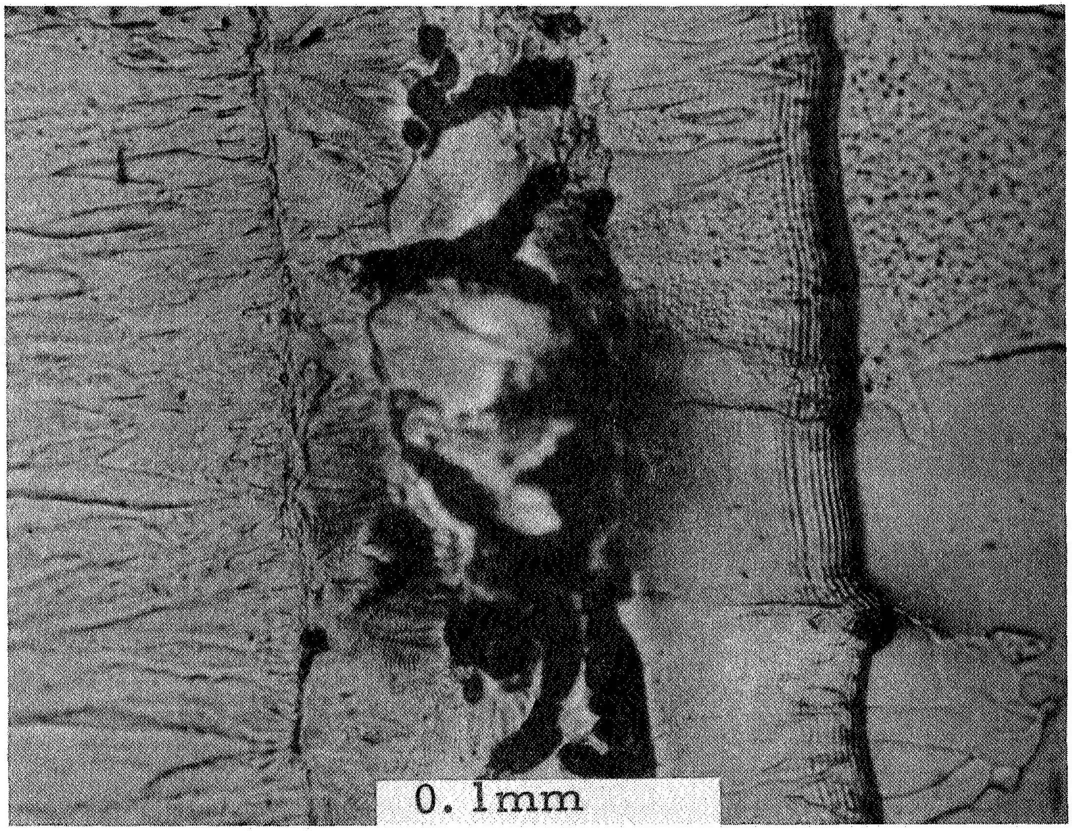

Figure V-15. Detail of Striated Zones Near Porosity in Ingot. 2WC.

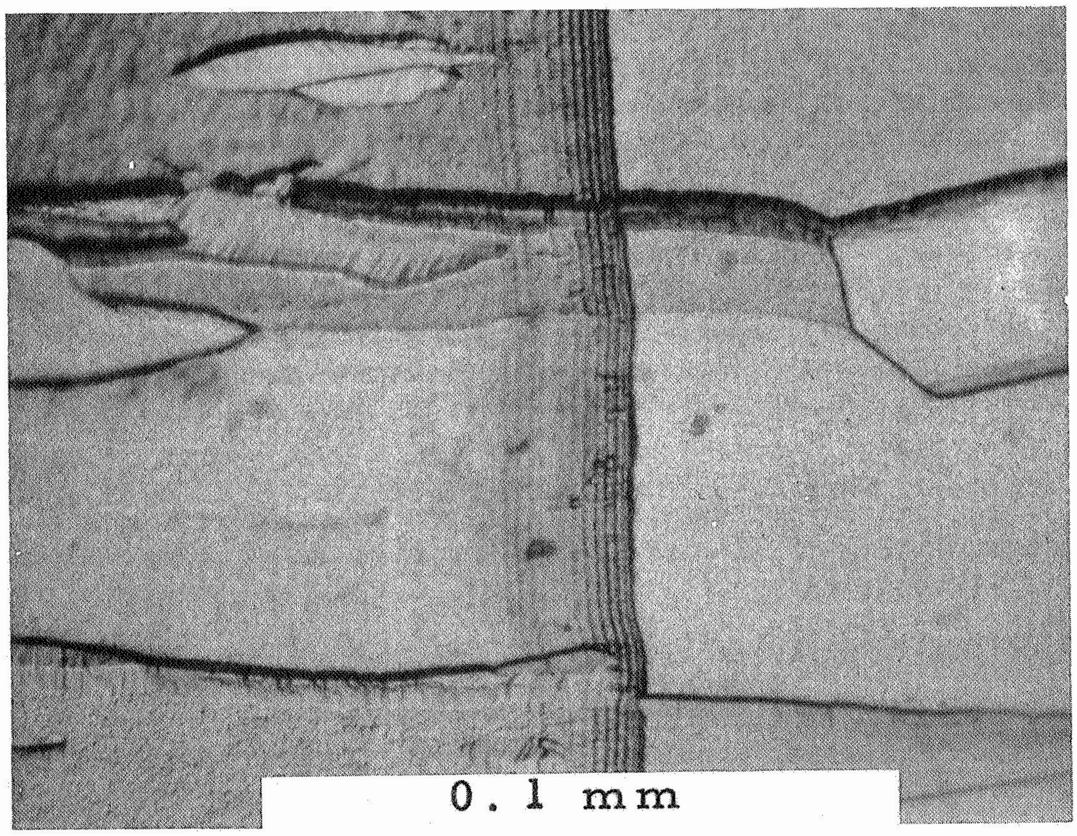

Figure V-16. Detail of Striated Zones without Porosity in Ingot 2WC.

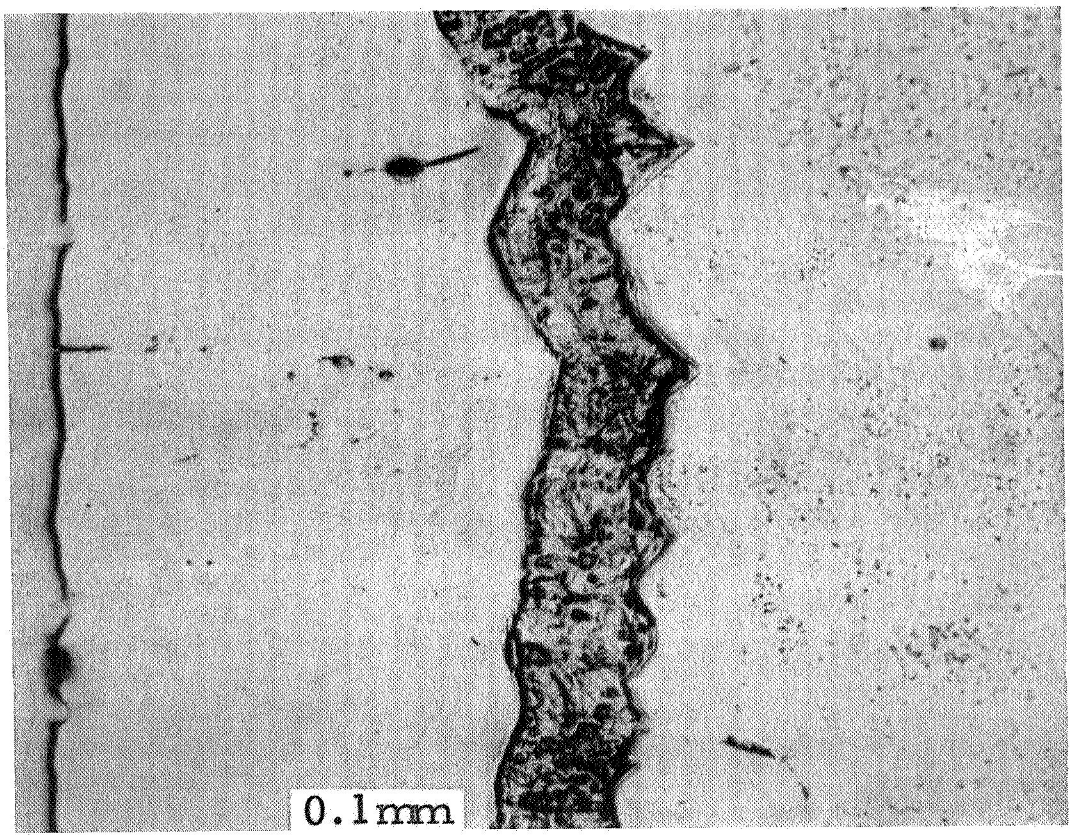

Figure V-17. First Foreign Layer, #2, Electropolished Only. 2WC.

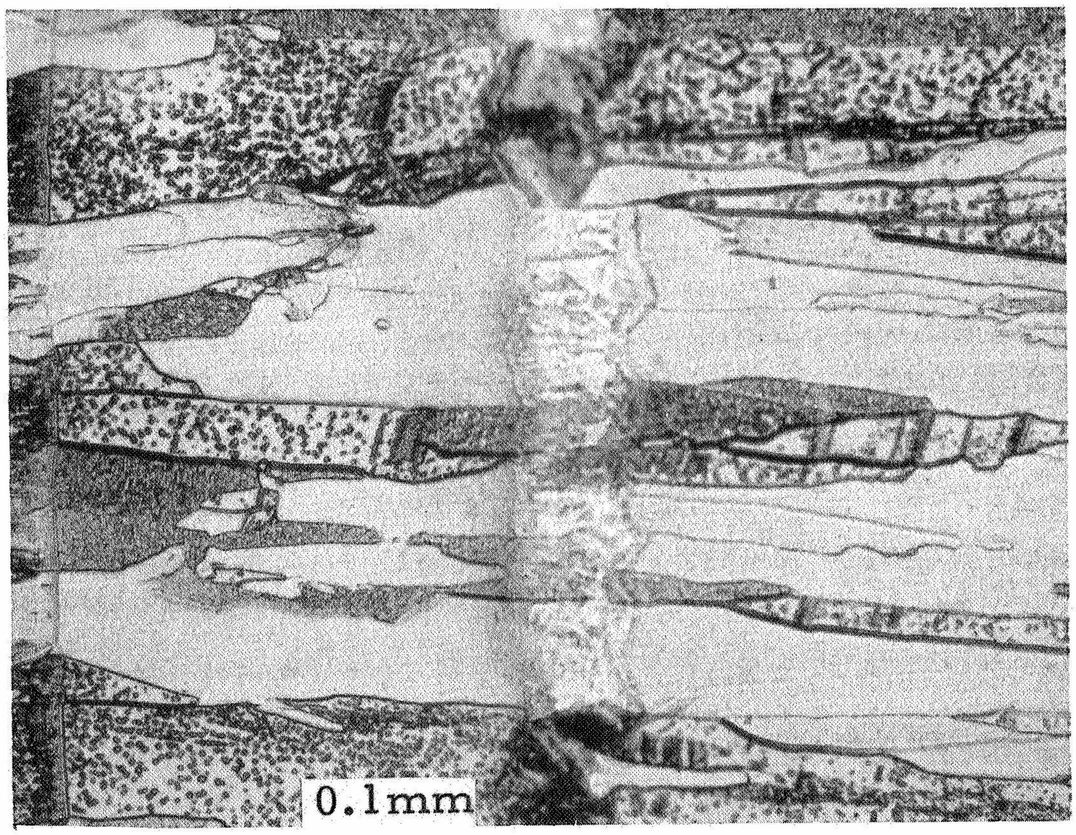

Figure V-17a. Same Region After Prolonged Electropolishing.

and this limited the rate at which the temperature could be raised. Furthermore, during one run in which the specimen attained 2230°C, considerable evaporation occurred from the specimen while at temperature, and condensation on the bell jar seriously interfered with temperature measurement. Such evaporation did not occur when the specimen was at 2100°C, and does not occur from pure tungsten at 2230°C.

Specimens which were heat-treated showed progressive changes in the microstructure as follows:

After 6 hours at 1800°C considerable recrystallization has occurred; in some regions, Figure V-18, such as 0 to #2 and #10 to #11, the columnar structure is retained, while in others, such as #11 to the top surface and around #9, the grains adopt a more nearly equi-axed arrangement. While greater changes occur in the wider zones, the converse is not always true. Zones #4 to #5 and #5 to #6 are of nearly equal width, but show unequal changes in structure after this heat treatment.

Treatment for an hour at 2100°C developed the structure shown in Figure V-19, in which considerable further coarsening has occurred in some layers, #9 to #10, while others, such as #5 to #6, have changed little. The striations around #7 are seen in Figure V-20 to be bands of etch pits, rather than the layered appearance of Figures V-15 and V-16.

The corresponding views of the prepared surface of the top of the deposit are given in Figures V-21 to V-23, and show the striking loss of angularity of the grains during the mildest heat treatment, together with an increase in grain size.

68-R-4-23

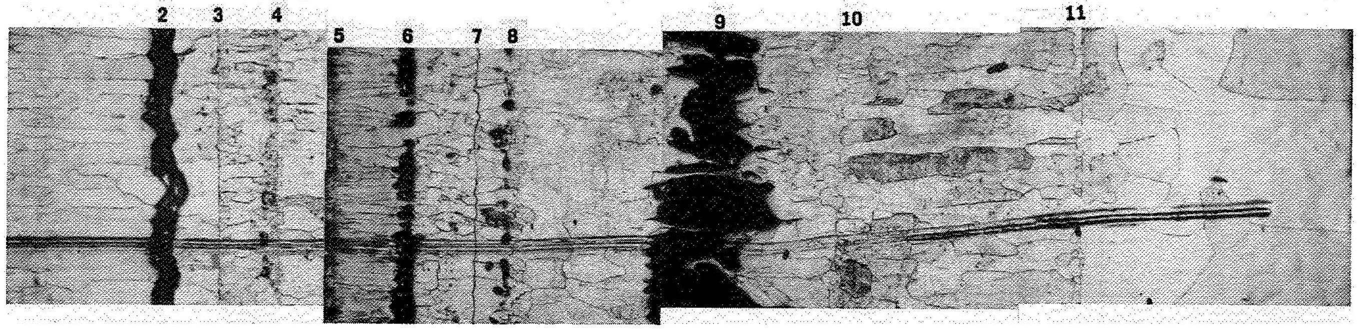

Figure V-18. Cross Section After 6 Hours at 1800°C, Repolished and Etched. WC2B'.

68-R 4-24

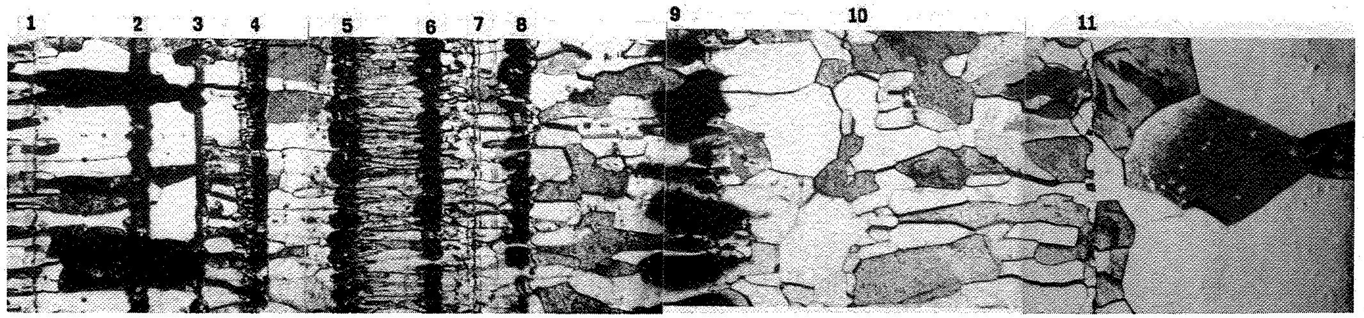

Figure V-19. Cross Section After 1 Hour at 2100°C, Repolished and Etched. WC3B'.

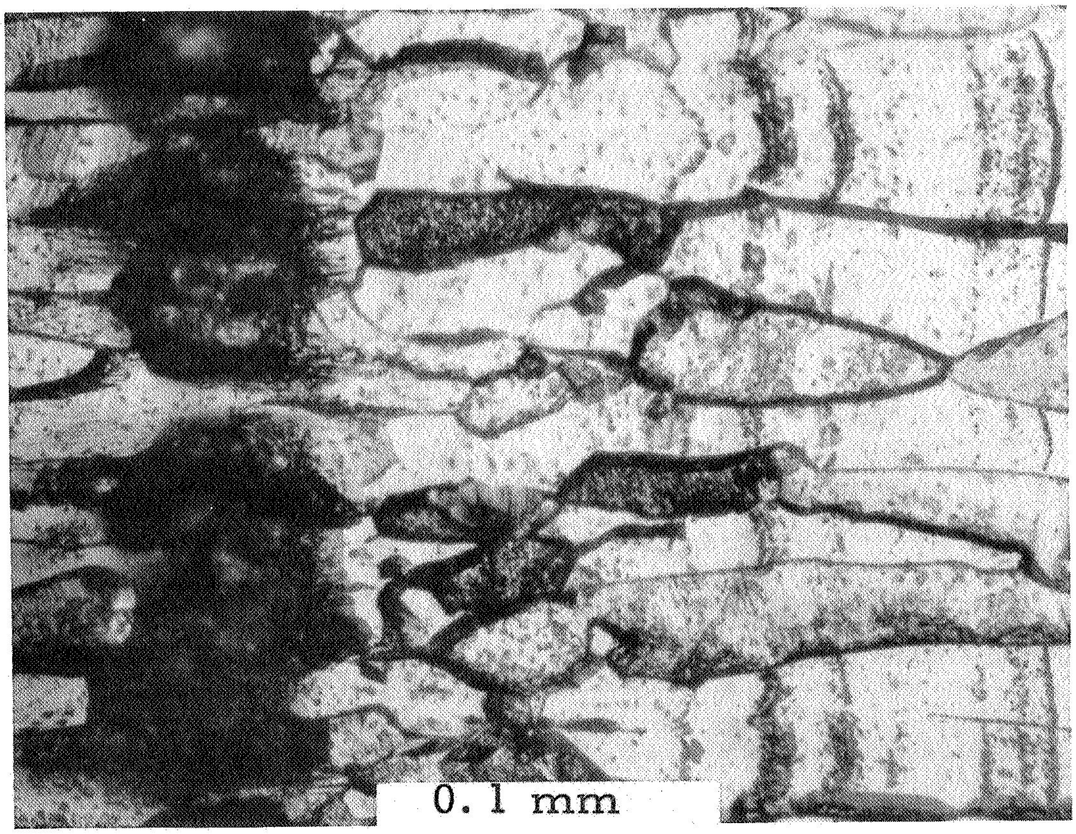

Figure V-20. Detail Near #7 from Figure V-19.

68-R-4-26

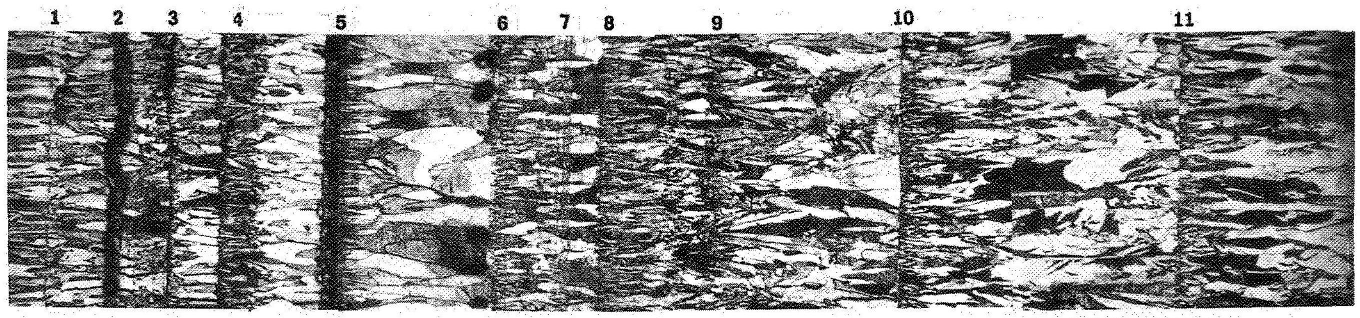

Figure V-21. Ground and Polished Top Surface of **As-Received** Sample. WC2A.

68-R-4-27

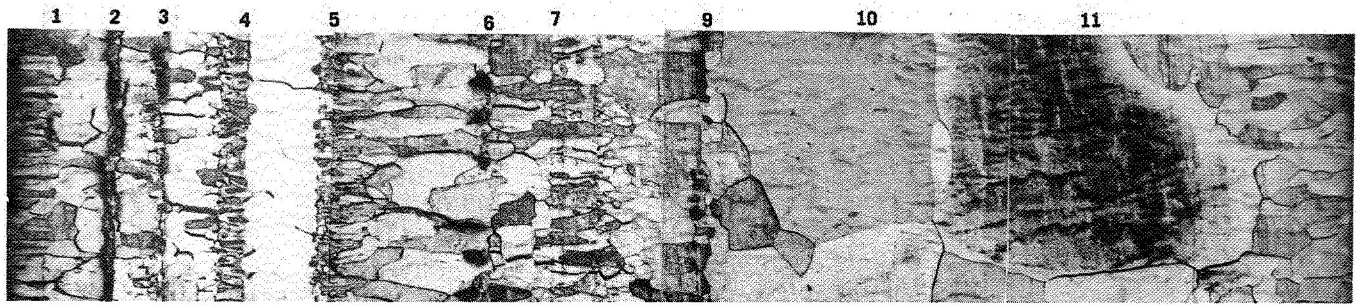

Figure V-22. Ground and Polished Top Surface of Sample After 6 Hours at 1800°C. WC2B′.

68-R-4-28

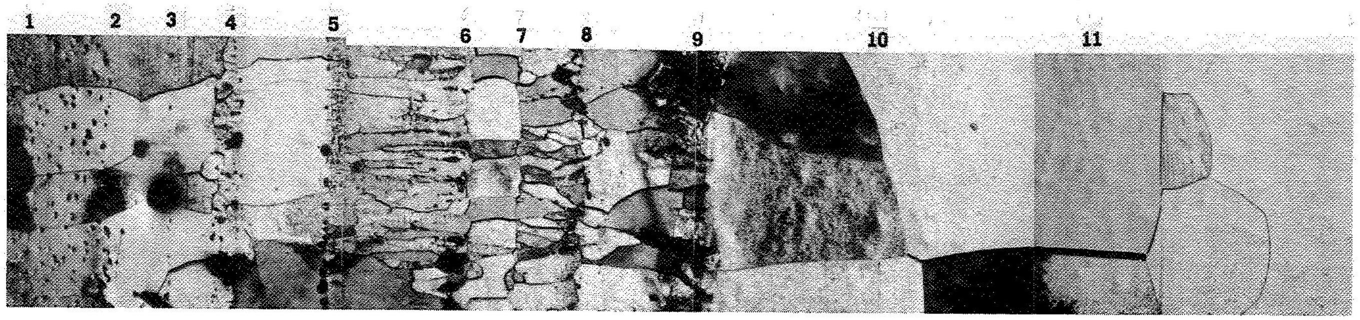

Figure V-23. Ground and Polished Top Surface of Sample After 1 Hour at 2100°C. WC3B′.

Figure V-25 shows the effect of exposure to 1 hour at 2230°C on the sample whose prior appearance is shown in Figure V-24. The layers seen here correspond to those in Figure V-13, though they differ in thickness.

Coarsening of the grain size has occurred to an extent which varies erratically between layers. The largest grain size is now found between #9 and #11, but, in contrast to Figure V-19, this coarse structure does not extend to the surface of the deposit. However, in Figure V-26 we see that more intensive treatment (1 hour at 2370°C) produces a large grain size from #9 to the surface. This also eliminates the layer of material at #2 and produces porosity there and at other interfaces.

3. Conclusions and Discussion

0.2-inch chloride material is deposited in many layers of varying thickness, grain size, and homogeneity. Heat treatment produces changes which vary unsystematically from layer to layer (though for the samples examined the response is uniform within each layer). Changes occur in conditions too mild to produce changes in fluoride material – e.g., 6 hours at 1800°C.

Variations in fluorine content are known to affect the grain growth of fluoride tungsten. Variations in the content of some impurity in different layers of this material may account for the varying response to heat treatment.

C. POLE FIGURE DETERMINATION BY X-RAY DIFFRACTION

Following the work of Doctor Ling Yang of Gulf General Atomic, studies of the preferred orientation of fluoride and chloride samples

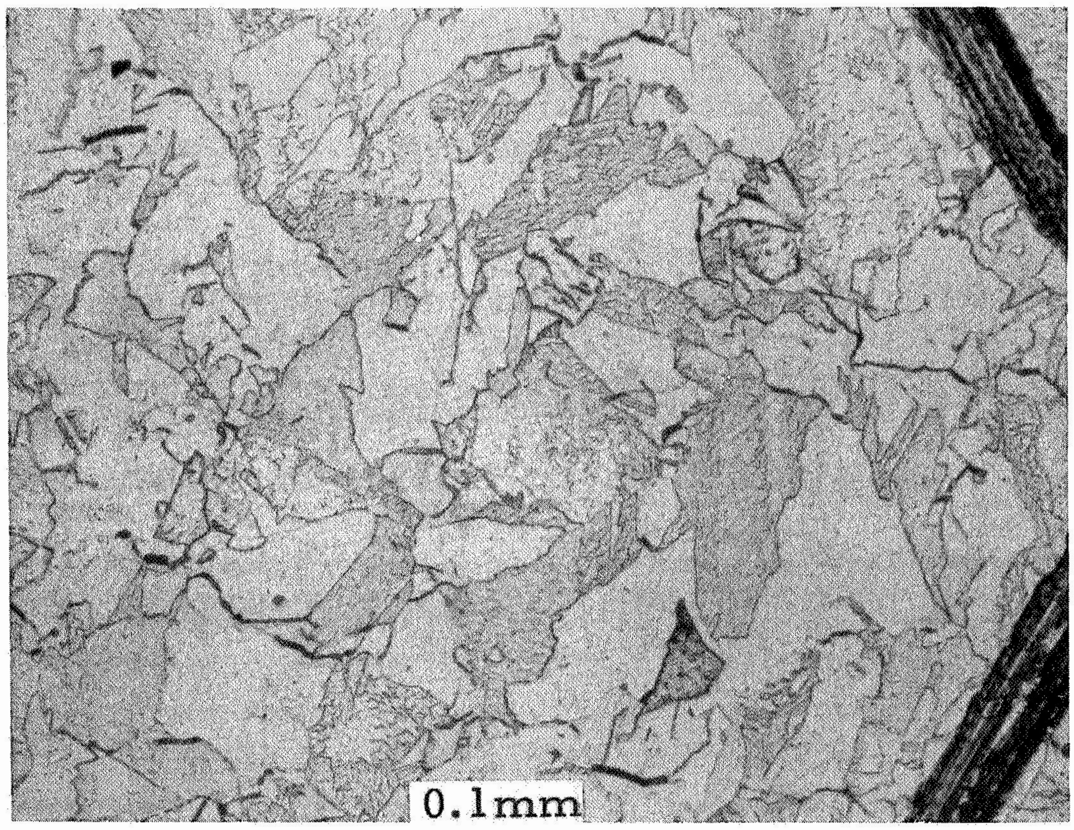

Figure V-24. Cross Section as Received, Polished and Etched. WC4A.

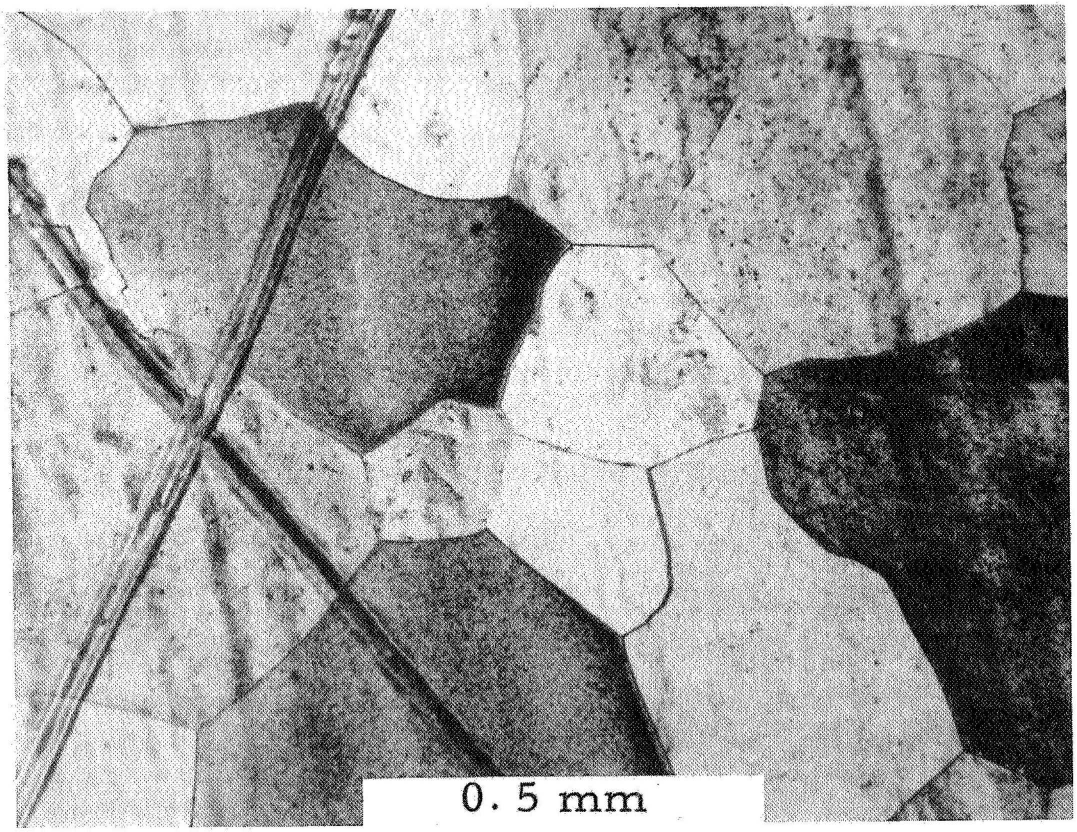

Figure V-25. Cross Section After 1 Hour at 2230°C, Polished and Etched. WC4B′.

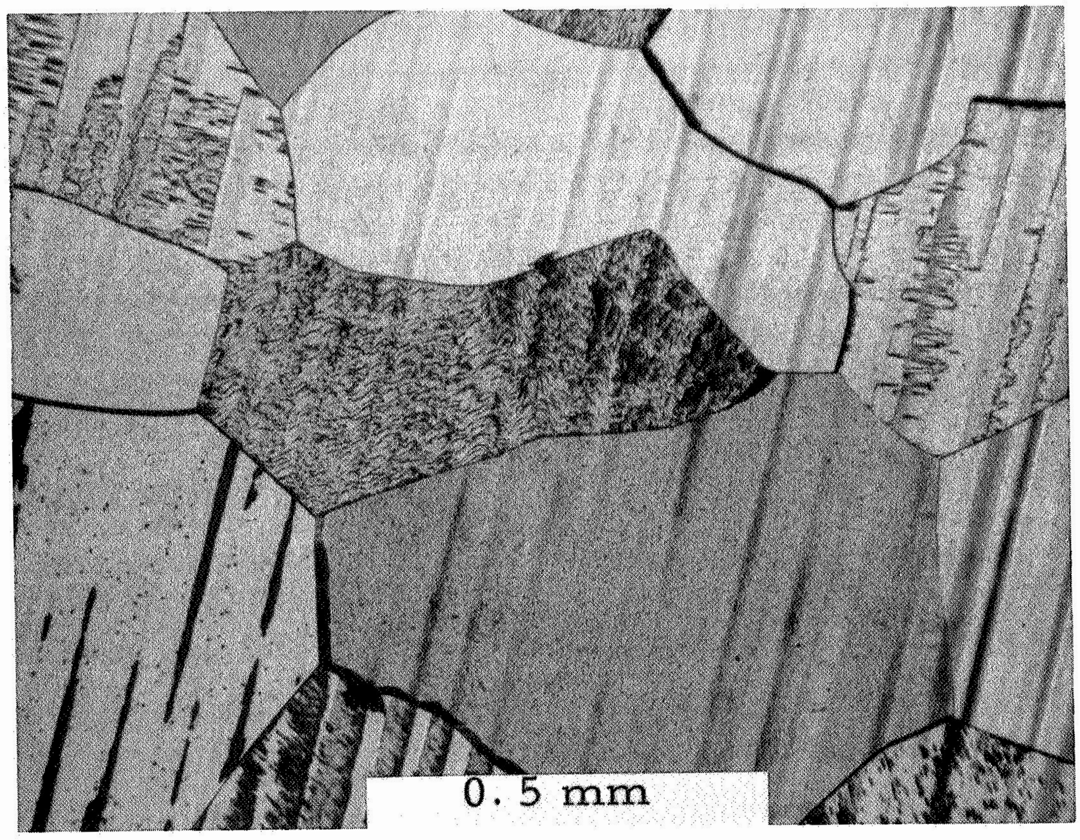

Figure V-26. Cross Section After 1 Hour at 2370°C, Polished and Etched. WC0B′.

have been made. A standard Norelco Pole Figure accessory is used in a simplified mode. The specimen is set with its surface on the diffractometer axis, and its surface normal bisecting the incident and diffracted beams, while the angle between the latter is chosen to fulfill the Bragg condition only for the type of crystal plane which is expected to occur parallel to the surface (e. g., $2\theta \sim 40°$ for deposits from the chloride having (110) planes parallel to the surface for the radiation used here). Then the surface normal is rotated out of the plane defined by the x-ray beams through an angle α, and the intensity of the desired reflection is recorded as a function of α. A normalized cumulative integral of the I-versus-α curve is derived algebraically and identified with the distribution curve showing the fraction of the specimen having the chosen planes with angle α of the surface normal. This curve runs from 0 at $\alpha = 0$ to 1 at some α between 10° and 30°. Its convexity upwards is a measure of the preferred orientation in the sample. The raw data from a well oriented sample takes the form of a symmetrical smooth curve rising from $\alpha = -20$ to a peak at $\alpha = 0$ and dropping to $\alpha = +20$.

The beam width is about 2 mm. Sampling of a number of grains is obtained by oscillating the specimen along a line in its own plane perpendicular to the incident beam, through an amplitude of 1. 5 cm. The period of the sampling oscillation is kept small compared to the time constant of the recording circuit, in order to reduce oscillations in the recorded signal due to any single strongly-reflecting grain.

Laue back reflection photographs of the material consist of uniform rings, indicating that the material is isotropic in that there is no preferred orientation along certain directions in the deposit.

That is to say, there is no analog of the rolling direction or transverse direction found in rolled sheet. Consequently, the rotation of the sample about its own surface normal will not alter the x-ray data obtained from it.

Most measurements have been made without any slits between the specimen and the detector (scintillation counter) opening. This leads to a loss in angular resolution accompanied by a smoothing of the output data curve. Most measurements have been made over a range of α from -20° to +20°, and the average of two readings for α was processed to give the final data. Unfiltered Cu Kα radiation is used, from a tube operating at 35 kV and 15 mA.

1. Results

The results are best presented in the form of graphs showing the fraction of the x-ray intensity originating within an angle α of the symmetrical ($\alpha = 0$) position, as a function of α. Such graphs will be called pole figures. These can be interpreted as indicating the fraction of the grains present having the investigated crystal planes within an angle α of the surface. (The investigated plane is (110) for chloride samples and (100) for fluoride samples). Such curves are necessary to present the data, since a curve cannot in general be represented by a few simple parameters without making assumptions about its shape. However, it may sometimes be convenient to summarize the data from a curve by using numerical indices, such as angles necessary to include 50% and 90% of the intensity. These figures may be interpreted to mean that 50% of the grains have, say, (100) planes within the specified number of degrees of the surface. Any inference about the thermionic behavior of the surface must await empirical correlations between curve shape and material performance.

2. As-Received Material

The curve derived from data taken from the top surface of fluoride material in the as-received (unground) condition is shown in Figure V-27. This pole figure shows a strong preferred orientation, in that half the area is oriented within 1.7 degrees of the (100) planes. A random sample would give a straight line from 0° to 20°, with a 50% angle of 10°. Another piece of material was ground flat (on a conventional surface grinder) and then electropolished to remove material damaged by grinding. A pole figure was obtained after about 0.002 inch (50 microns) had been removed by polishing, and this is shown in Figure V-28. It indicates a preferred orientation almost equal to that of the as-received material. The reverse surface of the deposit, next to the mandrel, was examined briefly and found to give an intensity of (100) reflection invariant with α, implying that it had a random orientation. The penetration depth of x-rays into the sample is a few microns, comparable with the diameter of the grains found at the bottom of the deposit, and presumably only this thin non-columnar layer of material is contributing to the signal, and is shielding the better-oriented structure from the x-rays.

If the material is ground, sandblasted or abraded to produce mechanical damage, the damaged layer has a random or disordered structure, at least to a depth of a few microns, and it gives a straight-line pole figure characteristic of random material. Annealing the ground surface allows the random material to recrystallize and recover the structure and orientation of the underlying undisturbed material. The effect of certain treatments which might be used to prepare emitters for thermionic converters was studied.

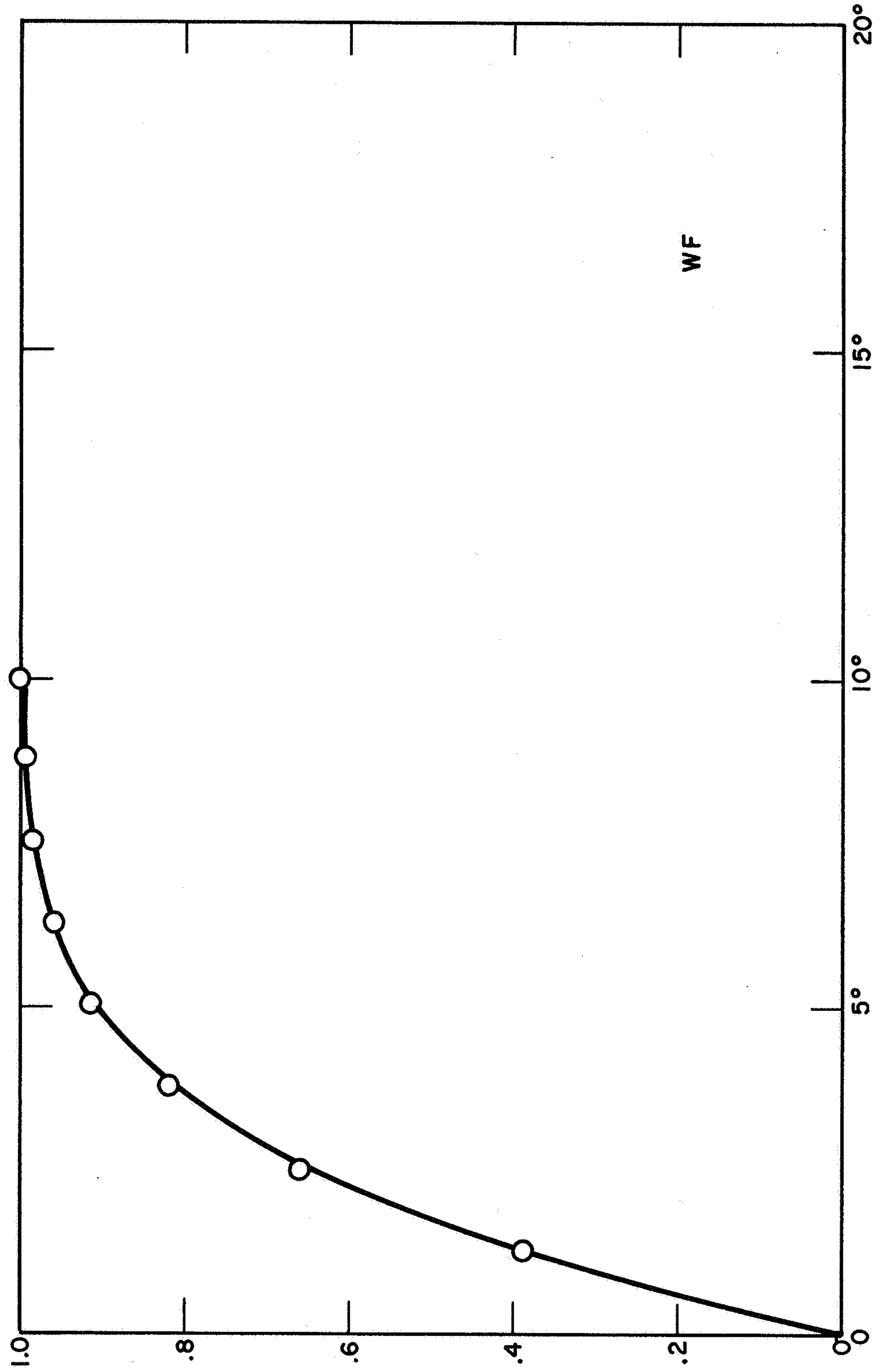

Figure V-27. Pole Figure Curve for Top Surface of As-Received Material. WF.

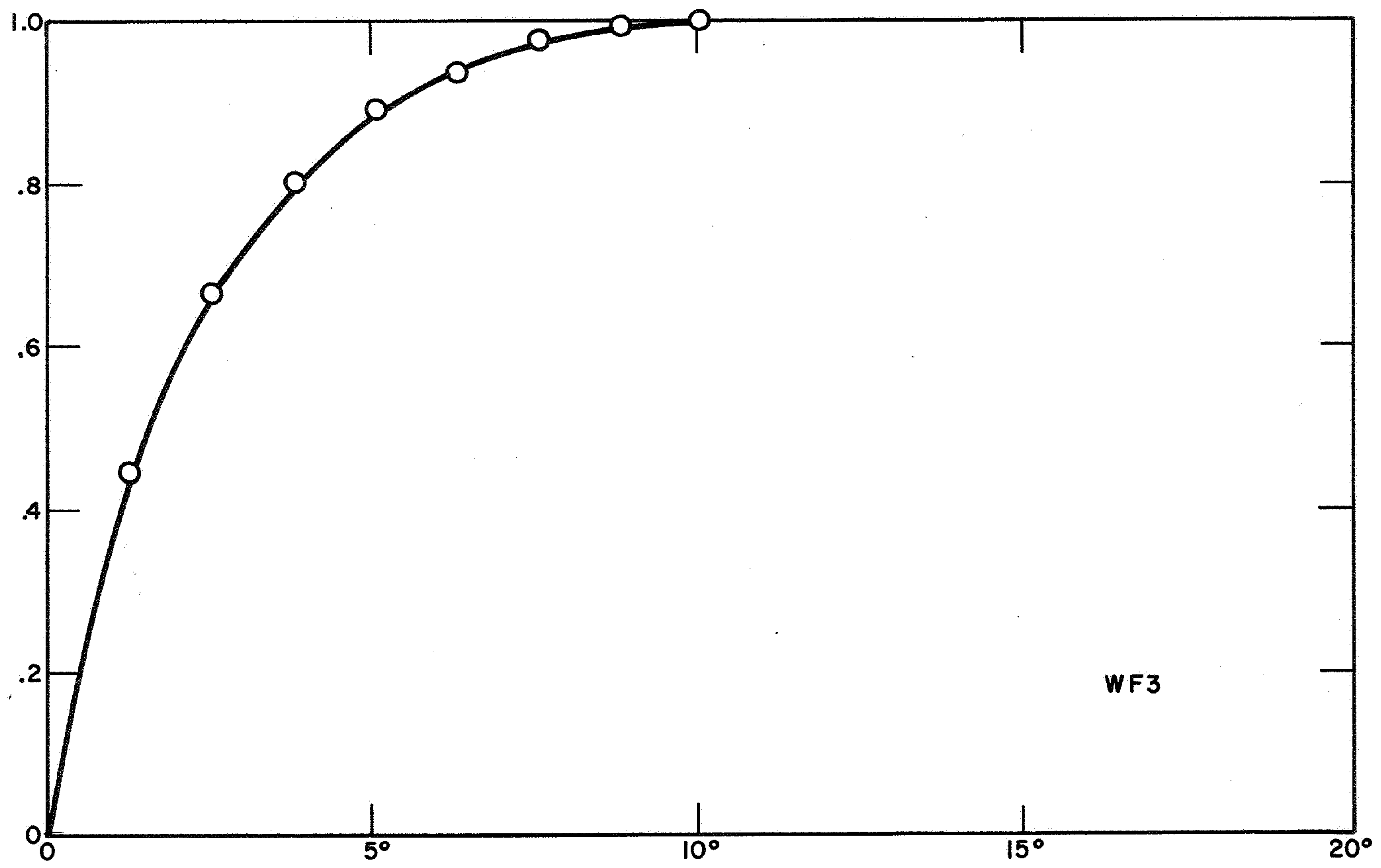

Figure V-28. Pole Figure for Material Ground and Electropolished. WF3′.

Sample WF5 was ground and annealed 20 minutes at 1900°C and then gave the pole figure in Figure V-29. This clearly shows a much milder preferred orientation than the as-deposited material, and approaches the straight line that a random sample would give (from 0 at 0° to 1 at 20°). If such a surface were used as an emitter (at temperatures below 1900°C) it would have a performance characteristic not of fluoride vapor-deposited material but of that heat treatment which had been applied to the material.

If a more drastic heat treatment is applied the ground surface layer can regain the orientation of the underlying deposit. If, however, further treatment causes recrystallization, and grain growth, the coarse new grains will not necessarily share the preferred orientation of their predecessors, and in any case the x-ray technique makes it difficult to sample coarse grains. For if at any time one grain illuminated by x-rays is oriented correctly, it can produce a very strong contribution to the measured diffracted intensity, which produces a large perturbation of the I-versus-α curve and a corresponding perturbation of the derived $\int$ I-versus-α curve. This effect occurs in Figure V-30 and more conspicuously in Figure V-31 around 0.85 on the ordinate.

Figure V-30 indicates that when a ground surface is treated for 1 hour at 2400°C, the resulting surface has some of the preferred orientation of the deposit, at least at large α, but the chance of finding (100) planes within two degrees of the surface is near that for a random sample. More intensive treatment, such as 6.5 hrs at 2600°C (Figure V-31), restores a large part of the preferred orientation, while also producing recrystallization and a large grain size (Figure V-10).

Further work on preferred orientation of deposits is under way.

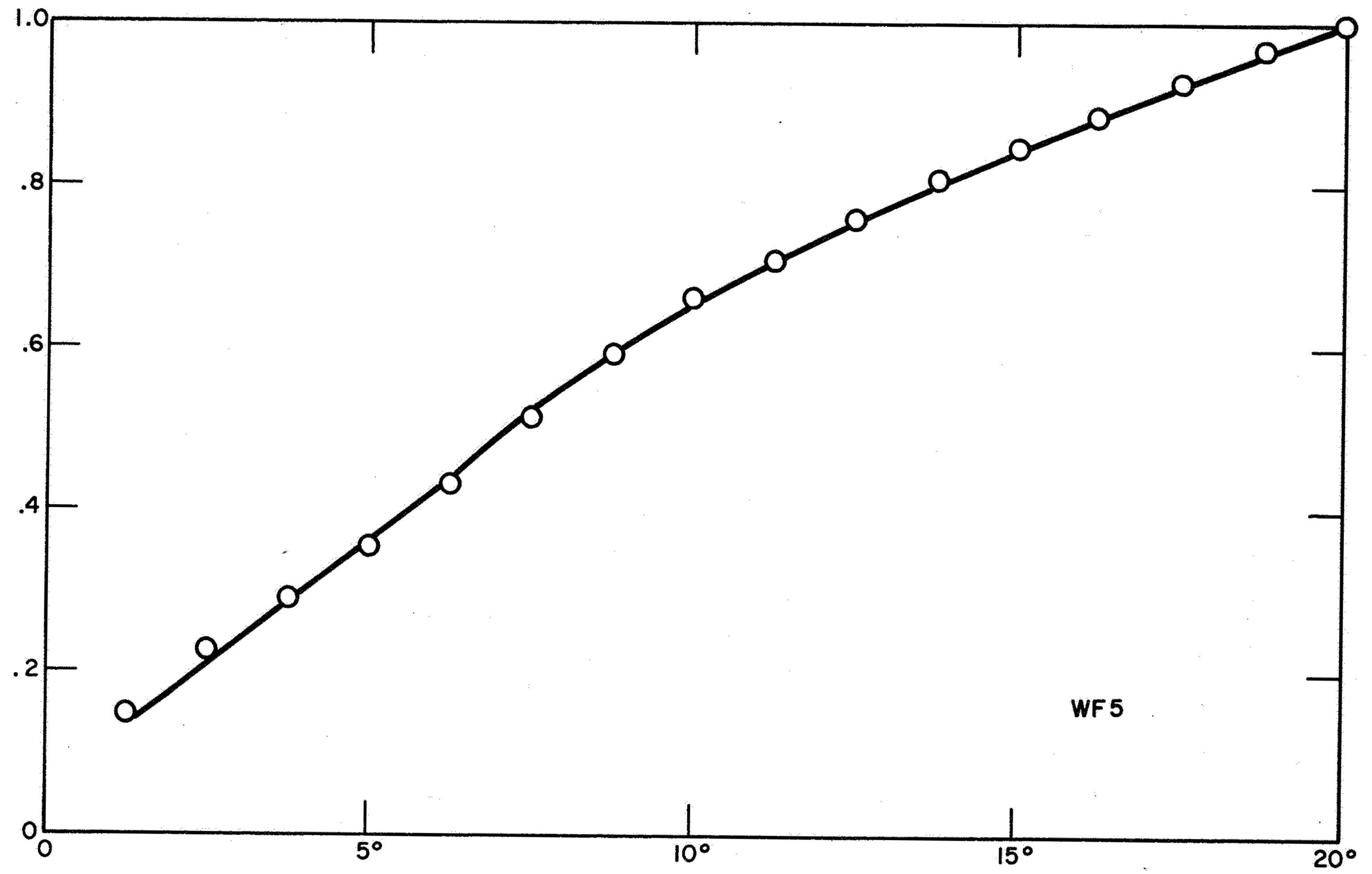

Figure V-29. Pole Figure for Material Ground and Annealed 20 Minutes at 1900°C. WF5.

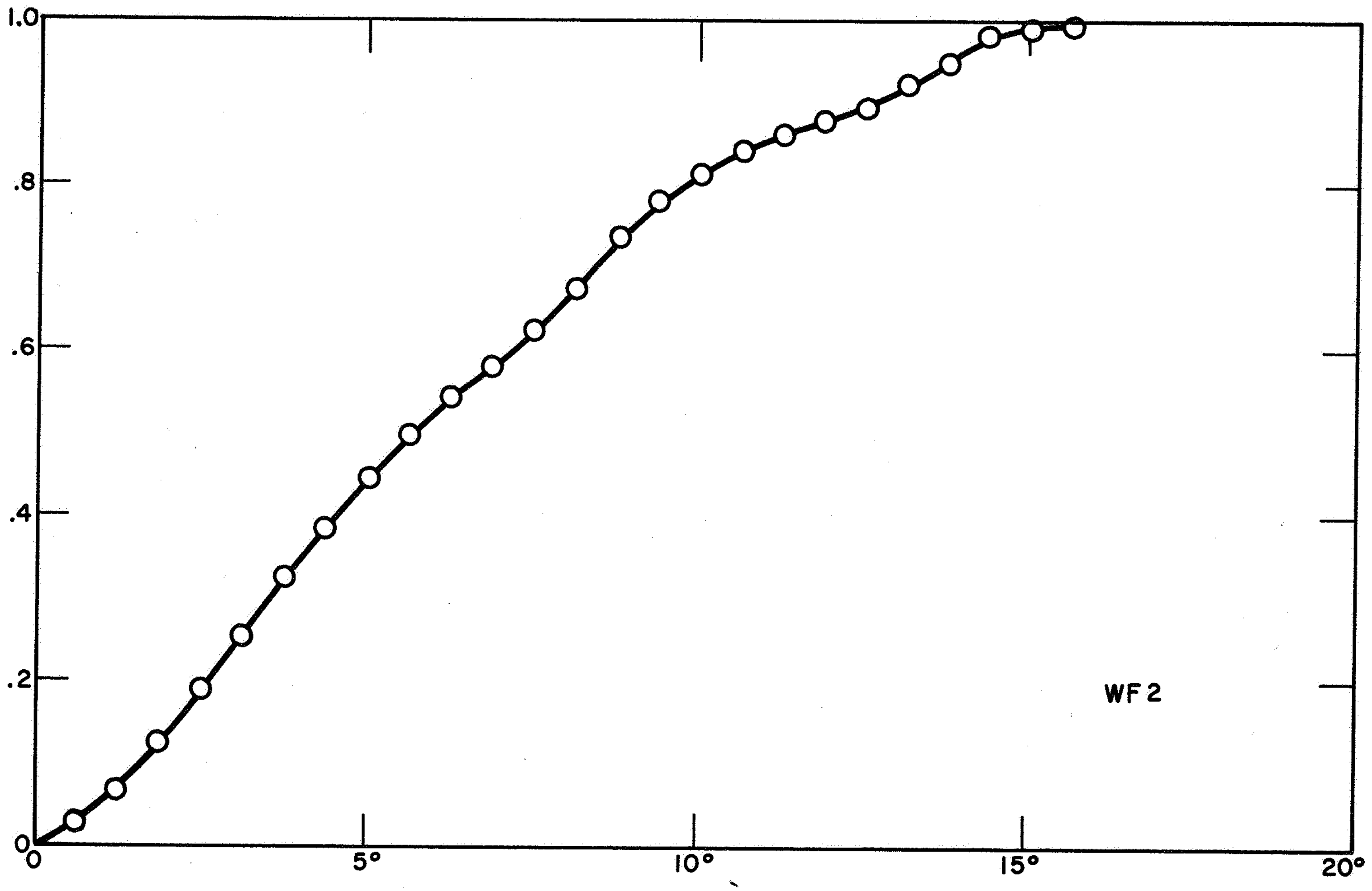

Figure V-30. Pole Figure for Material Heat-Treated for 1 Hour at 2400°C (Compare Figure V-6). WF2.

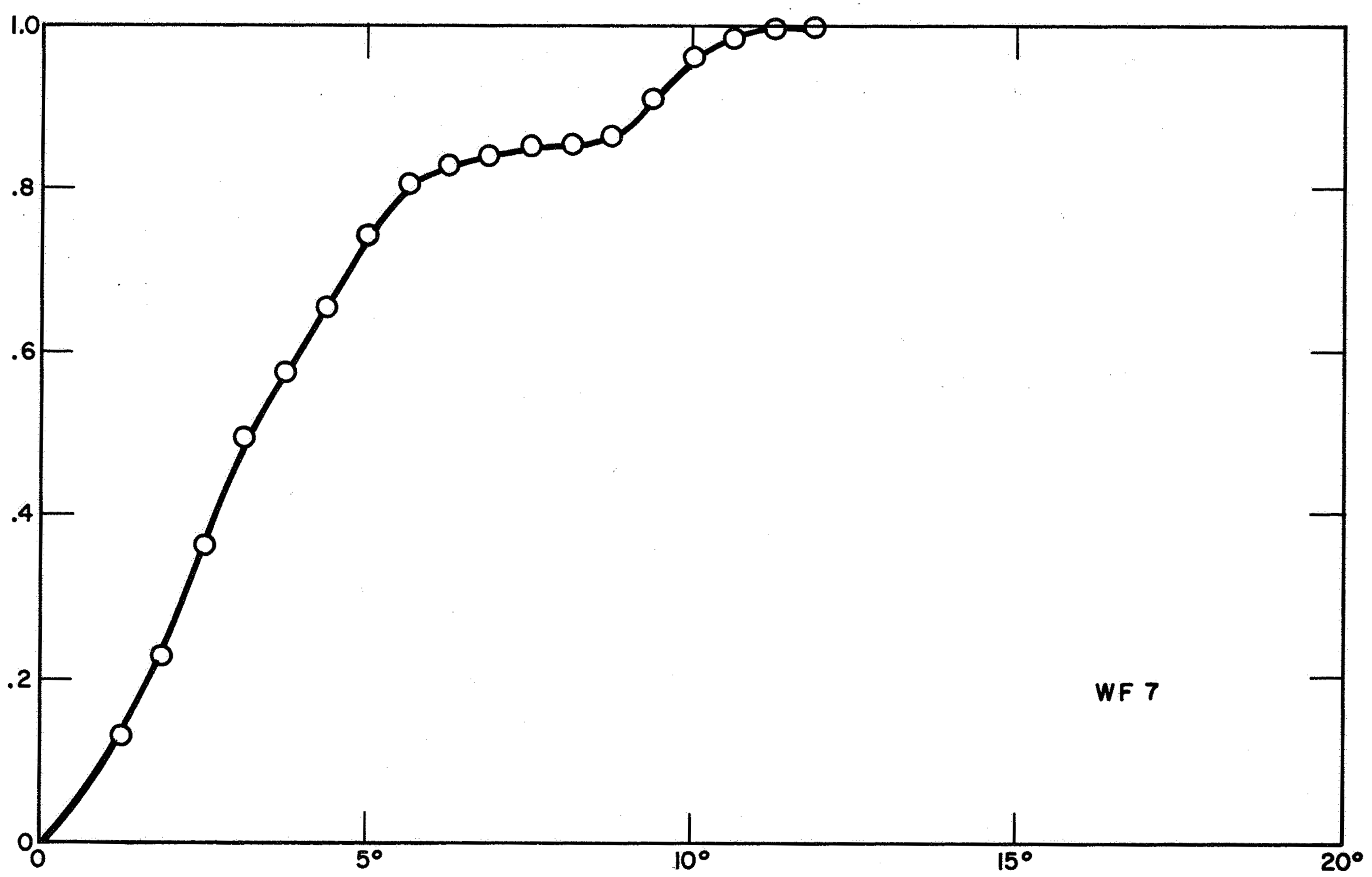

Figure V-31. Pole Figure for Material Heat-Treated for 6.5 Hours at 2600°C (Compare Figure V-10). WF7C.

CHAPTER VI

PLASMA ANALYSIS

D. Lieb

A set of plasma equations was developed and solved numerically in the Final Report on JPL Contract NAS7-508.[1] During this quarter particular attention was devoted to the emitter and collector boundary conditions. A new set of boundary conditions was incorporated in the equations, and the solution was compared with the previous results.[1]

In the set of equations used previously,[1] particle currents entering and leaving the plasma boundaries were expressed in terms of random current.

At the emitter,

$$\overleftarrow{J}_{eo} = J_{ro} \exp(-V_E/\Theta_{eo}) \tag{1}$$

At the collector for accelerating sheath,

$$\overrightarrow{J}_{el} = J_{rl} \tag{2}$$

At the collector for retarding sheath,

$$\overleftarrow{J}_{el} = J_{rl} \exp(V_c/\Theta_{el}) \tag{3}$$

where J_{ro} and J_{rl} are the electron random currents at the emitter and collector sheaths, respectively, $\overleftarrow{J}_{eo}$ and $\overrightarrow{J}_{el}$ are the electron currents from the plasma into the emitter and collector sheaths, V_E and V_C

are the emitter and collector sheath heights, and Θ_{eo} and Θ_{el} are the electron temperatures in the plasma at the sheaths. Similar equations were used for ion currents.

In nuclear reactor theory and some plasma analysis,[2,3] the boundary conditions for the particle current are expressed in terms of directed current. The plasma boundary conditions are then:

$$\overleftarrow{J}_{eo} = J_{ro} \exp\left(-V_E/\Theta_{eo}\right) - J_{eo}/2 \tag{4}$$

$$\overrightarrow{J}_{el} = J_{rl} + J_{el}/2 \tag{5}$$

$$\overrightarrow{J}_{el} = J_{rl} \exp\left(V_c/\Theta_{eo}\right) + J_{el}/2 \tag{6}$$

where J_{eo} and J_{el} are the net electron currents at the sheaths. At the emitter sheath, for the cases examined so far, the random current is typically an order of magnitude higher than the net electron current. The effect of using the directed current will be small. At the collector sheath, however, where random current is almost equal to the net electron current, significant changes can be expected.

As described previously,[1] the plasma equations are solved by selecting a set of six initial values and then advancing step by step across the plasma. From the emitter boundary equations, the initial electron current density, and the reference value of the plasma potential, four of the initial conditions are determined. The remaining two must be chosen arbitrarily and their correctness evaluated from the collector sheath relations when the solution reaches that sheath. The collector sheath equations are:

For electron-accelerating sheath:

$$J_{el} = J_{rl} - J_{sc} \exp (V_c / \Theta_c) \qquad (7)$$

and for electron-retarding sheath:

$$J_{il} = I_{rl} - I_{sc} \exp (V_c / \Theta_c) \qquad (8)$$

where J_{sc} and I_{sc} are electron- and ion-saturated emission currents for the collector. Θ_c is the collector temperature, and I_{rl} and J_{il} are the random and net ion currents at the collector sheath. Substituting the directed current for random current gives:

$$\frac{J_{ei}}{2} = J_{rl} - J_{sc} \exp (-V_c / \Theta_c) \qquad (9)$$

and

$$\frac{J_{il}}{2} = I_{rl} - I_{sc} \exp (V_c / \Theta_c) \qquad (10)$$

Since J_e and J_i are practically constant near the collector and the random currents fall with particle density, solutions with a directed-current boundary condition must occur closer to the emitter. To maintain the same spacing, a larger initial particle density is required. The particle density distributions for the two boundary conditions are compared in Figure VI-1. Other than the slight increase in initial concentration, the results are similar. For most of the cases studied the directed-current boundary condition can be expected to produce only small deviations from random-current boundary solutions.

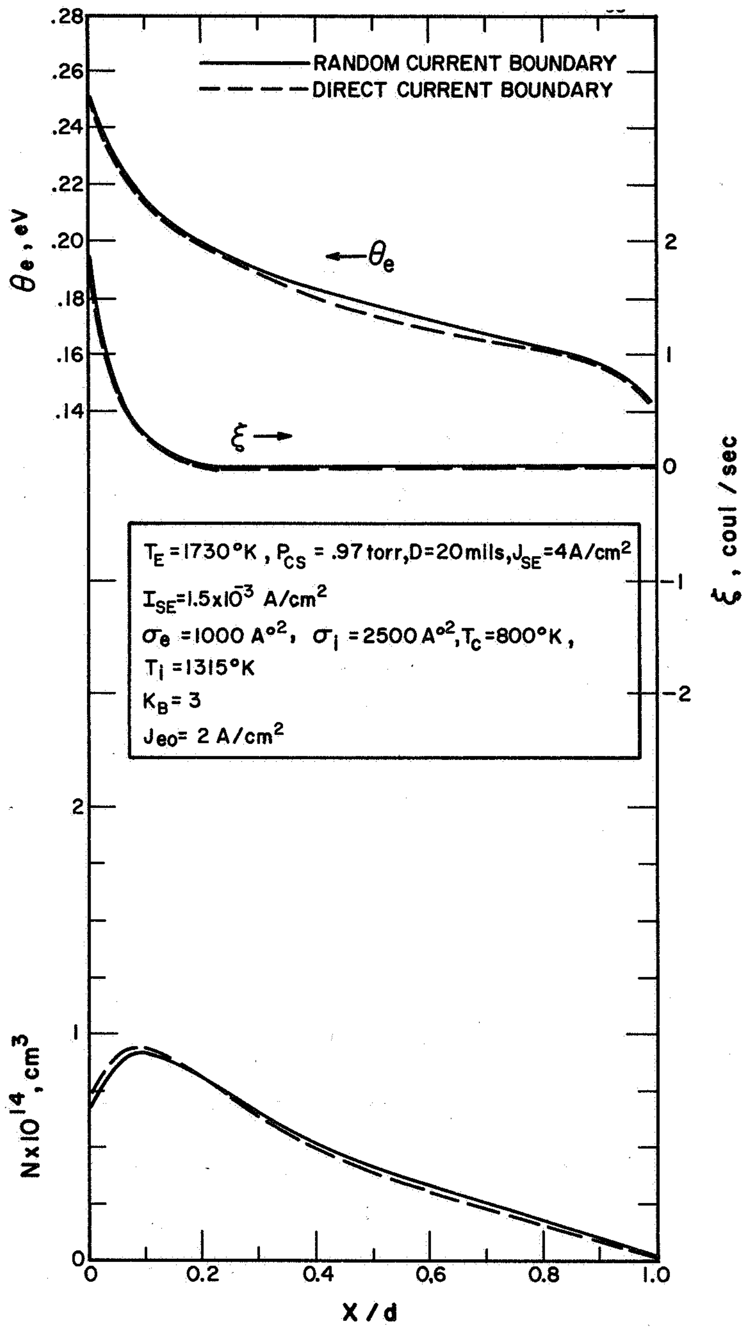
RANDOM CURRENT BOUNDARY
DIRECT CURRENT BOUNDARY
θ_e, eV
.28
.26
.24
.22
.20
.18
.16
.14
$\leftarrow \theta_e$
$\xi \rightarrow$
ξ, coul / sec
2
1
0
-1
-2
$T_E = 1730°K$, $P_{CS} = .97$ torr, D=20 mils, $J_{SE} = 4 A/cm^2$
$I_{SE} = 1.5 \times 10^{-3} A/cm^2$
$\sigma_e = 1000 A^{o2}$, $\sigma_i = 2500 A^{o2}$, $T_C = 800°K$,
$T_i = 1315°K$
$K_B = 3$
$J_{eo} = 2 A/cm^2$
$N \times 10^{14}, cm^3$
2
1
0
0
0.2
0.4
0.6
0.8
1.0
X / d

Figure VI-1 A

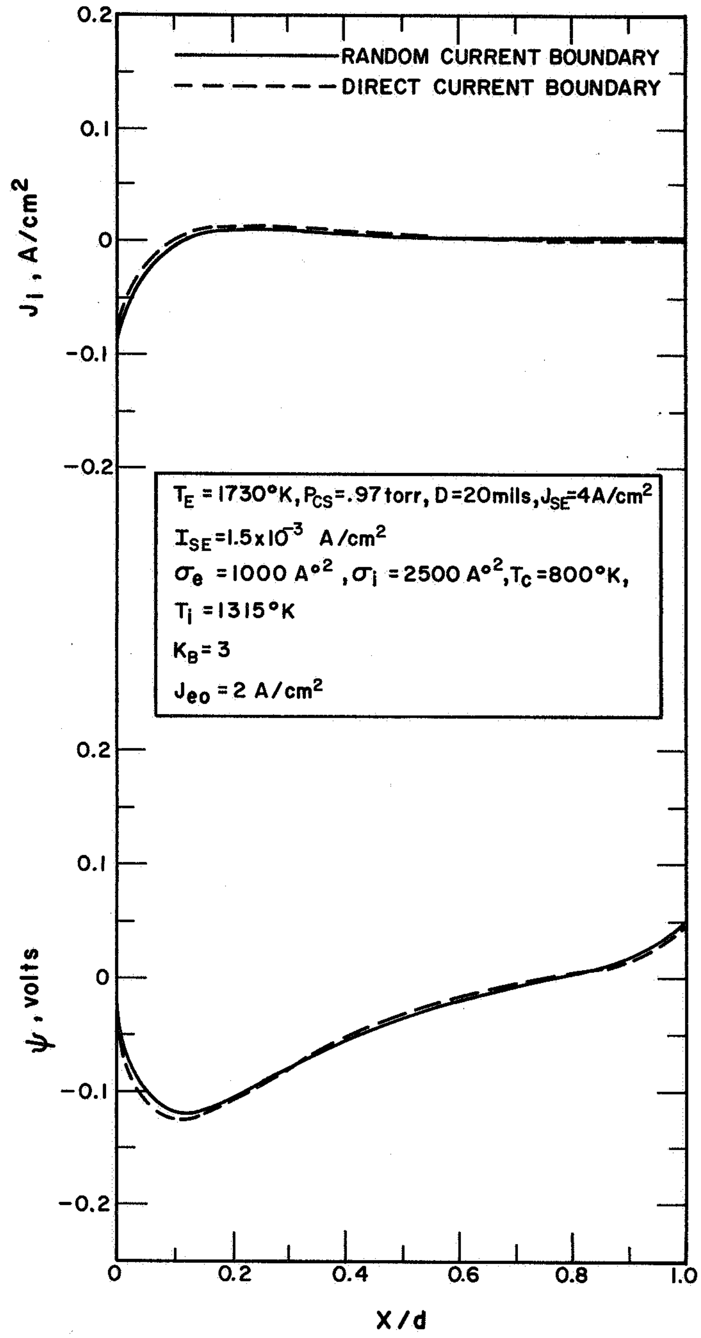
RANDOM CURRENT BOUNDARY
DIRECT CURRENT BOUNDARY
J_i , A/cm^2
0.2
0.1
0
-0.1
-0.2
T_E = 1730°K, P_{CS}=.97 torr, D=20mils, J_{SE}=4A/cm^2
I_{SE}=1.5x10^{-3} A/cm^2
σ_e =1000 A°^{2} , σ_i =2500 A°^{2}, T_C =800°K,
T_i =1315°K
K_B= 3
J_{eo} = 2 A/cm^2
ψ , volts
0.2
0.1
0
-0.1
-0.2
0
0.2
0.4
0.6
0.8
1.0
X / d

Figure VI- 1 B

REFERENCES FOR CHAPTER VI

1. Final Report on Research in Thermionic Conversion, Thermo Electron Report No. TE4072-49-68, prepared for National Aeronautics and Space Administration, Pasadena, under Contract NAS7-508, 1968.

2. Warner, C.; Hansen, L. K., " Transport Effects in the Electron-Rich Unignited Mode of Cesium Diodes." J. Appl. Phys. 38(1967), p. 491.

3. Davidson, B., Neutron Transport Theory. Oxford Univ. Press, New York, 1957.